THE JOURNAL OF PHYSICAL CHEMISTRY B

Article

pubs.acs.org/JPCB

Pump–Probe Microscopy: Spatially Resolved Carrier Dynamics in ZnO Rods and the Influence of Optical Cavity Resonator Modes

Brian P. Mehl, Justin R. Kirschbrown, Michelle M. Gabriel, Ralph L. House, and John M. Papanikolas*

Department of Chemistry, Caudill Laboratories, University of North Carolina at Chapel Hill, Chapel Hill, North Carolina 27599-3290, United States

ABSTRACT: Femtosecond pump–probe microscopy is used to investigate the charge recombination dynamics at different points within a single needle-shaped ZnO rod. Recombination in the tips of the rod occurs through an excitonic or electron–hole plasma state, taking place on a picosecond time scale. Photoexcitation in the larger diameter sections of the interior exhibit dramatically slower recombination that occurs primarily through defects sites, i.e., trap mediated recombination. Transient absorption imaging shows that the spatial variation in the dynamics is also influenced by the cavity resonances supported within the hexagonal cross section of the rod. Finite element simulations suggest that these optical resonator modes produce qualitatively different intensity patterns in the two different locations. Near the end of the rod, the intensity pattern has significant standing-wave character, which leads to the creation of photoexcited carriers in the core of the structure. The larger diameter regions, on the other hand, exhibit intensity distributions in which the whispering gallery (WG) mode character dominates. At these locations, the photoexcited carriers are produced in subsurface depletion zone, where the internal fields separate the electrons and holes and lead to a greater degree of trap recombination on longer time scales.

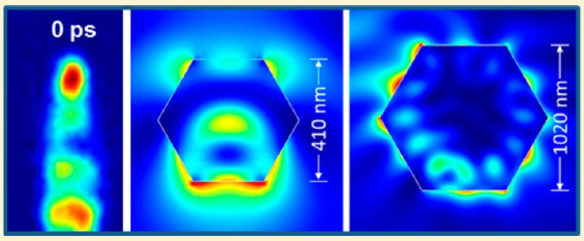

1. INTRODUCTION

The finite sizes of individual particles introduce new dynamical phenomena not found in bulk materials. Quantum confinement of the carrier wave function occurs when the size is smaller than the exciton Bohr radius. It alters the electronic structure, resulting in tunable band gaps, tunable spectral properties, and dynamical phenomena that depend upon the size and shape.[1] Because the exciton Bohr radius is typically only a few nanometers, confinement is important in only the smallest structures, seemingly suggesting that size effects are unimportant beyond the nanoscale. Although different physical mechanisms are at play, larger structures also exhibit size and shape dependent phenomena. Surfaces and intrinsic defects trap mobile carriers resulting in internal electric fields that influence electronic structure and photophysical behavior.[2,3] Band bending that arises from surface charging, for example, extends over tens to hundreds of nanometers and can separate photoexicted electrons and holes. In addition, optical resonator modes appear as the object dimensions approach the wavelength of light, impacting steady-state spectral properties and giving rise to nanostructure lasing.[4−8]

This paper examines the electron–hole recombination dynamics in needle-shaped ZnO rods using femtosecond microscopy. Our results suggest that the resonator modes, in combination with internal fields, give rise to spatially variant carrier dynamics, revealing a connection between the shape and dynamical behavior present in larger mesoscale structures. ZnO is an excellent material for exploring the relationship between the structure and dynamics in this size range. The ability to manipulate the structure of ZnO is enormous, and through a variety of facile synthetic methods many different forms, including nanorods with differing end morphologies, tetrapods, and nanohelices have been produced.[9−11] The needle-shaped rods used in this study are 10–20 μm in length and have faceted hexagonal cross sections with diameters range from 1 to 3 μm at their widest point, down to 300–400 nm at the ends.

A key observation is that the carrier dynamics vary spatially along the structure, with the ends showing dramatically faster electron–hole recombination compared to the interior locations. Comparison of transient absorption and time-resolved emission measurements indicate that recombination at the ends of the structure occurs primarily across the band gap, through an excitonic or electron–hole plasma (EHP) state, whereas trap-mediated recombination dominates at the interior locations. This counterintuitive observation is the result of optical cavity modes supported by the hexagonal cross-section of the rod that result in different spatial distributions of the photoexcited carrier distribution at different points in the structure.

Cavity resonances become important when the size of the structure is comparable to the wavelength of light. The faceted crystalline structures of these ZnO materials give rise to a rich variety of optical cavity modes. Several groups have described longitudinal standing-wave modes propagating along the long axis of the rod.[6−8] In addition to longitudinal modes, cavity resonances supported within the hexagonal cross-section of the

Special Issue: Paul F. Barbara Memorial Issue

Received: July 17, 2012
Revised: October 18, 2012

   dx.doi.org/10.1021/jp307089h | J. Phys. Chem. B XXXX, XXX, XXX–XXX

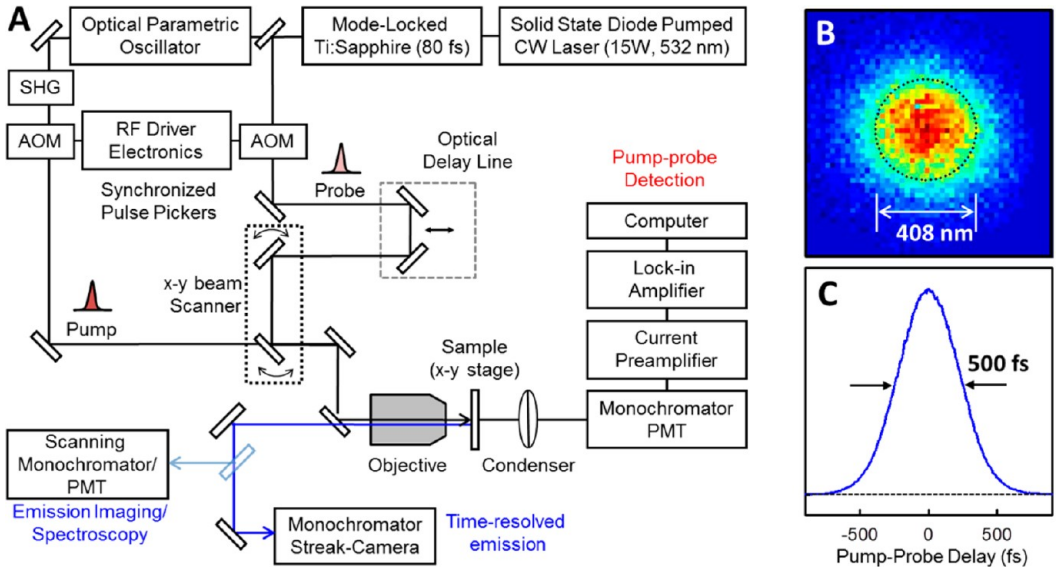

Figure 1. (A) Schematic diagram of a two-photon pump−probe microscope. The frequency-doubled output of an optical parametric oscillator (OPO) at 730 nm is directed on the back aperture of the microscope objective and focused to a diffraction-limited spot at the sample. Imaging is achieved by raster scanning the sample stage across the focused laser spot and monitoring the emission collected by the objective with a scanning monochromator/PMT. Pump−probe microscopy incorporates a second laser beam focused onto the location of the excitation beam. The beam that emerges from the sample is collected by a condenser lens, and its intensity is monitored by lock-in detection. Two acousto-optic modulators (AOM) are used to reduce the repetition rate of the laser to 1.6 MHz. Time-resolved emission measurements are performed by monitoring the emission intensity using a streak camera. (B) Two-photon emission image of a 100 nm nanoparticle with 810 nm excitation. The size of the emission feature suggests that the lateral resolution is approximately 410 nm. (C) Cross-correlation of the pump and probe pulses in the microscope obtained by monitoring the sum-frequency signal generated by the ZnO rod.

rod are also present. Previous reports describe these modes using two classic resonator pictures: Fabry−Pérot (FP) modes supported between two opposing parallel facets, and whispering gallery (WG) modes that correspond to the circulation of light around the periphery of rod via total internal reflection at each crystal face.[12−19] For the experiments described here, where the excitation pulse propagates perpendicular to the rod axis, the transverse modes dominate the resonance effects.

The resonance conditions for both the FP and WG modes depend upon the diameter of the structure, and because of the tapered shape, a fixed excitation wavelength will go in and out of resonance as one moves along the long axis of the rod. We observed both types of resonances in second-harmonic and two-photon emission images,[19−23] which appear as periodic intensity modulation along the long axis of the rod. Although the classic FP and WG resonator models[12−19] reproduce, at least qualitatively, the image features, finite-difference frequency-domain (FDFD) calculations indicate these models are too simplistic. In this size regime (200−1000 nm diameter), the hexagonal resonator modes actually contain characteristics of both the FP and WG resonances, whose relative contributions vary with resonator size. At smaller sizes, the modes have primarily standing-wave character with much of the optical intensity located in the core of the structure. As the size is increased, the intensity distribution shifts to the periphery of the structure, becoming more WG-like in character.

We attribute the spatial variation in the recombination pathways (band-edge vs trap) to differences in these optical intensity distributions. The standing-wave modes existing at the ends of the rods create photoexcited carriers in the core of the structure, where they recombine through bulk-like mechanisms (e.g., exciton or electron−hole plasma recombination). In the larger cross sections, on the other hand, the WG mode distributions produce carriers in the space-charge region, and the internal fields arising from the surface charge result in rapid charge separation and predominately trap-mediated recombination. These results point toward a connection between the shape of the object, and via its optical resonator modes, the charge carrier dynamics that follow photoexcitation.

2. EXPERIMENTAL SECTION

2.1. Materials. The ZnO rods were grown using hydrothermal methods adapted from previously published work.[24,25] A 0.05 M reaction solution of $Zn(NO_3)_2$ and hexamethylenetetramine ($(CH_2)_6N_4$) is heated in a closed bomb, to yield needle-shaped rods ranging from 5 to 30 μm in length and from 0.3 to 2 μm in diameter. Size control is achieved by varying the reaction temperature, time, and/or concentration. After completion, the structures are harvested and sonicated in ethanol to break up aggregates and form a suspension. Microscopy samples are prepared by drop-casting ~250 μL of the suspension onto a microscope slide with an etched reference grid. The grid facilitates the relocating of the rod for subsequent experiments in the optical microscope or structural characterization via SEM imaging. The ability to perform both optical and electron microscopy on the same structure allows us to correlate the photophysical observations with detailed structural information.

2.2. Imaging. The microscope combines an ultrafast laser source with a home-built far-field optical microscope for performing both two-photon emission imaging and time-resolved microscopy, in both pump−probe and emission configurations (Figure 1A). The femtosecond laser source consists of a mode-locked Ti:sapphire laser (810 nm, 80 fs, 80 MHz), whose output is split into two beams by an uncoated glass window. The more intense portion (96%) synchronously pumps a broad-band optical parametric oscillator (OPO),

dx.doi.org/10.1021/jp307089h | J. Phys. Chem. B XXXX, XXX, XXX−XXX

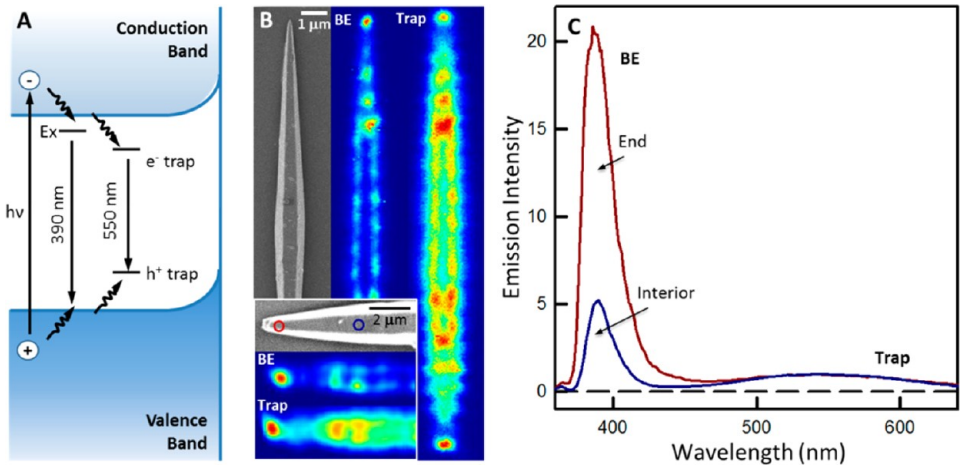

Figure 2. (A) Illustration of ZnO band structure depicting photoexcitation, band-edge emission at 390 nm from an exciton state (EX), and trap-mediated emission at 550 nm. (B) SEM and two-photon emission images (band-edge and trap) for two different structures. (C) Emission spectra observed at a point near the end and at a point within the interior of the rod are shown at the lower-left of panel B. Circles on the SEM image indicate locations of spectroscopic measurements.

whose frequency-doubled output at 730 nm (1 nJ/pulse) is used to excite the ZnO through a two-photon absorption process.

Conventional two-photon emission microscopy is achieved by directing the 730 nm beam onto the back aperture of a microscope objective (0.8 NA, 50×), which focuses it to a diffraction limited spot, resulting in two-photon excitation at a localized region of the ZnO rod. Light emanating from the structure is collected by the objective, passed through a dichroic beam splitter, and focused onto the slit of a monochromator and photomultiplier tube (PMT). Emission images are collected by raster scanning the sample across the focal point of the objective with a piezoelectric nanopositioning stage while monitoring the intensity of the emitted light. Imaging is performed without a cover slip under ambient conditions.

The spatial resolution of the microscope is determined by the size of the laser spot at the focus of the objective. Because two-photon absorption scales with the square of the optical intensity, efficient excitation occurs only at the focus, resulting in confocal-like behavior and a lateral excitation dimension that is smaller than the diffraction limit.[26] Emission images of a 100 nm particle (Figure 1B) indicate that the spatial extent of excitation is 380 nm for the 730 nm excitation, and 410 nm for 810 nm excitation. Both are slightly larger than the theoretical limits of 350 and 380 nm for the two different wavelengths, respectively.[26]

2.3. Spatially-Resolved Spectroscopies. Spectroscopic observations are made at specific points within the structure by using the scanning stage to position the excitation beam. Emission spectra can be collected using a scanning monochromator. Time resolved photoluminescence measurements are performed with monochromator/streak camera. The streak camera separates the emitted photons in both wavelength and time and is capable of following the evolution of the emission spectrum with ≈15 ps time resolution.

2.4. Pump−Probe Microscopy. Transient absorption microscopy is achieved by combining the 730 nm excitation beam (pump pulse) with the weak reflection of the 810 nm mode-locked oscillator beam and then directing the copropagating pulse pair onto the back aperture of the microscope objective. Two synchronized acousto-optic modulator (AOM) pulse pickers reduce the repetition rates of the pump and probe beams to 1.6 MHz, thus ensuring nearly complete relaxation before the next pump−probe pulse pair arrives.[20] A motorized linear stage controls the time delay between pump and probe pulses. Both the pump and probe pulses are focused to diffraction limited spots that are spatially overlapped within a single structure. The pump and probe polarizations were parallel to each other and oriented perpendicular to the long axis of the rod. The probe beam is collected by a condenser lens, focused onto the entrance slit of a monochromator, and detected by a photomultiplier tube and current preamplifier. The excitation beam is modulated at 4 kHz, and pump induced changes in the intensity of the probe pulse are monitored by a digital lock-in amplifier. The time resolution of the pump−probe measurement was characterized by cross-correlation of the two laser pulses using the frequency mixing properties of the ZnO (Figure 1C), which indicates a time-resolution of ∼500 fs.

3. RESULTS AND DISCUSSION

Zinc oxide is a wide band gap semiconductor with a large exciton binding energy (60 meV). Photoexcitation by a single UV photon, or simultaneous two-photon excitation in the near-infrared, promotes electrons from the valence band to the conduction band. These free charge carriers (Figure 2A) can then either associate into excitons that lie just below the conduction band edge, resulting in a UV-blue emission at 390 nm or become trapped at defect sites in the crystal lattice, giving rise to a broad visible emission band centered at 550 nm.[9]

We have used a combination of two-photon emission and time-resolved microscopies to investigate the charge carrier dynamics at specific points within mesoscale ZnO structures. Two-photon emission images (section 3.1) reveal the presence of optical resonator modes. Transient absorption and time-resolved emission measurements (section 3.2) performed at different points within the same structure show that the charge carrier recombination is significantly faster at the ends of the structure, with the slower recombination in the interior regions being dominated by trap mediated pathways. Spatially separated pump−probe experiments (section 3.3) indicate that carrier diffusion out of the excitation volume is

dx.doi.org/10.1021/jp307089h | J. Phys. Chem. B XXXX, XXX, XXX−XXX

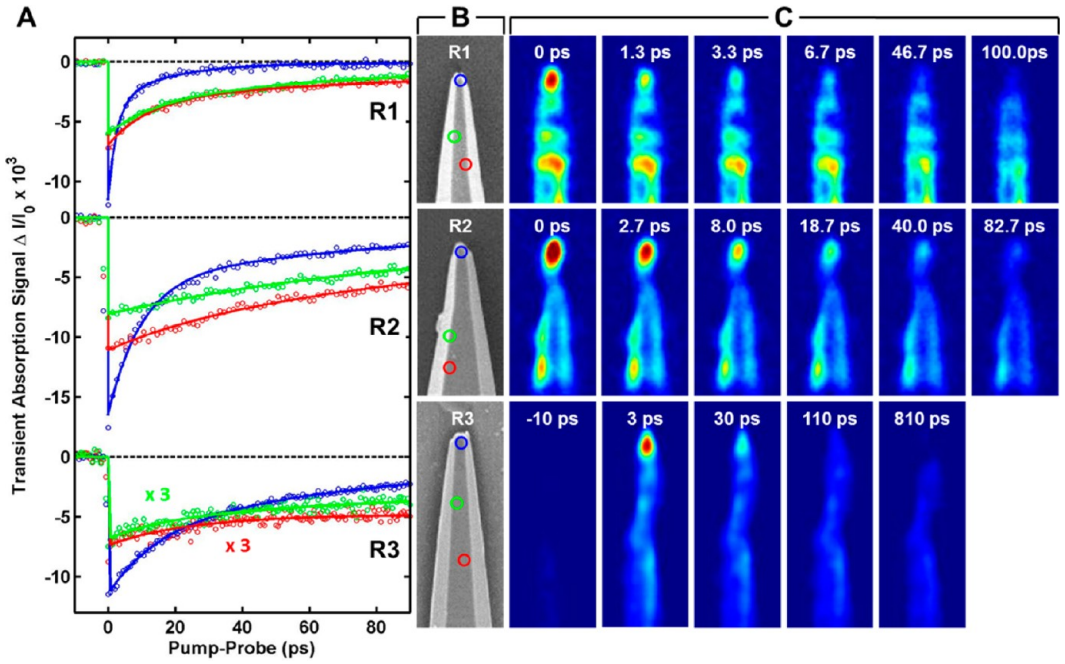

Figure 3. Pump−probe transients ($\Delta I/I$) collected from the end (blue) and two different points within the interior (green and red) from three different rods, R1, R2, and R3. The locations of the collected points for the three transients are indicated in the corresponding SEM images (B), where the horizontal dimension of each image is 3 μm. (C) Series of transient absorption images (ΔI) obtained at different pump−probe delays for the three rods. The series of pump−probe images show the rapid loss of the signal at the rod end, which ultimately decays to zero signal, whereas the response from the interior persists significantly longer.

insignificant, ruling out physical confinement and other mechanisms that require expansion of the charge cloud to explain the observed spatial variation. Finite-element simulations (section 3.4) suggest a connection between the spatially dependent dynamics and cavity resonator modes. They indicate that the WG modes, which are prevalent in the larger cross sections, produce carriers predominately in the surface depletion zone, where internal fields separate the electrons and holes, leading to greater trapping events and slower recombination.

3.1. Emission Imaging and Photoluminescence Spectroscopy. Scanning electron microscopy (SEM) and two-photon emission images acquired while monitoring the band-edge or the trap emission channels for two different rods are shown in Figures 2B. A prominent feature in many of the emission images is the variation in the emission intensity across the interior of the structure. Though the contrast varies from rod-to-rod, some structures exhibit a pronounced pattern of emission "spots" that are evenly spaced along the long axis of the rod. This intensity variation is a consequence of FP and WG modes supported within hexagonal cross section (Figure 2B). The tapered shape causes the fixed excitation wavelength to go in and out of resonance due to the changing diameter along the length of the rod, giving rise to the periodic emission pattern. Light couples more efficiently into the structure at the resonance locations, resulting in a greater number of photo-excited carriers, and hence a greater emission intensity.[12,22,27]

Photoluminescence spectra (Figure 2C) obtained from the rod shown in the lower portion of Figure 2B show both the narrow exciton and broad trap emission bands that are characteristic of ZnO photoluminescence. The figure shows spectra collected following excitation at two different locations, indicated by the blue and red circles on the SEM image (Figure 2B, lower left). The relative intensities of the two emission bands vary across the structure, with the end showing a more intense band-edge emission that suggests a greater propensity for *e-h* recombination across the band gap at that location.

3.2. Ultrafast Microscopy. Transient absorption microscopy with spatially overlapped pump and probe pulses were performed on three different rods denoted R1, R2, and R3 (Figure 3). The transient response (Figure 3A) was monitored at three different points in each rod, the end (blue) and two interior locations (green and red). The exact positions are indicated by colored circles on the corresponding SEM images (Figure 3B). The transients exhibit complex decay kinetics with fast (<30 ps), intermediate (100−200 ps), and long (>500 ps) components, whose relative amplitudes depend upon position. Interior locations exhibit all three components, with the fastest contributing only 25−50% of the total amplitude. On the other hand, the ends are dominated by the fastest component, which accounts for 60−100% of the amplitude.

Two different processes contribute to the magnitude of the pump−probe signals. The first is induced absorption, which arises from near-infrared excitation of free-carriers. In addition, there is a Kerr lens contribution, resulting from a spatial variation in the index of refraction associated with the localized photoexcited carrier distribution (vide infra). Although the absorptive component is negative, corresponding to a *decrease* in the probe beam intensity, the lensing contribution can result in either an increase or decrease in the probe intensity, and give rise to either a positive or a negative signal. Because the magnitudes of both the absorptive and lensing contributions depend upon the concentration of carriers, we attribute the decay of the pump−probe signal to the decrease in the free carrier population due to recombination and trapping events.

Pump−Probe Imaging. The carrier dynamics at the end of the rod differ dramatically from those observed at the interior, with the ends showing typically faster recombination rates than

dx.doi.org/10.1021/jp307089h | J. Phys. Chem. B XXXX, XXX, XXX−XXX

any other point in the structure. Spatial variation is particularly apparent in images obtained by fixing the pump−probe delay and monitoring ΔI as a function of position (Figure 3C). At early delays, the largest signal is at the end of the rod. Although the overall signal in the interior regions is less intense compared to the end, there are localized, periodic regions of greater signal observed throughout the interior. This spatial modulation in the pump−probe signal is attributed to cavity modes (FP and WG modes) supported within the cross section of the structure.[19,21,22] At longer delays, the bright spot at the end diminishes, becoming less intense than the interior and eventually disappearing altogether. Although differences from structure to structure are common in nanoscale materials, spatial variation in the dynamical response of individual objects has not been reported.

Combined Pump−Probe and Ultrafast Emission. Transient photoluminescence provides a direct view of the band-edge and trap mediated e−h recombination processes. A spectral-temporal intensity map (Figure 4A) of the time-resolved

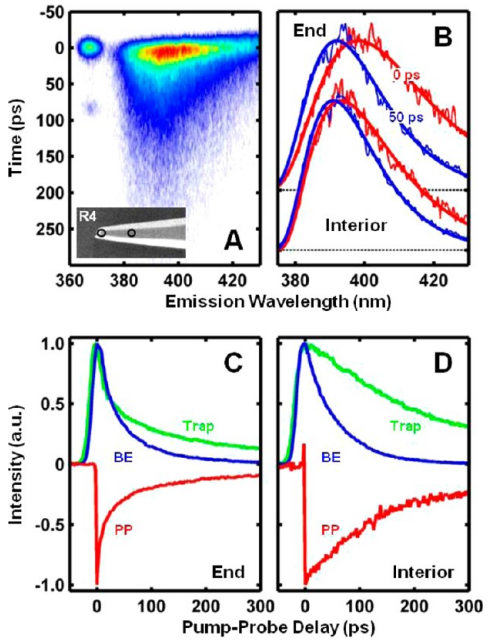

Figure 4. (A) Spectral-temporal intensity map of the emission collected from the end of the rod (R4) and detected using a streak camera. The main feature is the band-edge emission; the narrow peak at 365 nm is the second-harmonic of the excitation pulse and provides the instrument response (17 ps). The inset shows the SEM image and locations of spectroscopic measurements (end versus interior). The vertical dimension of the SEM image is 3 μm. (B) Time-resolved spectra obtained at 0 (red) and 50 ps (blue) from the end of the rod (upper set) and interior (lower set). (C, D) Comparison of the band-edge (BE), trap emission, and pump−probe (PP) data collected at the two points.

emission data collected from the end of a third rod, R3, shows a rich evolution of the band-edge emission, which shifts to the blue as it decays during the first 15−20 ps. Horizontal slices through the map correspond to snapshots of the emission spectrum at different times. The emission band initially appears with $\lambda_{max}\approx$400 nm, and then narrows as it blue shifts to a limiting position of 390 nm.

Spectral shifts of this type are one signature of the electron−hole plasma (EHP) emission that occurs at high carrier densities in II−VI semiconductors.[28−30] When the carrier density exceeds the Mott threshold, Coulombic and exchange interactions weaken the exciton binding and reduce the band gap (i.e., band gap renormalization). This phenomenon gives rise to a collective EHP state with an intense, red-shifted emission relative to the exciton, as well as an enhanced recombination rate due to a greater degree of overlap between electron and hole wave functions. As electrons and holes recombine, the charge carrier density decreases, resulting in the time-dependent blue shift that reflects transition back to the excitonic state. Our time-resolved emission data indicate that the EHP to exciton transition in these structures occurs during the first 15−20 ps, consistent with observations in bulk and nanostructured ZnO.[28,31] Photoexcitation of the interior shows a significantly smaller spectral shift (Figure 4B) and decreased propensity for EHP formation compared to the end. We estimate, on the basis of the two-photon cross-section,[32] that $\sim 10^{20}$ carriers/cm^3 are produced by the pump pulse. This is well above the EHP threshold reported for ZnO,[33] consistent with our observations.

A comparison of the pump−probe and photoluminescence decays (Figure 4C,D) shows qualitatively different behavior at the end of the rod compared to the interior. At the end of the rod, the decays of the pump−probe, band edge, and trap emission are similar to each other (Figure 4C), indicating that a major fraction of the electron−hole recombination events occur through the EHP state. At the interior location (Figure 4D), the pump−probe signal decays slowly, on the same time scale as the trap emission, suggestive of a carrier population that recombines primarily through defect states. These observations suggest that the overlap of the electron and hole wave functions persists in the tips of the rods, whereas at interior sites the two become spatially separated, suppressing band-edge recombination and resulting in a greater degree of trap mediated recombination. Given that the tips of the rods should possess the greatest concentration of defects, the conclusion that trap-mediated recombination is less important there is counter-intuitive.

The spatial variation in the dynamics could stem from several factors. A greater degree of physical confinement in the tips of the rod is one possible explanation. With no room for the charge cloud to expand in the narrow tips, the high carrier density formed upon photoexcitation persists, leading to a prolonged overlap of the electron and hole wave functions, and a propensity for EHP formation. In the interior of the structure, on the other hand, carriers can migrate away from the excitation region through simple diffusion, or perhaps driven by internal fields that separate the electrons and holes, resulting in a decrease in the charge density that makes it more difficult to form and sustain the EHP. Spatially separated pump−probe experiments (described below) probe the expansion of the charge cloud and test this hypothesis. A second possibility is that the spatial variation arises from a difference in *where* carriers are created (i.e., the core versus surface region). FDFD calculations are used to gain insight into distribution of the optical field within the structures. Overall, our analysis suggests that the spatial variation in the carrier dynamics arises not from carrier diffusion, but rather from different spatial distributions in where the charge carriers are created.

3.3. Spatially-Separated Pump−Probe Microscopy. The spatially separated pump−probe configuration excites structures in one location and probes them in another by incorporating two separate positioning mechanisms for the

dx.doi.org/10.1021/jp307089h | J. Phys. Chem. B XXXX, XXX, XXX−XXX

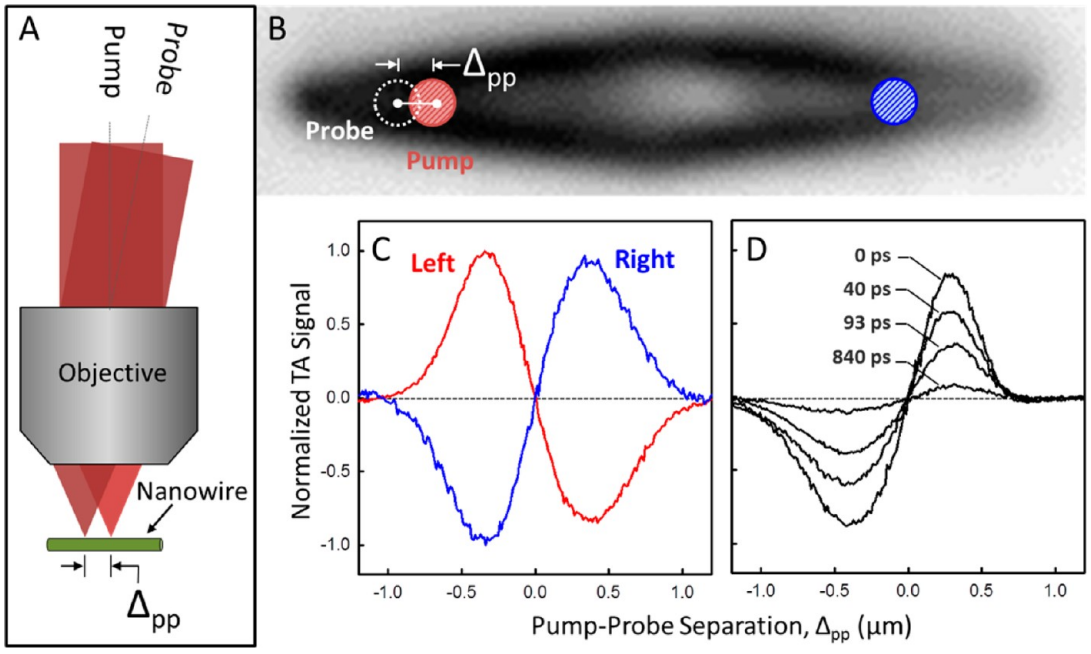

Figure 5. (A) Illustration of spatially separated pump−probe configuration via angle scanning of the probe beam. (B) Bright-field image of the ZnO rod showing locations of pump−probe separation scans. (C) Pump−probe signal as a function of the separation of the pump and probe spots at an early delay time. The red and blue scans correspond to data collected from the left and right locations, respectively. (D) Pump−probe separation scans obtained at a series of delays. Note: data in panels C and D were obtained from different rods.

pump and probe beams. One laser spot is positioned over a particular point in the structure via adjustment of the x−y sample stage. The position of the other beam is controlled by directing it through an x−y scanner that alters the angle it makes relative to the fixed beam as it enters the objective, causing it to be focused at point that is laterally separated from fixed beam by an amount Δ_{pp} (Figure 5A).

Contributions to Pump−Probe Signal. Figure 5 shows the transient absorption signal collected as a function of the separation between the pump and probe spots following excitation at two different locations within a single rod. These data were obtained with the probe beam fixed (scanned pump beam); however, similar observations are made with the pump beam fixed and probe beam scanned. Excitation toward either end of the rod results in derivative-like signals, with positive signals observed when the probe beam is placed between the pump spot and the rod tip. Because ZnO does not absorb in the near-infrared, the positive going signals cannot be the result of photobleaching. The derivative like signal results from interaction of the probe beam with the localized carrier distribution, resulting in a spatial variation in the index of refraction (i.e., a lens) that alters the direction of the probe beam as it passes through the rod. When the focused probe spot is positioned between the pump and the tip, it is deflected toward the middle of the rod. As the probe pulse exits the needle-shaped structure, it experiences a larger facet and greater clear aperture, and as a result, its intensity *increases*. When the probe is positioned on the other side of the pump spot, it is deflected toward the tip, experiences a smaller clear aperture and its intensity is reduced. Scans obtained at intermediate locations show that the negative lobe increases in magnitude as the pair is moved toward the center, becoming entirely negative at the midpoint (Figure 6). These results suggest that the pump−probe signals include contributions from both an induced absorption, arising from near-infrared excitation of

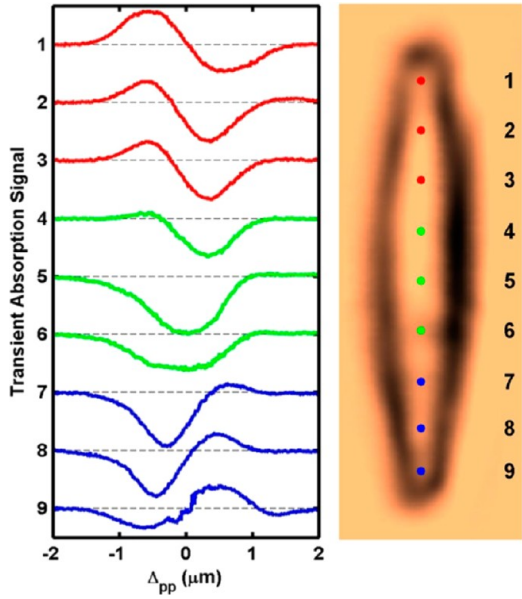

Figure 6. (Left) Transient absorption signal vs pump−probe separation (Δ_{pp}) at 1 ps pump−probe delay for nine different locations. (Right) Transmission image at 810 nm with nine different locations depicting positions of the Δ_{pp} scans along the c-axis.

free-carriers,[34] and a lensing component originating from a spatial variation in the index of refraction due to the localized excitation.[32,35−37]

The transient lens created by photoexcitation could result from either a photoinduced electronic response (i.e., a Kerr lens) or local heating of the structure (i.e., a thermal lens). The relative magnitude of these two contributions can be estimated from the optical properties of ZnO. The Kerr lens results from intensity dependent, nonlinear polarization of the lattice due to optical excitation, and it includes both a nonresonant

dx.doi.org/10.1021/jp307089h | J. Phys. Chem. B XXXX, XXX, XXX−XXX

contribution from the bound electrons and a resonant contribution from photoexcited charge carriers. The change in index of refraction of the ZnO due to the electronic excitation is given by[32,38]

$$\Delta n^{\mathrm{El}} = \gamma\Phi + \sigma_{\mathrm{r}} N_{2h\nu} \tag{1}$$

where the first term corresponds to the instantaneous response of the bound electrons, whereas the second term arises from charge carriers produced through two-photon excitation. In this expression γ (2.51×10^{-11} cm^2/W at 730 nm) is the bound-electron nonlinear refractive index, and σ_{r} (3.02×10^{-20} cm^3 at 730 nm) is the change in the index of refraction due to photoexcited charge-carriers, both of which have been measured using traditional Z-scan methods.[32] $N_{2h\nu}$ is the photoexcited charge carrier density produced by two-photon excitation, which we estimate, on the basis of the two-photon cross section,[32] to be 10^{19}–10^{21} carriers/cm^3 under our experimental conditions. Pump–probe separation scans collected at a series of delays (Figure 5D) show that the lens persists at longer times indicating that the instantaneous response ($\gamma\Phi$) is a minor component of the overall signal, i.e., $\Delta n^{\mathrm{El}} \approx \sigma_{\mathrm{r}} N_{2h\nu}$. The thermal lens arises from local heating, which also alters the refractive index, i.e.

$$\Delta n^{\mathrm{T}} = \frac{2E_{h\nu}}{\rho_0 C_P}\left(\frac{\mathrm{d}n}{\mathrm{d}T}\right) N_{2h\nu} \tag{2}$$

where C_p is the heat capacity (40.17 J mol^{-1} K^{-1}), ρ_0 is the density (0.069 mol/cm^3), and $(\mathrm{d}n/\mathrm{d}T)$ is the thermal-optical coefficient (0.7×10^{-4} K^{-1})[32] for ZnO. The relative magnitude of the two effects is then

$$\frac{\Delta n^{\mathrm{El}}}{\Delta n^{\mathrm{T}}} = \frac{\rho_0 C_p \sigma_{\mathrm{r}}}{2E_{h\nu}\left(\frac{\mathrm{d}n}{\mathrm{d}T}\right)} \tag{3}$$

Using known materials properties of ZnO suggests that the change in refractive index due to the electronic response is approximately 2000 times greater than the thermal affect, implying that the transient lens is the result of the photoexcited carrier distribution and not local heating.

This conclusion is further supported by the pump–probe separation profiles collected at a series of delay times. The shape of the profile is independent of delay, and its amplitude decay coincides with decay of the photoluminescence. If the lens were thermal in nature, the decay of the pump–probe separation profile would reflect the return of the lattice to its initial temperature, which would most likely not coincide with charge carrier recombination. This observation implies that the lens owes it origin to the photoexcited carrier distribution.

Carrier Diffusion. The pump–probe separation profile reflects the spatial extent of the carrier distribution, and the observation that it does not change as the carriers recombine suggests that there is not significant expansion of the initial charge cloud produced by localized excitation, at least on a length scale detectable with our spatial resolution. This further implies that physical confinement of the carriers is not the origin of the spatial variation observed in the charge carrier dynamics.

3.4. Role of Cavity Resonator Modes. The spatial variation observed in the pump–probe images is also observed in the band-edge and trap emission images.[19–23] It is attributed to optical cavity modes supported by the rod's hexagonal cross section, which becomes visible when the structure's dimensions are comparable to the wavelength of light. Both the FP and WG resonances have resonance conditions that depend upon the excitation wavelength and the cross-sectional diameter of the rod.[12–19] Due to the needle shaped structure, the diameter changes along the length of the rod, causing the excitation light to go in and out of resonance, giving rise to the observed patterns.[21,22]

We have used FDFD methods to simulate the distribution of the optical intensity within the structure.[19] The simulation model (Figure 7A) consists of a Gaussian EM source that is focused onto a two-dimensional hexagonal slab of ZnO surrounded by air. The Gaussian source is placed at the boundary of the simulation box and is parametrized (i.e., frequency, numerical aperture, spatial extent at the boundary, etc.) to mimic the size and focus of the laser beam in the experimental arrangement and is polarized parallel to the top edge of the box. Figure 7B shows the optical field of the source in the absence of ZnO, with the hexagon depicting the cross-sectional size of the rod near the tip for comparison. The source is directed toward the ZnO from the top, and its center can be laterally offset relative to the center of the hexagonal slab. The

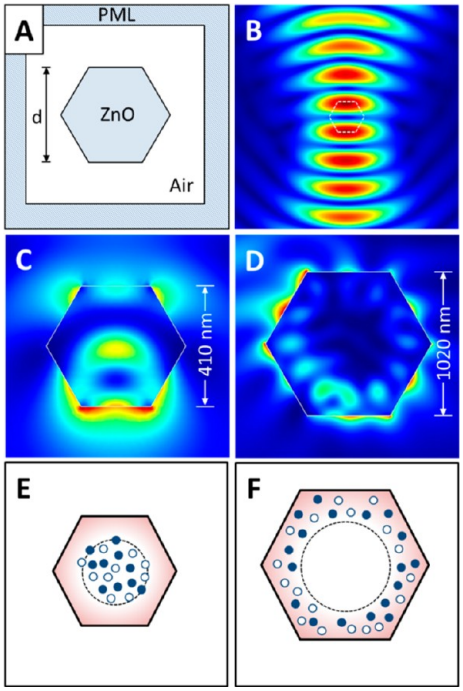

Figure 7. (A) Illustration of FDFD simulation cell. The two-dimensional model includes a hexagonal region representing the ZnO (n = 2.2), surrounded by air (n = 1). The EM source is placed at the top boundary and is parametrized to produce a focused spot at the center of box. The source is $\vec{E}$-field polarized parallel to the top boundary (i.e., perpendicular to the rod axis, which is normal to the page). (B) Magnitude of the optical electric field, $|\vec{E}|$, produced by the EM source in the absence of the ZnO rod. Red is maximum field and blue is zero field. The dashed hexagon in the center shows the size of a d = 410 nm resonator for reference. Distribution of the optical intensity (i.e., $|\vec{E}|^2$) for resonators with (C) d = 410 nm, which is commensurate with the cross sectional diameter near the rod tip, and (D) d = 1020 nm. For the smaller resonator, the EM source is centered over the top facet. For the larger resonator, the source is laterally displaced to the left of the resonator. Illustration of where carriers are created in the smaller (E) and larger (F) resonators.

dx.doi.org/10.1021/jp307089h | J. Phys. Chem. B XXXX, XXX, XXX–XXX

simulations suggest the intensity patterns in the tip differ from those observed in larger interior sections.

The maximum integrated intensity for larger resonator sizes, similar to the interior sections, occurs when the source is offset to one side or the other. These patterns have clear WG mode characteristics, with the largest intensity being located near the surface of the rod. This could be the origin of the increased trap recombination contribution observed in those regions. If the optical intensity is concentrated in the periphery of the rod, photoexcited carriers will be produced in the surface depletion zone (Figure 7F). The internal field present in this region (i.e., band bending) would separate the electrons and holes, resulting in a greater degree of carrier trapping and longer recombination times.

Near the tips of the rod, photoexcited carriers may be preferentially produced in the cores of the structure. This may simply result from a greater degree of scattering off the rough surfaces at the tip, resulting in a more spatially homogeneous intensity distribution. Another possibility suggested by the simulations is that for smaller resonator sizes, the intensity distribution has significant standing wave character, consistent with FP modes (Figure 7C), suggesting a greater density of photoexcited carriers will be produced in the core of the structure (Figure 7E). Regardless of the relative contributions of these two effects, both suggest that carriers in the tips will be produced in the central region of the rod. Because of the low carrier mobility, electrons and holes created in this zone would remain there, and experience a lattice environment similar to that of the bulk, accounting for the greater degree of recombination observed at the band edge.

Our experiments suggest that in this mesoscale size regime, light can couple into resonator modes, resulting in nonuniform excitation and spatially dependent dynamics. Although such modes have been discussed extensively,[12−19] the role they play in shaping dynamical behavior has remained largely unexplored.

4. CONCLUSIONS

We have used femtosecond pump−probe microscopy to investigate the charge recombination dynamics at different points within a single needle-shaped ZnO rod. We find dramatically faster recombination in the tips of the rod that occurs through excitonic or electron−hole plasma states. Photoexcitation in the larger diameter sections of the interior exhibit much slower recombination, which proceeds primarily through defects sites, i.e., trap mediated recombination. Direct imaging of the excitation cloud using a spatially separated pump−probe method indicates that carrier diffusion in the excitation volume is not important in these experiments. Finite element simulations suggest that the spatial variation observed in the carrier recombination dynamics is the result of optical resonator modes, which produce qualitatively different intensity patterns in the two different locations. The intensity pattern near the end of the rod has significant standing-wave character, which leads to the creation of photoexcited carriers in the core of the structure. The larger diameter regions, on the other hand, exhibit intensity distributions in which the WG mode character dominates. At these locations, the photoexcited carriers are produced in subsurface depletion zones, where the internal fields separate the electrons and holes and lead to a greater degree of trap recombination on longer time scales. Although cavity resonator modes are known to alter steady-state optical properties, their impact on the carrier dynamics has not been extensively discussed.

AUTHOR INFORMATION

Corresponding Author

*Phone: (919) 962-1619. E-mail: John_Papanikolas@unc.edu.

Notes

The authors declare no competing financial interest.

ACKNOWLEDGMENTS

Funding for this project came from a grant from the National Science Foundation (CHE-0809045). The project also made use of instrumentation purchased by the UNC-EFRC Center for Solar Fuels, an Energy Frontier Research Center funded by the U.S. Department of Energy, Office of Science, Office of Basic Energy Sciences, under Award Number DE-SC0001011.

REFERENCES

(1) Yoffe, A. D. *Adv. Phys.* **2002**, *51*, 799−890.
(2) Allen, M. W.; Swartz, C. H.; Myers, T. H.; Veal, T. D.; McConville, C. F.; Durbin, S. M. *Phys. Rev. B* **2010**, *81*.
(3) Tay, Y. Y.; Tan, T. T.; Boey, F.; Liang, M. H.; Ye, J.; Zhao, Y.; Norby, T.; Li, S. *Phys. Chem. Chem. Phys.* **2010**, *12*, 2373−2379.
(4) Vanmaekelbergh, D.; van Vugt, L. K. *Nanoscale* **2011**, *3*, 2783−2800.
(5) Yang, P. D.; Gargas, D. J.; Moore, M. C.; Ni, A.; Chang, S. W.; Zhang, Z. Y.; Chuang, S. L. *Acs Nano* **2010**, *4*, 3270−3276.
(6) Ruhle, S.; van Vugt, L. K.; Li, H. Y.; Keizer, N. A.; Kuipers, L.; Vanmaekelbergh, D. *Nano Lett.* **2008**, *8*, 119−123.
(7) Zimmler, M. A.; Bao, J.; Capasso, F.; Muller, S.; Ronning, C. *Appl. Phys. Lett.* **2008**, *93*, 051101−051104.
(8) van Vugt, L. K.; Ruhle, S.; Ravindran, P.; Gerritsen, H. C.; Kuipers, L.; Vanmaekelbergh, D. *Phys. Rev. Lett.* **2006**, *97*, 147401−147405.
(9) Ozgur, U.; Alivov, Y. I.; Liu, C.; Teke, A.; Reshchikov, M. A.; Dogan, S.; Avrutin, V.; Cho, S. J.; Morkoc, H. *J. Appl. Phys.* **2005**, *98*, 041301−041404.
(10) Djurisic, A. B.; Leung, Y. H. *Small* **2006**, *2*, 944−961.
(11) Wang, Z. L. *J. Phys.: Condens. Matter* **2004**, *16*, R829−R858.
(12) Nobis, T.; Grundmann, M. *Phys. Rev. A* **2005**, *72*, 063806−063817.
(13) Nobis, T.; Kaidashev, E. M.; Rahm, A.; Lorenz, M.; Grundmann, M. *Phys. Rev. Lett.* **2004**, *93*, 103903−103907.
(14) Czekalla, C.; Nobis, T.; Rahm, A.; Cao, B. Q.; Zuniga-Perez, J.; Sturm, C.; Schmidt-Grund, R.; Lorenz, M.; Grundmann, M. *Phys. Status Solidi B* **2010**, *247*, 1282−1293.
(15) Yang, Y. H.; Dong, J. W.; Wang, N. W.; Yang, G. W. *J. Appl. Phys.* **2011**, *109*, 093511−093517.
(16) Yang, Y. H.; Zhang, Y.; Wang, N. W.; Wang, C. X.; Li, B. J.; Yang, G. W. *Nanoscale* **2011**, *3*, 592−597.
(17) Liu, J. Z.; Lee, S.; Ahn, Y. H.; Park, J. Y.; Koh, K. H.; Park, K. H. *Appl. Phys. Lett.* **2008**, *92*, 263102−263105.
(18) Sun, L. X.; Chen, Z. H.; Ren, Q. J.; Yu, K.; Bai, L. H.; Zhou, W. H.; Xiong, H.; Zhu, Z. Q.; Shen, X. C. *Phys. Rev. Lett.* **2008**, *100*, 156403−156407.
(19) Kirschbrown, J. R.; House, R. L.; Mehl, B. P.; Gabriel, M. M.; Parker, J. K.; Papanikolas, J. M. *J. Phys. Chem. C* **2011**, manuscript in preparation.
(20) House, R. L.; Mehl, B. P.; Kirschbrown, J. R.; Barnes, S. C.; Papanikolas, J. M. *J. Phys. Chem. C* **2011**, *115*, 10806−10816.
(21) House, R. L.; Kirschbrown, J. R.; Mehl, B. P.; Gabriel, M. M.; Puccio, J. A.; Parker, J. K.; Papanikolas, J. M. *J. Phys. Chem. C* **2011**, *115*, 21436−21442.
(22) Mehl, B. P.; House, R. L.; Uppal, A.; Reams, A. J.; Zhang, C.; Kirschbrown, J. R.; Papanikolas, J. M. *J. Phys. Chem. A* **2010**, *114*, 1241−1246.
(23) Mehl, B. P.; Kirschbrown, J. R.; House, R. L.; Papanikolas, J. M. *J. Phys. Chem. Lett.* **2011**, *2*, 1777−1781.
(24) Cheng, B.; Samulski, E. T. *Chem. Commun.* **2004**, 986−987.
(25) Li, F.; Li, Z.; Jin, F. J. *Mater. Lett.* **2007**, *61*, 1876−1880.

(26) Zipfel, W. R.; Williams, R. M.; Webb, W. W. *Nat. Biotechnol.* **2003**, *21*, 1368−1376.
(27) Johnson, J. C.; Yan, H. Q.; Yang, P. D.; Saykally, R. J. *J. Phys. Chem. B* **2003**, *107*, 8816−8828.
(28) Hendry, E.; Koeberg, M.; Bonn, M. *Phys. Rev. B* **2007**, *76*, 045214−045220.
(29) Mitsubori, S.; Katayama, I.; Lee, S. H.; Yao, T.; Takeda, J. *J. Phys.: Condens. Matter* **2009**, *21*, 064211−064216.
(30) Song, J. K.; Willer, U.; Szarko, J. M.; Leone, S. R.; Li, S.; Zhao, Y. *J. Phys. Chem. C* **2008**, *112*, 1679−1684.
(31) Yamamoto, A.; Kido, T.; Goto, Y. F.; Chen, Y.; Yao, T.; Kasuya, A. *Appl. Phys. Lett.* **1999**, *75*, 469−471.
(32) Lin, J. H.; Chen, Y. J.; Lin, H. Y.; Hsieh, W. F. *J. Appl. Phys.* **2005**, *97*, 033526−033532.
(33) Klingshirn, C. F. *Semiconductor optics*, 3rd ed.; Springer: Berlin, New York, 2007.
(34) Bauer, C.; Boschloo, G.; Mukhtar, E.; Hagfeldt, A. *Chem. Phys. Lett.* **2004**, *387*, 176−181.
(35) Okamoto, K.; Fujita, S.; Kawakami, Y.; Scherer, A. *Phys. Status Solidi B* **2003**, *240*, 368−371.
(36) Okamoto, K.; Inoue, K.; Kawakami, Y.; Fujita, S.; Terazima, M.; Tsujimura, A.; Kidoguchi, I. *Rev. Sci. Instrum.* **2003**, *74*, 575−577.
(37) Okamoto, K.; Scherer, A.; Kawakami, Y. *Appl. Phys. Lett.* **2005**, *87*, 161104−161107.
(38) Said, A. A.; Sheikbahae, M.; Hagan, D. J.; Wei, T. H.; Wang, J.; Young, J.; Vanstryland, E. W. *J. Opt. Soc. Am. B* **1992**, *9*, 405−414.

THE JOURNAL OF PHYSICAL CHEMISTRY Letters

LETTER

pubs.acs.org/JPCL

The End Is Different than The Middle: Spatially Dependent Dynamics in ZnO Rods Observed by Femtosecond Pump−Probe Microscopy

Brian P. Mehl, Justin R. Kirschbrown, Ralph L. House, and John M. Papanikolas*

Department of Chemistry, Caudill Laboratories, University of North Carolina at Chapel Hill, Chapel Hill, North Carolina 27599, United States

ABSTRACT: Pump−probe transient absorption microscopy was used to follow the electron−hole (e−h) recombination dynamics at different points within individual needle-shaped ZnO rods to characterize spatial differences in dynamical behavior. The results from pump−probe experiments are correlated with spatially resolved ultrafast emission measurements, and scanning electron microscopy provides structural details. Dramatically different e−h recombination dynamics are observed in the narrow tips compared to the interior, with the ends exhibiting a greater propensity for electron−hole plasma (EHP) formation and faster recombination of carriers across the band gap that stem from a physical confinement of the charge carriers. In the interior of the rod, a greater fraction of the e−h recombination is trap-mediated and occurs on a significantly longer time scale.

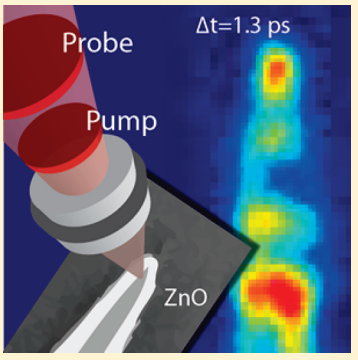

SECTION: Kinetics, Spectroscopy

The polydispersity intrinsic to nanoscale and microscale semiconductor materials poses a major challenge to using individual objects as building blocks for device applications. Early work showed that surfaces, which trap mobile carriers, result in band bending and internal electric fields that give rise to significant variation in the electronic and photophysical behavior from one object to the next. Modern nanomaterials have moved beyond simple particles, and the complex geometrical architectures that are available (e.g., needles, ribbons, tetrapods) have both expanded the range of potential applications and raised new questions regarding the connection between shape and function.[1] This report addresses a fairly simple one: Can different locations within a single structure exhibit different dynamical signatures? Do the ends of a rod behave differently than the middle? Spatial differences can arise from a variety of physical sources and mechanisms. Carrier confinement in the sharp features of high-aspect structures and variation in defect density are two examples. Both would influence carrier relaxation and could result in behavior that differs from one location to another. While such effects are easy to envision, experimental observation requires techniques with combined spatial and temporal resolution.

The pursuit of such methods is not new, and time-resolved optical microscopies have been applied to the study of a wide variety of problems. The most common are luminescence-based approaches, which are the simplest to implement but are limited to the study of phenomena on the picosecond time scale.[2] Pump−probe methods can follow dynamics on faster time scales; however, incorporation into microscopy is more difficult, and far fewer examples exist. While near-field and scanning probe microscopies offer the greatest spatial resolution, their combination with pump−probe methods significantly increases the experimental complexity.[3−5] In this respect, far-field methods are more attractive, and a few examples have begun to appear on a variety of systems and materials.[6−15] While several studies of carrier dynamics in semiconductor particles achieved femtosecond time resolution, their spatial resolution was lower than the diffraction limit, and the excitation of whole structures generated carriers throughout the object.[6−9]

Exposing dynamical differences from point to point requires localized excitation with high lateral resolution. Spatially localized excitation in pump−probe microscopy has been reported in just a few cases, including the study of graphene sheets,[10] semiconductor nanowires,[11] molecular crystals,[12] and composite materials.[13−15] The greatest spatial variation was observed in composites, which stemmed from distinct chemical domains, while the nanomaterials exhibited only slight differences from one point to the next. Here, we combine pump−probe methods with far-field microscopy to study the spatial variation of the electron−hole (e−h) recombination dynamics in needle-shaped ZnO rods on a femtosecond time scale with high lateral resolution (350 nm). Time-resolved images show significant variation in the dynamical response, with the ends of the rods exhibiting dramatically faster e−h recombination than at points in the interior.

The ability to manipulate the shape of ZnO structures is enormous, and through a variety of synthetic methods, many different structural forms have been demonstrated, making it an ideal material for studying shape-dependent phenomena. The rods used in this work were grown using solution-based methods by incubating a 0.05 M solution of $Zn(NO_3)_2$ and methenamine ($(CH_2)_6N_4$) under hydrothermal conditions for 3 h at 150 °C.[16] The resulting structures were sonicated in ethanol to disperse aggregates, drop-cast onto a microscope slide, and then annealed at 550 °C to reduce the overall defect density.[17]

Received: June 15, 2011
Accepted: June 30, 2011
Published: June 30, 2011

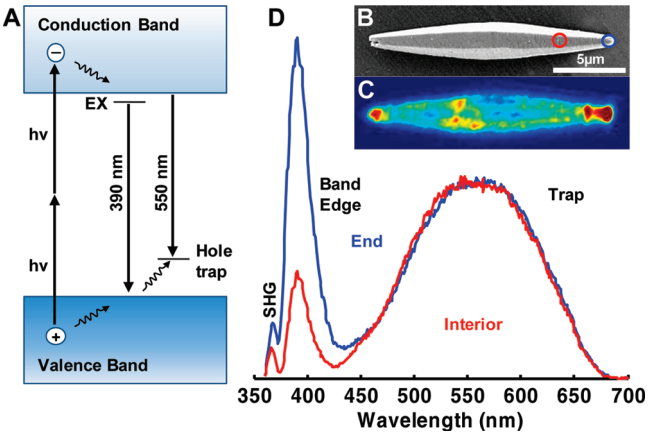

Figure 1. (A) Illustration of ZnO band structure depicting two-photon excitation, band-edge emission at 390 nm from an exciton state (EX), and trap-mediated emission at 550 nm. (B) SEM image of a typical structure; circles indicate locations of spectroscopic measurements. (C) Band-edge emission image obtained by raster scanning the focused excitation laser across the rod. (D) Emission spectra observed at a point near the end of the rod (blue circle in (B)) and within the interior (red circle in (B)). Spectra show the band-edge, trap emission and second-harmonic generation (SHG).

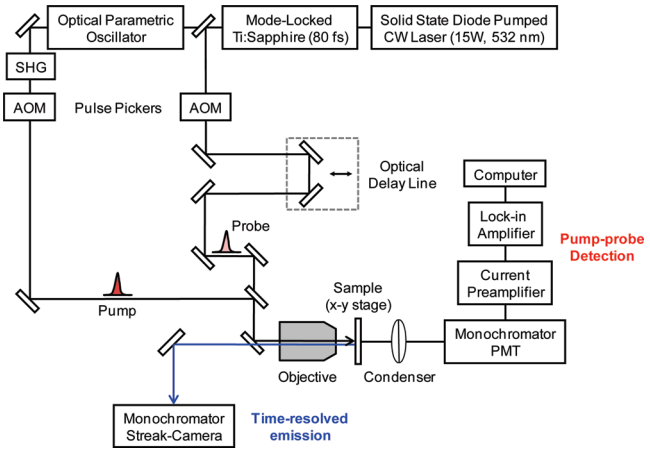

Figure 2. Schematic diagram of a two-photon pump−probe microscope. The frequency-doubled output of an optical parametric oscillator (OPO) at 730 nm is directed on the back aperture of the microscope objective and focused to a diffraction-limited spot at the sample. Imaging is achieved by raster scanning the sample stage across the focused laser spot and monitoring the emission collected by the objective. The lateral resolution is approximately 350 nm. Pump−probe microscopy incorporates a second laser beam focused onto the location of the excitation beam. The beam that emerges from the sample is collected by a condenser lens, and its intensity is monitored by lock-in detection. Two acousto-optic modulators (AOM) are used to reduce the repetition rate of the laser to 1.6 MHz. Time-resolved emission measurements are performed by monitoring the emission intensity using a streak camera.

Photoexcitation of ZnO by a single UV photon (or simultaneous two-photon excitation in the near-infrared) promotes electrons from the valence band to the conduction band, resulting in free charge carriers (Figure 1A). These free carriers can either associate into excitons that lie just below the conduction band edge or become trapped at defect sites in the crystal lattice. Exciton recombination results in a UV−blue emission that is centered at 390 nm, while defect emission gives rise to a broad visible emission band centered at 550 nm.[18]

A schematic diagram of the nonlinear microscope used in this work is displayed in Figure 2. Individual rods are excited by a 730 nm femtosecond laser pulse (1 nJ/pulse) generated by the frequency-doubled output of an optical parametric oscillator (OPO). The excitation pulse is focused to a diffraction-limited spot by a microscope objective, resulting in a two-photon absorption that creates charge carriers in a localized region of the structure. On the basis of the magnitude of the two-photon cross section,[19] we estimate that the pump pulse produces $\sim 10^{20}$ carriers/cm^3. Emission is then collected in the backward-scattered direction by the objective and focused onto the slit of a scanning monochromator and photomultiplier tube. Two-photon emission imaging is achieved by raster scanning the sample across the focal point of the objective with a piezoelectric nanopositioning stage. The spatial resolution of the two-photon microscope is determined by the size of the laser spot at the focus of the objective. Because two-photon absorption scales with the square of the optical intensity, efficient excitation occurs only at the focus, resulting in confocal-like behavior and a lateral excitation dimension that is smaller than the diffraction limit. For our microscope, the spatial extent of the excitation is approximately 350 nm.

Shown in Figure 1B is the scanning electron microscopy (SEM) image of a typical rod used in this work. The structures vary in length from 15 to 20 μm and have faceted hexagonal cross sections with tapered ends (Figure 1B). We have developed the protocols for locating objects found in the SEM in the optical microscope, which enable us to correlate the photophysical observations with detailed structural information. The two-photon emission image shown in Figure 1C depicts the 390 nm band-edge emission from the same rod. The image shows significant variation in the intensity across the structure, with the most prominent features being bright emission from the rod ends and enhanced emission along the vertices and outer facets. The modulated intensity within the interior of the rod is attributed to the influence of Fabry−Perot and whispering gallery cavity modes supported within the hexagonal cross section of the rod that concentrate the optical field at certain points within the structure.[20−22]

Spectroscopic measurements are performed by positioning the excitation spot at specific points. Photoluminescence spectra obtained at two different locations (Figure 1D) show both the characteristic narrow exciton and broad trap emission bands. The relative intensities of the two emission bands vary across the structure, with the end showing a more intense band-edge emission that suggests a greater propensity for e−h recombination across the band gap at that location.

Transient absorption microscopy incorporates a second laser pulse (810 nm, 50 pJ) focused onto the position of the excitation spot by the objective (Figure 2). The probe beam is collected by a condenser lens and focused onto the entrance slit of a monochromator and detected by a photomultiplier tube. A long-pass filter placed before the monochromator rejects unwanted pump light. An optical chopper modulates the excitation beam at 4 kHz, and pump-induced changes in the intensity of the probe pulse are monitored by a digital lock-in amplifier. The pump and probe polarizations were parallel to each other and oriented perpendicular to the long axis of the rod. The time resolution of the microscope is ~500 fs.

Pump−probe microscopy data are shown in Figure 3 for two different rods, denoted **R1** and **R2**. Transient absorption ($\Delta I/I$)

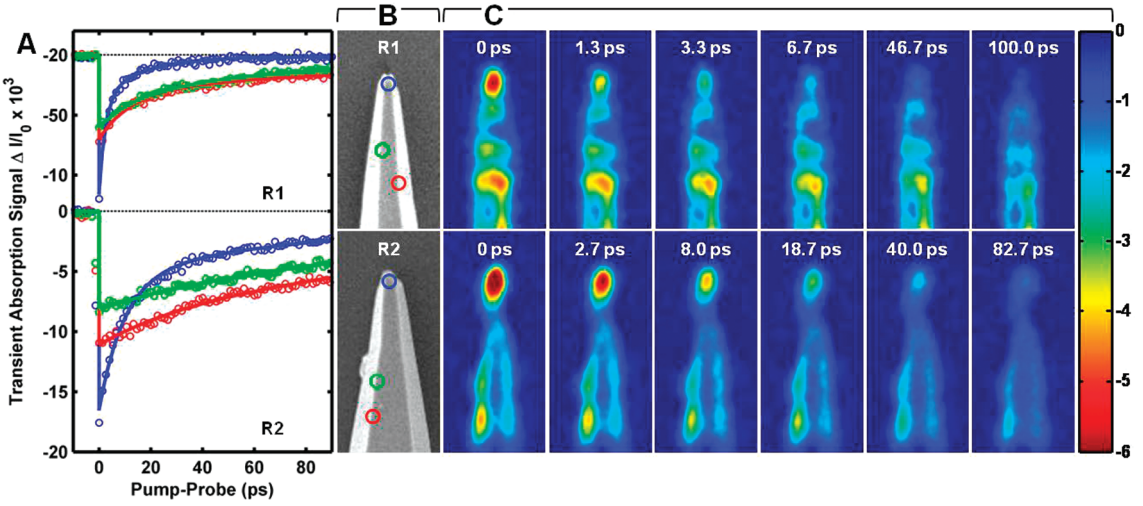

Figure 3. (A) Pump−probe transients ($\Delta I/I_0$) collected from the end (blue) and two different points within the interior (green and red) from two different rods, **R1** and **R2**. The locations of the collected points for the three transients are indicated in the corresponding SEM images (B), where the horizontal dimension of each image is 3 μm. The transients exhibit complex decay kinetics with fast (<30 ps), intermediate (100−200 ps), and long (>500 ps) components, whose relative amplitudes depend on position. While the interior exhibits all three components, with the fastest contributing only 25−50% of the total amplitude, the ends are dominated by this component, which accounts for 60−100% of the amplitude. (C) A series of transient absorption images (ΔI) obtained at different pump−probe delays for the two rods. The series of pump−probe images show the rapid loss of the signal at the rod end, which ultimately decays to zero signal, while response from the interior persists significantly longer.

data for three different points in each rod are displayed (Figure 3A), and colored circles on the corresponding SEM images (Figure 3B) indicate their locations. The negative-going signal signifies a pump-induced decrease in probe intensity. The pump−probe signals include contributions from an induced absorption arising from near-infrared excitation of free carriers[23] and a Kerr lensing contribution stemming from a spatial variation in the index of refraction due to the localized charge carrier distribution produced by excitation.[19] The magnitude of both contributions depends on the presence of free carriers, and the decay of the pump−probe signal is attributed to a decrease in their concentration due to recombination and trapping events.

The electronic dynamics at the end of the rod differ dramatically from those observed at the interior, with the ends showing typically more intense signals with generally faster recombination rates than any other point in the structure. Spatial variation in the e−h recombination is particularly apparent in images obtained by fixing the pump−probe delay and monitoring ΔI as a function of position (Figure 3C). At early delays, the largest signal appears at the end of the rod. Less intense but localized regions of increased signal that coincide with the vertices are also observed. This modulation in the signal intensity is likely the result of cavity modes supported within the cross section of the structure.[20−22] At longer delays, the bright spot at the end diminishes, becoming less intense than the interior and eventually disappearing. Although there are examples of pump−probe microscopy that reveal differences from structure to structure, this is the first time that significant spatial variation in the dynamical response of an individual object has been observed.

Transient photoluminescence provides a direct view of the band-edge and trap-mediated e−h recombination processes. A spectral−temporal intensity map (Figure 4A) of the time-resolved emission data collected from the end of a third rod, **R3**, shows a rich evolution of the band-edge emission, which shifts to the blue as it decays during the first 15−20 ps. Horizontal slices through the map correspond to snapshots of the emission spectrum at different times. The emission band appears with $\lambda_{max} \approx 400$ nm and then narrows as it blue shifts to a limiting position of 390 nm.

Spectral shifts of this type are one signature of the electron−hole plasma (EHP) emission that occurs at high excitation intensities in II−IV semiconductors.[24] When the carrier density exceeds the Mott threshold, Coulombic and exchange interactions weaken the exciton binding and reduce the band gap (i.e., band gap renormalization). This phenomenon gives rise to a collective EHP state with an intense, red-shifted emission relative to the exciton. As electrons and holes recombine, the charge carrier density decreases, and the excitonic state resumes, resulting in the time-dependent blue shift in the emission spectrum. The EHP to exciton transition that occurs during the first 15−20 ps is consistent with observations in bulk and nanostructured ZnO.[25,26] Similar measurements performed at the interior show a significantly smaller spectral shift (Figure 4B) and decreased propensity for EHP formation compared to the end.

Vertical slices through this surface provide the photoluminescence decay (Figure 4C,D). The band-edge emission at the end of the rod decays with 22 and 88 ps components (τ_{avg} = 30 ps). The faster component is assigned to EHP recombination. The slower component is attributed to exciton emission, which emerges as the carrier density decreases and the exciton becomes most stable. The presence of the fast component in the interior is less obvious, and the slightly slower (τ_{avg} = 55 ps) decay is consistent with a smaller contribution from EHP recombination.

The decays of the pump−probe and trap emission are similar to each other at two locations (Figure 4C,D) but differ in their relationship to the band-edge emission. At the end of the rod, they match the decay of the band-edge emission at early times, suggesting that band-edge recombination is the primary cause of the decay in the free carrier population. In the tips of the rods, where the diameter is comparable to the size of the excitation spot (~350 nm), physical confinement of the charge carriers leads to a prolonged overlap of the electron and hole

dx.doi.org/10.1021/jz200809c | J. Phys. Chem. Lett. 2011, 2, 1777–1781

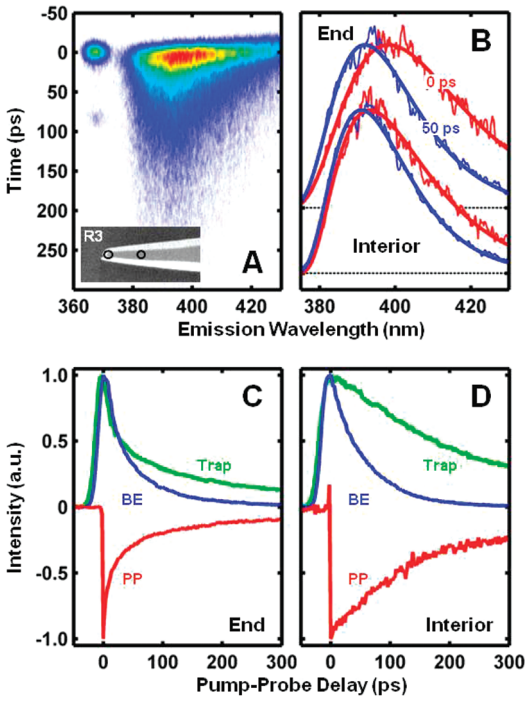

Figure 4. (A) Spectral−temporal intensity map of the emission collected from the end of the rod (**R3**) and detected using a streak camera. The main feature is the band-edge emission; the narrow peak at 365 nm is the second harmonic of the excitation pulse and provides the instrument response (17 ps). The inset shows the SEM image and locations of spectroscopic measurements (end versus interior). The vertical dimension of the SEM image is 3 μm. (B) Time-resolved spectra obtained at 0 (red) and 50 ps (blue) from the end of the rod (upper set) and interior (lower set). (C,D) Comparison of the band-edge (BE), trap emission, and pump−probe (PP) data collected at the two points.

wave functions, increasing the propensity for EHP formation and band-edge recombination. The interior is qualitatively different, however. Here, the band-edge emission decays more quickly compared to the pump−probe and trap emission, indicating that a significant free carrier population persists following the initial band-edge recombination events. At interior sites, carriers can migrate out of the excitation volume, either due to diffusion or internal fields arising from depletion zones. Expansion of the charge cloud and the spatial separation of electrons and holes would make EHP formation more difficult, suppress band-edge recombination (consistent with the emission spectra, Figure 1D), and lead to slower recombination.

The spatial dependence in the e−h dynamics correlates with the structure's size in the vicinity of the excitation. Transient absorption data collected across a series of structures show recombination rates that depend on the size of the rod, with smaller ends showing faster decays. The three structures depicted in Figures 2 and 3 represent a range of taper sizes found in our samples. With a 406 nm diameter at the end, **R1** has a sharper taper than **R2** (690 nm) or **R3** (518 nm). The trend in recombination times is clearly evident for the three rods, where the 3 ps recombination in the sharper tip of **R1** is significantly faster than that observed in **R2** (10 ps) or **R3** (9 ps).

While heterogeneous behavior in nanomaterials is often ascribed to polydispersity and variation between structures is observed here too, the presence of different dynamical behaviors from different parts of the same object cannot be overlooked.

EXPERIMENTAL METHODS

A schematic diagram of the nonlinear microscope is displayed in Figure 2. The excitation pulse at 730 nm is generated from the frequency-doubled output of an optical parametric oscillator (Spectra-Physics: OPAL) pumped from a femtosecond mode-locked Ti:Sapphire laser (Spectra-Physics: Tsunami) at 810 nm. Imaging is achieved by raster scanning the sample across the focal point of the objective with a piezoelectric nanopositioning stage (Queensgate Instruments: NPS-XY-100A). The spatial resolution of the two-photon microscope is approximately 350 nm.

Pump−probe microscopy is achieved by picking off a small portion of the Ti:Sapphire output with a beam sampler for use as the probe pulse. Two acousto-optic modulator pulse pickers (Gooch and Housego) reduce the repetition rates of the pump and probe beams to 1.6 MHz to ensure complete relaxation before the next pump−probe pulse pair arrives. A motorized linear stage (Newport: ILS250CCHA) is inserted into the path of the probe beam to control the time delay between excitation and probe pulses. Both beams are focused to a diffraction-limited spot by an objective (Olympus MSPlan 50×, NA 0.8) placed below the sample plane. The probe beam is collected by a condenser lens and focused onto the entrance slit of a monochromator (Spectral Products: CM110) and detected by a photomultiplier tube (Hamamatsu: R928) and current preamplifier (Stanford Research System: SR570). A long-pass filter (Semrock: LP02-785RS) placed before the monochromator rejects unwanted pump light. An optical chopper modulates the excitation beam at 4 kHz, and pump-induced changes in the intensity of the probe pulse are monitored by a digital lock-in amplifier (Stanford Research Systems: SR830). Analog data acquisition (National Instruments PCI-6221) is handled in conjunction with MATLAB. The microscope can measure $\Delta I/I$ as low as 10^{-4}. The pump and probe polarizations are parallel to each other and oriented perpendicular to the long axis of the rod.

A convenient measure of the transient absorption experimental time resolution involves monitoring the sum frequency generated within ZnO from the overlap of the pump and probe beams. The cross correlation of the pump and probe beams monitored at the 384 nm is measured to have a full width at half-maximum of 520 fs.

In the time-resolved fluorescence measurements, light emanating from the sample is re-collected by the objective, transmitted through a dichroic beam splitter (Semrock: FF670), and focused onto the entrance slit of a streak camera (Hamamatsu: Streakscope). The instrument response of the streak camera is approximately 17 ps.

AUTHOR INFORMATION

Corresponding Author

*E-mail: john_papanikolas@unc.edu.

ACKNOWLEDGMENT

Primary funding for this project came from a grant from the National Science Foundation (CHE-0809045). The project also made use of instrumentation purchased by the UNC-EFRC on Solar Fuels and Next Generation Photovoltaics, an Energy Frontier Research Center funded by the U.S. Department of Energy, Office of Science, Office of Basic Energy Sciences under Award Number DE-SC0001011.

REFERENCES

(1) Djurisic, A. B.; Leung, Y. H. Optical Properties of ZnO Nanostructures. *Small* **2006**, *2*, 944–961.

(2) Suhling, K.; French, P. M. W.; Phillips, D. Time-Resolved Fluorescence Microscopy. *Photochem. Photobiol. Sci.* **2005**, *4*, 13–22.

(3) Okamoto, K.; Scherer, A.; Kawakami, Y. Near-Field Scanning Optical Microscopic Transient Lens for Carrier Dynamics Study in InGaN/GaN. *Appl. Phys. Lett.* **2005**, *87*, 161104.

(4) Terada, Y.; Yoshida, S.; Takeuchi, O.; Shigekawa, H. Real-Space Imaging of Transient Carrier Dynamics by Nanoscale Pump−Probe Microscopy. *Nat. Photonics* **2010**, *4*, 869–874.

(5) Anderson, A.; Deryckx, K. S.; Xu, X. J. G.; Steinmeyer, G.; Raschke, M. B. Few-Femtosecond Plasmon Dephasing of a Single Metallic Nanostructure from Optical Response Function Reconstruction by Interferometric Frequency Resolved Optical Gating. *Nano Lett.* **2010**, *10*, 2519–2524.

(6) Gundlach, L.; Piotrowiak, P. Femtosecond Kerr-Gated Wide-Field Fluorescence Microscopy. *Opt. Lett.* **2008**, *33*, 992–994.

(7) Djurisic, A. B.; Kwok, W. M.; Leung, Y. H.; Phillips, D. L.; Chan, W. K. Stimulated Emission in ZnO Nanostructures: A Time-Resolved Study. *J. Phys. Chem. B* **2005**, *109*, 19228–19233.

(8) Song, J. K.; Willer, U.; Szarko, J. M.; Leone, S. R.; Li, S.; Zhao, Y. Ultrafast Upconversion Probing of Lasing Dynamics in Single ZnO Nanowire Lasers. *J. Phys. Chem. C* **2008**, *112*, 1679–1684.

(9) Johnson, J. C.; Knutsen, K. P.; Yan, H. Q.; Law, M.; Zhang, Y. F.; Yang, P. D.; Saykally, R. J. Ultrafast Carrier Dynamics in Single ZnO Nanowire and Nanoribbon Lasers. *Nano Lett.* **2004**, *4*, 197–204.

(10) Huang, L. B.; Hartland, G. V.; Chu, L. Q.; Luxmi; Feenstra, R. M.; Lian, C. X.; Tahy, K.; Xing, H. L. Ultrafast Transient Absorption Microscopy Studies of Carrier Dynamics in Epitaxial Graphene. *Nano Lett.* **2010**, *10*, 1308–1313.

(11) Carey, C. R.; Yu, Y. H.; Kuno, M.; Hartland, G. V. Ultrafast Transient Absorption Measurements of Charge Carrier Dynamics in Single II−VI Nanowires. *J. Phys. Chem. C* **2009**, *113*, 19077–19081.

(12) Fujino, T.; Fujima, T.; Tahara, T. Femtosecond Fluorescence Dynamics Imaging Using a Fluorescence up-Conversion Microscope. *J. Phys. Chem. B* **2005**, *109*, 15327–15331.

(13) Fu, D.; Ye, T.; Matthews, T. E.; Grichnik, J.; Hong, L.; Simon, J. D.; Warren, W. S. Probing Skin Pigmentation Changes with Transient Absorption Imaging of Eumelanin and Pheomelanin. *J. Biomed. Opt.* **2008**, *13*, 054036.

(14) Polli, D.; Grancini, G.; Clark, J.; Celebrano, M.; Virgili, T.; Cerullo, G.; Lanzani, G. Nanoscale Imaging of the Interface Dynamics in Polymer Blends by Femtosecond Pump−Probe Confocal Microscopy. *Adv. Mater.* **2010**, *22*, 3048–3051.

(15) Cadby, A.; Dean, R.; Fox, A. M.; Jones, R. A. L.; Lidzey, D. G. Mapping the Fluorescence Decay Lifetime of a Conjugated Polymer in a Phase-Separated Blend Using a Scanning near-Field Optical Microscope. *Nano Lett.* **2005**, *5*, 2232–2237.

(16) Cheng, B.; Shi, W. S.; Russell-Tanner, J. M.; Zhang, L.; Samulski, E. T. Synthesis of Variable-Aspect-Ratio, Single-Crystalline ZnO Nanostructures. *Inorg. Chem.* **2006**, *45*, 1208–1214.

(17) House, R. L.; Mehl, B. P.; Kirschbrown, J. R.; Barnes, S. C.; Papanikolas, J. M. Characterizing the Ultrafast Charge Carrier Trapping Dynamics in Single ZnO Rods Using Two-Photon Emission Microscopy. *J. Phys. Chem. C* **2011**, *115*, 10806–10816.

(18) Ozgur, U.; Alivov, Y. I.; Liu, C.; Teke, A.; Reshchikov, M. A.; Dogan, S.; Avrutin, V.; Cho, S. J.; Morkoc, H. A Comprehensive Review of ZnO Materials and Devices. *J. Appl. Phys.* **2005**, *98* 041301.

(19) Lin, J. H.; Chen, Y. J.; Lin, H. Y.; Hsieh, W. F. Two-Photon Resonance Assisted Huge Nonlinear Refraction and Absorption in ZnO Thin Films. *J. Appl. Phys.* **2005**, *97*, 033526.

(20) Mehl, B. P.; House, R. L.; Uppal, A.; Reams, A. J.; Zhang, C.; Kirschbrown, J. R.; Papanikolas, J. M. Direct Imaging of Optical Cavity Modes in ZnO Rods Using Second Harmonic Generation Microscopy *J. Phys. Chem. A* **2010**, *114*, 1241–1246.

(21) Johnson, J. C.; Yan, H. Q.; Yang, P. D.; Saykally, R. J. Optical Cavity Effects in ZnO Nanowire Lasers and Waveguides. *J. Phys. Chem. B* **2003**, *107*, 8816–8828.

(22) Nobis, T.; Grundmann, M. Low-Order Optical Whispering-Gallery Modes in Hexagonal Nanocavities. *Phys. Rev. A* **2005**, *72*, 063806.

(23) Bauer, C.; Boschloo, G.; Mukhtar, E.; Hagfeldt, A. Ultrafast Relaxation Dynamics of Charge Carriers Relaxation in ZnO Nanocrystalline Thin Films. *Chem. Phys. Lett.* **2004**, *389*, 449–449.

(24) Klingshirn, C. F. *Zinc Oxide from Fundamental Properties Towards Novel Applications*, 1st ed.; Springer: Berlin, Germany, 2010.

(25) Yamamoto, A.; Kido, T.; Goto, Y. F.; Chen, Y.; Yao, T.; Kasuya, A. Dynamics of Photoexcited Carriers in ZnO Epitaxial Thin Films. *Appl. Phys. Lett.* **1999**, *75*, 469–471.

(26) Hendry, E.; Koeberg, M.; Bonn, M. Exciton and Electron−Hole Plasma Formation Dynamics in ZnO. *Phys. Rev. B* **2007**, *76*, 045214.

THE JOURNAL OF PHYSICAL CHEMISTRY C

Article

pubs.acs.org/JPCC

Hybrid Standing Wave and Whispering Gallery Modes in Needle-Shaped ZnO Rods: Simulation of Emission Microscopy Images Using Finite Difference Frequency Domain Methods with a Focused Gaussian Source

Justin R. Kirschbrown, Ralph L. House, Brian P. Mehl, James K. Parker,[†] and John M. Papanikolas*

Department of Chemistry, Caudill Laboratories, University of North Carolina at Chapel Hill, Chapel Hill, North Carolina 27599-3290, United States

ABSTRACT: Two-photon emission microscopy is used to investigate the photoluminescence properties of individual ZnO rods. The rods are 10−20 μm in length with a tapered cross section that varies from 1 to 2 μm at the midpoint to several hundred nanometers at the ends. The tapered shape and hexagonal cross section result in complex optical resonator modes that lead to periodic patterns in the two-photon emission image. Finite-difference frequency domain methods using a series of excitation sources, including focused Gaussian, point dipole, and plane wave, suggest that resonator modes have both standing wave (Fabry-Pérot) and whispering gallery mode character, whose relative contributions vary along the rod axis.

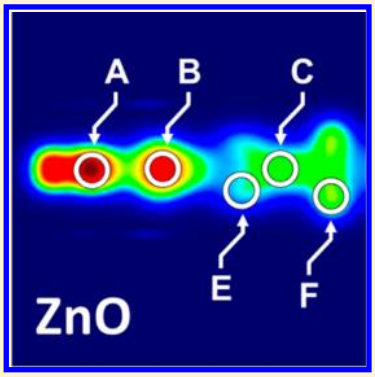

INTRODUCTION

Optical resonator modes appear as the dimensions approach the wavelength of light, impacting steady-state spectral properties. The ability to manipulate the structure of ZnO makes it an ideal material for shape dependent optical studies, and through a variety of facile synthetic methods many different forms have been produced, including nanorods with differing end morphologies, tetrapods, and nanohelices.[1−3] The simplest cavity resonances are longitudinal, standing-wave modes propagating along the long axis of ZnO nanorods, which have been described by several groups.[4−6] The size of the resonator determines the optical frequencies that are supported, which are often observed spectroscopically as a series of narrow resonances superimposed on the broader band-edge and trap emission bands.[7−15]

While longitudinal modes are clearly important to our understanding of the light−matter interactions of these structures, this work focuses on the cavity-modes supported within the hexagonal cross section and lie transverse to the rod axis. The faceted crystalline structures of these ZnO materials give rise to a rich variety of optical cavity modes. Previous reports describe these modes using two classic resonator pictures: Fabry-Pérot (FP) modes supported between two opposing parallel facets, and whispering gallery (WG) modes arising from the circulation of light around the periphery of rod through total internal reflection at each crystal face.[7−13,16,17]

We observed both types of resonances in second-harmonic and two-photon emission images obtained from tapered ZnO rods.[18−22] The rods are 10−20 μm in length and have faceted hexagonal cross sections with diameters that range from 1 to 3 μm at their widest point, down to 100−200 nm at the ends. Because the resonance conditions for both modes depend upon the diameter of the structure, and because of the tapered shape, a fixed excitation wavelength will go in and out of resonance as the source moves along the rod and the resonator diameter changes, resulting in a periodic intensity modulation along the long axis of the rod. This paper shows that while the classic FP and WG resonator models[7−12,16] reproduce the image features in a qualitative sense, finite-difference frequency-domain (FDFD) simulations indicate that the classical resonator models are overly simplistic. In this size regime (200−1000 nm diameter), the hexagonal resonator modes actually contain characteristics of both the FP and WG resonances, whose relative contributions vary with resonator size. At smaller sizes, the modes have primarily standing-wave character with much of the optical intensity located in the core of the structure. As the size is increased, the intensity distribution shifts to the periphery of the structure, becoming more WG-like in character. These two different mode types may explain the spatial variations in electron−hole recombination that are observed these structures. Pump−probe microscopy experiments from our lab[21,22] indicate that recombination in the tips of the rod proceeds through an electron−hole plasma state, suggesting that carriers are created in a bulk-like region of the rod, that is, the core. In the larger sections of the rod, electron−hole recombination is trap mediated, consistent with carriers being produced in the

Received: February 1, 2013
Revised: April 15, 2013
Published: April 16, 2013

   dx.doi.org/10.1021/jp4011907 | J. Phys. Chem. C 2013, 117, 10653−10660

depletion zone near the surface and undergoing rapid charge separation.

EXPERIMENTAL SECTION

Materials. ZnO rods were grown using hydrothermal methods adapted from previously published work.[23,24] An aqueous solution of $Zn(NO_3)_2$ (50 mM) and hexamethylenetetramine ($(CH_2)_6N_4$) (50 mM) was heated in a closed bomb to yield needle-shaped rods ranging from 5 to 30 μm in length and 0.3 to 2 μm in diameter. Size control was achieved by varying reaction temperature, time, and/or concentration. After cooling the reaction to room temperature, the structures were harvested and suspended in ethanol using ultrasonication to break up aggregates. Microscopy samples were prepared by drop-casting a 250 μL of the suspension onto a microscope slide with an etched reference grid. The grid facilitated the locating of the rod observed in the optical microscope in a scanning electron microscope for structural characterization. The ability to perform both optical and electron microscopy on the same structure allows photophysical observations to be correlated with detailed structural information.

Emission Imaging. Two-photon emission imaging was accomplished by combining an ultrafast laser source with a home-built far-field optical microscope (Figure 1A). The

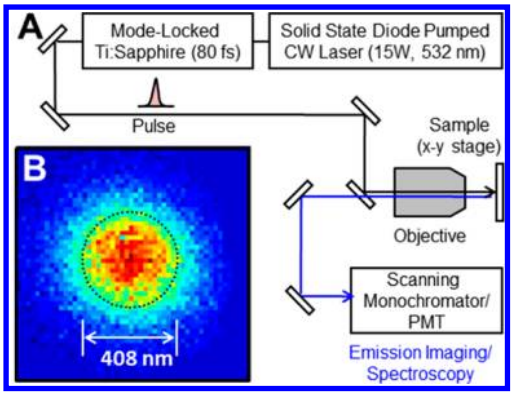

Figure 1. (A) Diagram of the two-photon emission microscope. The 730 nm output of a mode-locked Ti:Sapphire laser is directed onto the back aperture of the microscope objective (50×, 0.8 NA) and focused to a diffraction-limited spot at the sample. Imaging is achieved by raster scanning the sample stage across the focused laser spot and monitoring the emission collected by the objective with a scanning monochromator/PMT. (B) Two-photon emission image of a 100 nm quantum dot with 810 nm excitation. The size of the emission feature suggests that the lateral resolution at this wavelength is approximately 410 nm.

femtosecond laser source consisted of a mode-locked Ti:Sapphire laser (730 nm, 80 fs, 80 MHz) pumped by a solid-state diode-pumped Nd:YVO_4 laser. The laser output was directed onto the back aperture of a 50× microscope objective (0.8 NA), which focused it to a diffraction limited spot, resulting in two-photon excitation at a localized region of the ZnO rod. Light emanating from the structure was collected by the objective, passed through a dichroic beam splitter, and focused onto the slit of a monochromator and photomultiplier tube (PMT). Emission images were collected by raster scanning the sample across the focal point of the objective with a piezoelectric nanopositioning stage while monitoring the intensity of the emitted light. Imaging was performed without a coverslip under ambient conditions.

The spatial resolution of the microscope is determined by the size of the laser spot at the focus of the objective. Since two-photon absorption scales with the square of the optical intensity, efficient excitation occurs only at the focus, resulting in confocal-like behavior and a lateral excitation dimension that is smaller than the diffraction limit.[25] Emission images of a 100 nm quantum dot (Figure 1B) indicate that the spatial extent of excitation is 410 nm for the 810 nm excitation, which is slightly larger than the theoretical limits of 380 nm for this wavelength.[25] The spatial extent for 730 nm excitation is slightly less, about 380 nm.

RESULTS AND DISCUSSION

Two-Photon Emission Imaging. Characterization of the optical modes combines two-photon emission imaging with detailed structural information garnered from scanning electron microscopy (SEM). The SEM image of a typical needle-shaped structure is shown in Figure 2A. The rod has an overall length of 17 μm and a hexagonal cross section diameter (distance between parallel facets, d) that increases from 150 nm at the end to about 1 μm at the midpoint.

An individual structure is excited by a focused near-infrared laser pulse polarized parallel to the long-axis of the rod, resulting in a two-photon absorption that promotes carriers from the valence band to the conduction band in a localized region of the structure. Because ZnO is transparent in the near-infrared, two-photon absorption will occur throughout the excitation volume. Single UV photon absorption at 365 nm, by comparison, would occur within 100 nm of the surface. Free carriers produced by photoexcitation will either relax into excitons, resulting in the intense near-UV emission, or become trapped in defect sites, giving rise to the broad visible emission (Figure 2B).

Emission imaging is achieved by monitoring the photoluminescence intensity at a particular wavelength as a function of two-photon excitation position. Previous work in our lab showed that the majority of the emission detected emanates from the location of laser excitation, indicating that while coupling of light (either the excitation or emission) into wave-guiding modes propagating along the long axis of the rod does occur, it is relatively weak and contributes little to the observed emission at a given point.[19] A striking feature of images compiled from either band edge emission (λ_{em} = 390 nm) or trap emission (λ_{em} = 560 nm) is the axially symmetric intensity modulation along the length of the rod (Figure 2C, D). The emission spots appear along the middle of the rod at smaller diameters (labeled a−c and a′−c′ in Figure 2C), becoming two separate spots at larger diameters (f−h and f′−h′). We have observed similar patterns in both second-harmonic and two-photon emission images of other needle-shaped rods,[18,20] and reports of spatially periodic patterns in cathodoluminescence images of tapered wires have been shown previously.[7,8] Qualitatively, the patterns arise from optical resonator modes associated with a hexagonal cavity formed by the cross section of the rod. Because of the tapered structure, the cavity size changes along the long axis of the rod, causing the excitation wavelength to go in and out of resonance as the focused laser spot is moved along the rod. While in principle either the excitation or the emission wavelength could be resonant with the cavity, the qualitative similarity between the two images suggests that the excitation wavelength is largely responsible for the observed patterns.

Standing-Wave and Whispering Gallery Mode Descriptions. Generally, there are two types of optical modes: standing wave (Fabry-Pérot, FP) resonances that are supported between two parallel facets, and whispering gallery (WG) modes that correspond to propagation of light around the periphery of

dx.doi.org/10.1021/jp4011907 | J. Phys. Chem. C 2013, 117, 10653−10660

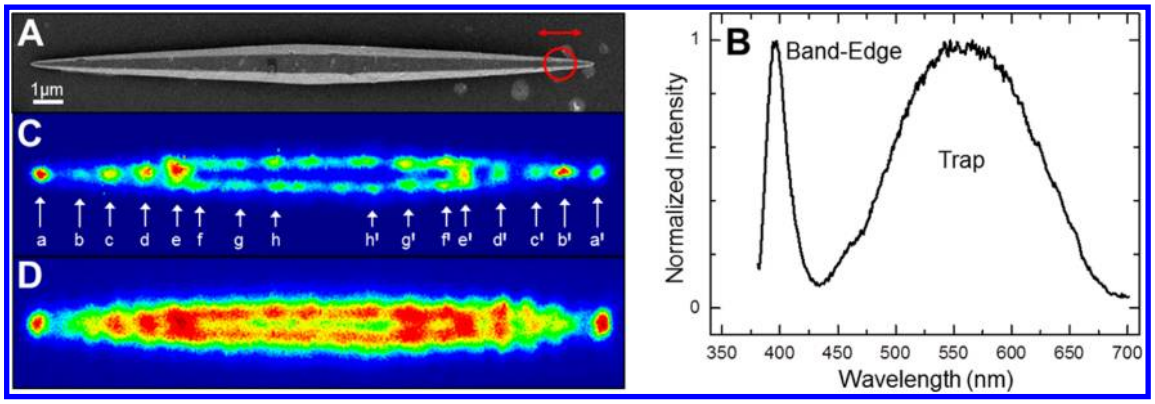

Figure 2. (A) SEM image and (B) emission spectrum of a tapered zinc oxide nanorod. The red circle and double-headed arrow indicate the location at which the spectrum was acquired and the direction of the excitation polarization vector, respectively. (C, D) Photoluminescence images taken at 390 and 550 nm, respectively, show a modulated emission pattern along the structure. The lower case letters in (C) indicate the resonance spots discussed in the text.

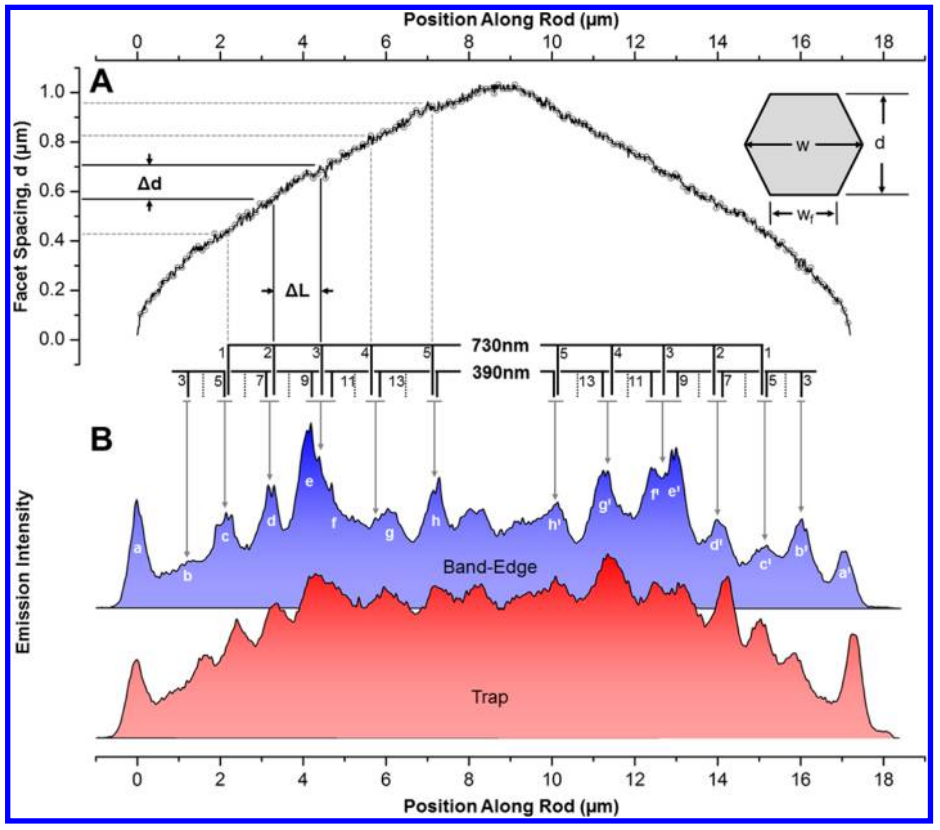

Figure 3. (A) Facet spacing determined from the SEM image in Figure 2A plotted as a function of position along the rod. (B) Intensity profiles obtained by integrating a column of pixels at each longitudinal position along the images for both the band-edge and trap emission images (Figure 2C and D). The calculated whispering gallery mode locations for 730 and 390 nm light are indicted by the two brackets positioned between (A) and (B). The lower-case letters in the band-edge profile correspond to the resonance spots indicated in Figure 2B.

the hexagonal cross-section through total internal reflection off each facet. Both are characterized by resonance conditions that depend upon the resonator size and wavelength, that is,

$$d_{\mathrm{FP}}^{m} = \frac{\lambda}{2n}m \tag{1a}$$

$$d_{\mathrm{WG}}^{m} = \frac{\lambda}{3n}\left(m + \frac{6}{\pi}\tan^{-1}(\beta\sqrt{3n^2 - 4})\right) \tag{1b}$$

where d_{FP}^{m} and d_{WG}^{m} are the facet separations for the mth mode in the FP and WG resonances, respectively, λ is the wavelength, and n is the index of refraction. The value of β is based on the polarization of the excitation source, being $\beta = n$ for TM ($E\|c$) and $\beta = n^{-1}$ for TE ($E\perp c$).

The distance between resonance spots in the emission images, ΔL, depends upon the taper angle of the structure, with smaller cone angles giving rise to larger separations, that is,

$$\Delta L = \frac{\Delta d}{\alpha} \tag{2}$$

where Δd is the mode spacing, that is, $(d^{m+1} - d^{m})$, and α is the change in facet spacing per unit length along the structure.

dx.doi.org/10.1021/jp4011907 | J. Phys. Chem. C 2013, 117, 10653−10660

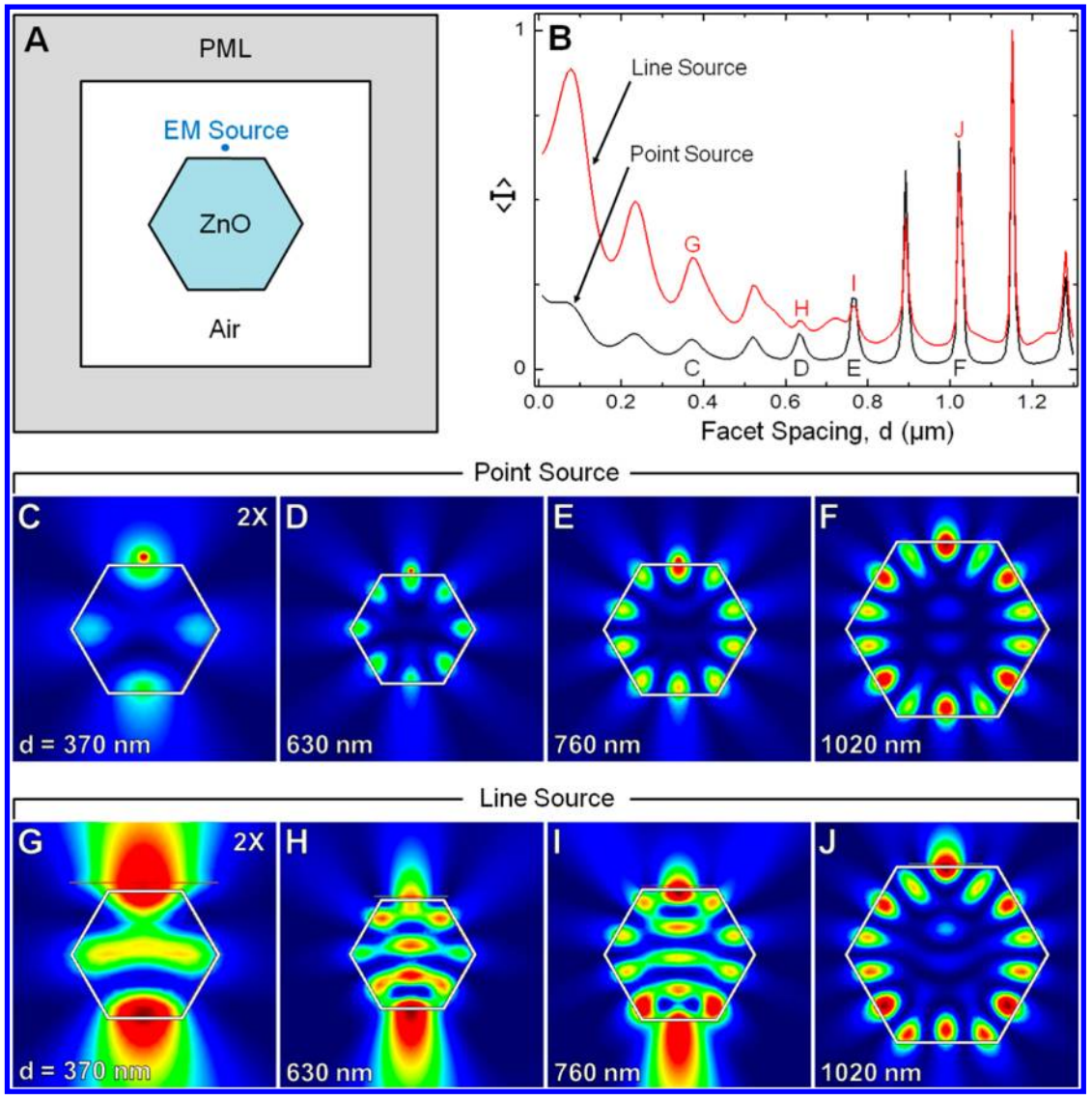

Figure 4. (A) Diagram of the simulation environment depicting the point source configuration. The line source (not shown) is placed in the same location and is 440 nm wide. (B) Plot of the average intensity ($\langle I \rangle = \int |E|^2 dA/A_{hex}$) as a function of the facet spacing (d) for both the point source (black) and line source (red). (C–J) Spatial intensity maps ($|E|^2$) for resonators with facet spacing d = 370, 630, 760, and 1020 nm for the point source (C–F) and line source (G–J). Blue corresponds to zero intensity, and red is max intensity.

The value of α varies from one rod to the next, but its value for a particular rod can be estimated from the SEM image. Moreover, for this rod, the overall width (w) is twice the facet width (w_f) over most of the length, indicating that the cross section is nearly a perfect hexagon (Figure 3, inset). The facet spacing (d) is determined from w using $d = (\sqrt{3}/2)w$ and is depicted as a function of position along the rod in Figure 3A. The α-values extracted from the slopes on the right and left side are 101 and 103 nm/μm, respectively, indicating that the rod is nearly symmetric with a consistent taper throughout the much of the structure.

The predicted spacing between resonance spots along the rod are $\Delta L_{FP} = \lambda/2n\alpha$ and $\Delta L_{WG} = \lambda/3n\alpha$ for the two different optical mode types. Using an average α-value of 102 nm/μm and n = 2 for the index of refraction of ZnO at 730 nm[26] leads to predicted separations of ΔL_{FP} = 1.8 μm and ΔL_{WG} = 1.2 μm.

Intensity profiles along the long axis for the band-edge and trap emission images (Figure 3B) show the resonances to be nearly equally spaced with an average ΔL of 1.0–1.2 μm. This spacing is qualitatively consistent with the WG mode description and significantly smaller than the spacing predicted by the FP resonance condition. The locations of the WG resonances for the first five modes (λ = 730 nm), indicated by the bracket placed above the emission profile, coincide with the locations of the emission maxima.

If the modulated emission intensities were due solely to cavity resonance involving the excitation light, then the patterns observed in the band-edge and trap emission images should be the same. This is not the case. While the modulated pattern is present in both, the band-edge image exhibits a higher contrast compared to the trap, suggesting that the intensity pattern is influenced, to some degree, by the emission. We estimate that in this structure the resonance spacing, ΔL, for 390 nm light (n = 2.33)[26] would be 0.54 μm. This is approximately half the spacing for the 730 nm resonances, leading to a possible double-resonance scenario in which the 730 nm modes coincide with every other 390 nm mode (see 390 nm bracket, Figure 3). Amplified spontaneous emission, and even lasing, of the band-

dx.doi.org/10.1021/jp4011907 | J. Phys. Chem. C 2013, 117, 10653–10660

edge photoluminescence has been observed in ZnO nanostructures. While we do not observe evidence of actual lasing, previous work in our lab[20] showed that the band-edge emission has a greater than quadratic power dependence on pulse intensity. This is particularly true when the rod is excited at one of the resonance spots,[20] suggesting that the emission is likely reinforced by the cavity modes as the 390 nm emitted light is reflected off the facets and returns to the excitation region. The trap emission, on the other hand, shows simple quadratic dependence. The larger scaling factor for the band-edge emission effectively results in a higher spatial resolution, accounting for the greater contrast difference between the band-edge and trap emission images.

These WG mode descriptions qualitatively account for many of the features observed in the emission images, but they do not explain the existence of the spots at the ends of the rod (denoted a and a′). At this point, d = 160 nm. This is far below the 450 nm predicted by the WG resonance condition (eq 1b) for the m = 1 resonance with λ = 730 nm, and also smaller than the 210 nm spacing obtained with λ = 390 nm. Interestingly, it is close to the spacing calculated using the FP resonance condition (eq 1a) for the m = 1 mode at 730 nm, underscoring the idea that neither picture adequately describes the resonance properties of these structures.

Finite Difference Frequency Domain (FDFD) Simulations. We have used finite element methods to map the optical intensity distribution created in the rod upon photoexcitation. We treat the 3D tapered rod as a stack of hexagonal resonators of different diameters, enabling the overall structure to be modeled using a series of two-dimensional calculations. The 2D model of each individual resonator (see Figure 4A, for example) consists of a square box (air) with a hexagonal slab (ZnO) placed at the center. The box is surrounded by a perfectly matched layer (PML) that eliminates electromagnetic reflections at simulation boundaries. The mesh spacing used in the simulations, defined as the size of the largest cell, was 30 nm, which is approximately 10 times smaller than the wavelength inside the ZnO material. Simulations performed with a smaller mesh size (15 nm) yielded identical results, confirming the appropriateness of this choice. FDFD methods, which were implemented using the COMSOL Multiphysics software package (version 4.3), solve for the electromagnetic field in response to a single-frequency source, resulting in a steady-state map of the optical intensity distribution inside the resonator. We have examined four different sources: (i) point-source, (ii) line source, (iii) focused Gaussian beam, and (iv) plane-wave. The first two provide a crude approximation of the localized laser excitation; the third is realistic representation of the focused laser beam used in the experiment, while the last provides a comparison with far-field excitation configurations. In each case, the source is polarized with the electric field perpendicular to the simulation plane and the output of the simulation is the EM field inside the simulation area.

(i). Point Source. The simplest localized excitation scheme is an oscillating (ν = 411 THz, λ = 730 nm) current density point source positioned 25 nm above the center of the topmost facet. Figure 4B shows the average optical intensity inside the resonator (i.e., $\langle I\rangle = \int |E|^2 dA/A_{hex}$) as a function of its size. The plot shows a series of sharp resonances for the larger cavity sizes that become increasingly broad for the smaller diameters. The intensity distribution inside the hexagonal cavity is depicted for four of the resonances in Figure 4C–F. The largest resonators show the characteristic WG mode pattern in which the optical field is located near the periphery of the structure. The width of the resonances reflects the quality of the cavity. For the larger sizes, total internal reflection at each facet minimizes loss, resulting in multiple round trips and narrow resonances. The broadening of the resonances as the cavity size decreases suggests an increased loss per round trip. This most likely occurs at the vertices, which become a dominant feature at the smaller sizes.

The spacing between modes is not constant across this size range. The Δd spacing between the sharp peaks at larger cavity size is 130 nm, similar to that predicted by the WG mode resonance condition (eq 1b). Interestingly, for the broader resonances, at smaller cavity sizes, Δd is about 160 nm, which matches the FP spacing (eq 1a) Although the presence of standing-wave character is not obvious from the mode patterns, the EM sources described below suggest that the modes best described as hybrid resonance with both WG and FP character.

(ii). Line Source. While the point source is qualitatively appealing, it is not a good representation of the experimental configuration, where the spatial extent of excitation is several hundred nanometers. A similar calculation in which the point source is replaced by a line 400 nm long and centered at 25 nm above the top facet addresses this shortcoming. The results from this simulation, which are shown alongside those for the point source in Figure 4, highlight the role that the source plays in shaping the field patterns.

A key factor appears to be the size of the source in relation to that of the resonator. The resonances for the larger cavity sizes are unaffected by the increase in the size of the source. They have similar magnitude and width, and are located at the same diameters (Figure 4B). Furthermore, the field distributions (Figure 4J) are nearly identical to those obtained from the point source, with a small, but notable difference being a slight increase in the intensity present in the center of the resonator. While the results for the larger diameter are unaffected by the change in source, there are significant differences at smaller sizes (d < 600 nm). First, the broad resonances at smaller diameters have drastically higher average intensities in the line source model than the point source (Figure 4B). Moreover, the field distributions are also affected. Whereas the point source produces a mode pattern in the 370 nm resonator that is largely WG in nature, the patterns obtained with the line source takes on more standing-wave character (Figure 4G). As the cavity size increases (630 and 760 nm), the modes are neither completely WG- nor FP-like in character (Figure 4H–I), but rather a combination of the two. The simulations point to the presence of two modes progressions, where at large cavity sizes the resonances are dominated by WG modes, and at small cavity sizes they are dominated by FP character. Hybrid resonances that contain elements of both are observed where the two progressions overlap, which appears to occur when the source and top facet are of similar sizes. These results underscore the need for adequately modeling the EM source in simulating the emission patterns of these structures.

(iii). Gaussian Source. An optical source that mimics the focused Gaussian beam used in the experiment is implemented by specifying the EM field along the boundary, that is,

$$E(x) = E_0 \frac{\omega_0}{\omega(y_B)} \exp\left(\frac{-x^2}{\omega^2(y_B)} - ik\frac{x^2}{2R(y_B)} + i\zeta(y_B)\right) \quad (3)$$

where y_B is the distance from beam waist to the boundary, x is the coordinate along the boundary, and k is the wave vector for the

dx.doi.org/10.1021/jp4011907 | J. Phys. Chem. C 2013, 117, 10653–10660

propagating electric field (Figure 5A). The radius of the beam waist at the focus, ω_0, is defined at the $1/e$ width of the electric

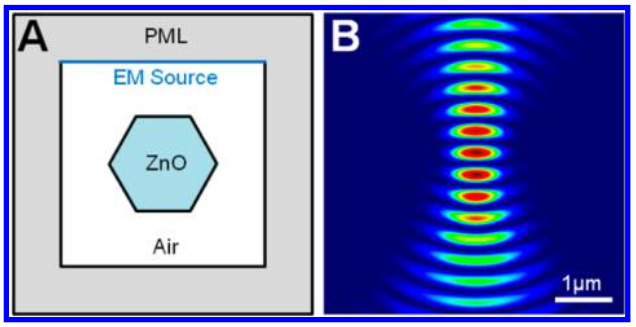

Figure 5. (A) Diagram of the focused Gaussian simulation environment. The EM source is functionalized according to eq 3 with the x and y dimensions corresponding to the horizontal and vertical axes and the origin located at the center of the simulation box. (B) Spatial map of the optical field $(Re(|E|))^2$ produced by the Gaussian source in the absence of the resonator.

field. The functions $\omega(y_B) = \omega_0(1 + (y_B/y_R))^{1/2}$, $R(y_B) = y_B[1 + (y_R/y_B)^2]$, and $\zeta(y_B) = \arctan(y_B/y_R)$ are the beam width, radius of curvature, and Gouy phase at the boundary, respectively, and $y_R = \pi\omega_0^2/\lambda$. With this boundary condition, the EM field focuses to a minimum spot size at the center of the simulation box ($y = 0$). An intensity map of the optical field, $(Re(|E|))^2$, produced by this Gaussian source, in the absence of the hexagonal resonator, is shown in Figure 5B. With $\omega_0 = 460$ nm, the lateral width of the two-photon volume created by the source, obtained by examining $I^2 = (|E|^2)^2$, is around 420 nm, which is comparable to the lateral resolution of two-photon excitation in our microscope.

The top of Figure 6 shows a simulated two-photon emission image obtained using this focused Gaussian source. The image was reconstructed using a procedure analogous to the experimental image collection. First, the cross-sectional diameter is determined at a particular position along the rod from the SEM image. For a given resonator size, a series of simulations are performed at different displacements between the central axis of the EM source and the midpoint of the resonator. For each configuration, the squared-intensity, that is, $(|E|^2)^2$, is integrated inside the resonator to represent the total two-photon excitation; this series of integrated intensities is then represented by a column of pixels in the simulated image. The process is repeated for a series of resonator sizes to construct the two-dimensional image.

The simulated image is a reasonable mimic of the two-photon emission image, reproducing many of its qualitative features, including the appearance of off-centered spots at larger diameters that become single, centered spots near the ends of the rod. The mode patterns that correspond to resonance spots reveal two distinct progressions. When excited at the center, the smaller resonators near the tips of the rod show hybrid patterns with more FP than WG mode character (Figure 6A–D), while significant WG character is observed in the mode pattern when excited off-center (Figure 6E–H), especially at the larger diameters. The simulated image also shows the existence of modes at facet spacing values below the lowest predicted WG mode resonance for either 390 or 730 nm light (for 390 nm, $d^1_{WGM} = 210$ nm) and predicts the intense spot at the tip of the rod. Slices of the image taken down the center (red) and at 500 nm off-center (blue) are plotted as a function of position at the

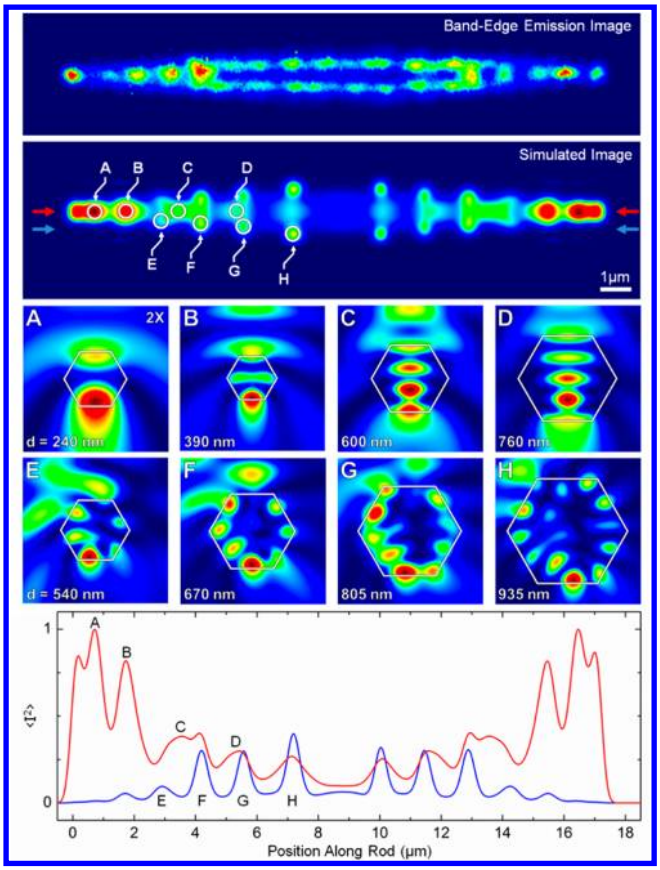

Figure 6. (Top) Simulated emission image constructed from a series of calculations on resonators with sizes corresponding to width measurements taken from the SEM image (horizontal dimension). A series of calculations are performed for each resonator size in which the center of the Gaussian source is offset relative to the center of the resonator in the horizontal dimension. For each simulation, the average squared intensity ($\langle I^2\rangle = \int |E|^4 dA/A_{hex}$) inside the resonator is calculated and its value is displayed as pixel in the image, with blue colors corresponding to zero intensity; red is maximum intensity. (A–H) Spatial intensity maps ($|E|^2$) of the corresponding encircled modes from the image. (Bottom) Plot of average squared intensity per unit area for a slice through the center (red) and 500 nm from the center (blue).

bottom of Figure 6. The intensity of the centered modes decreases with increasing the diameter, while the intensity of the off-centered modes follows the opposite trend.

(iv). Plane-Wave Source. The dependence of the field patterns on source geometry raises the question: Is the spatial variation observed with the focused source also present when the structure is excited by a monochromatic plane-wave? We addressed this question by replacing the focused Gaussian beam with a plane wave source (Figure 7). Although the details differ, many of the features observed with the Gaussian source are preserved with plane wave excitation (Figure 7A). Both show a series of broad resonances with considerable FP character at small diameters (Figure 7B), which become increasingly WG-mode-like at larger diameters (Figure 7C–E). This suggests that the spatial heterogeneity observed within these single structures would also be present when illuminating the entire structure, as is done for ensemble measurements.

Implications. Transient absorption microscopy experiments from our group shows that electron–hole recombination in the tips of these structures occurs primarily through band-edge states, whereas in the interior locations it is dominated by

dx.doi.org/10.1021/jp4011907 | J. Phys. Chem. C 2013, 117, 10653–10660

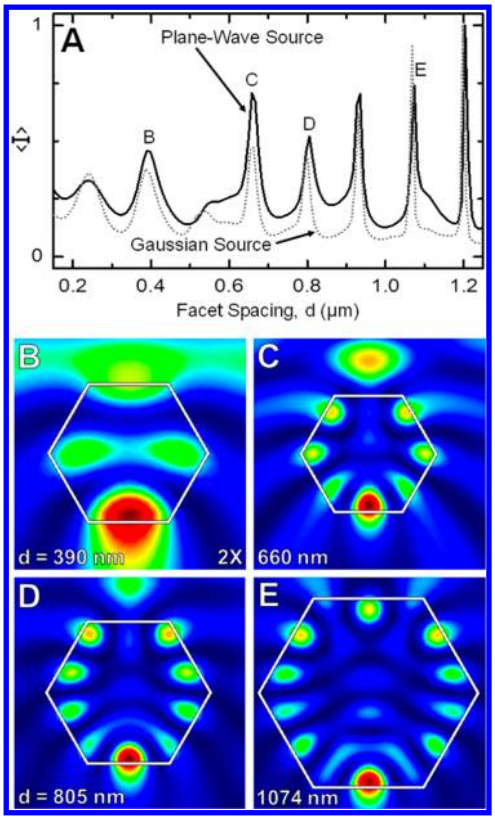

Figure 7. (A) Plot of the average intensity ($\langle I \rangle = \int |E|^2 dA/A_{hex}$) as a function of facet spacing for the plane wave source (black) and the Gaussian source (gray, dotted), calculated by integrating each column of the simulated image in Figure 6. (B–E) Spatial intensity maps ($|E|^2$) of several of the simulated resonant modes for the plane-wave excitation source.

trapping.[21,22] The qualitative difference between the WG and FP type modes offer a plausible explanation for this spatial dependence. In the larger diameter sections, the cavity resonances are almost completely WG in nature, with the largest intensity being located near the surface of the rod. When the optical intensity is concentrated in the periphery of the rod, photoexcited carriers will be produced in the surface depletion zone. The internal field present in this region (i.e., band bending) will separate the electrons and holes, resulting in a greater degree of carrier trapping and longer recombination times. The FP modes near the tips of the rods have the optical field localized primarily in the core of the structure. The standing wave patterns produced in these regions may result in the preferential production of photoexcited carriers in the core of the structure. Because of the low carrier mobility, electrons and holes created in this zone would remain there and experience a lattice environment similar to that of the bulk, accounting for the greater degree of recombination observed at the band edge.

CONCLUSIONS

Two-photon emission microscopy is used to investigate the photoluminescence properties of individual ZnO rods. The rods are 10–20 μm in length with a tapered cross section that varies from 1 to 2 μm at the midpoint to several hundred nanometers at the ends. This structure, with its tapered ends and hexagonal cross section, results in a complex series of optical resonator modes. Two types of modes typically ascribed to hexagonal resonators are Fabry-Pérot (FP) modes and whispering gallery (WG) modes. Finite-difference frequency domain methods suggest that resonator modes of these structures are better described as hybrid modes that have both standing wave (Fabry-Pérot) and whispering gallery mode character, whose relative contributions vary along the rod axis. In particular, at the tips of the rod the modes have significant standing wave character, whereas in the larger cross sections, near the rod midpoint, the modes are dominated by whispering gallery mode features.

AUTHOR INFORMATION

Corresponding Author

*Phone: 919-962-1619. E-mail: John_Papanikolas@unc.edu.

Present Address

[†]J.K.P.: Chemical Sciences Division, U.S. Army Research Office, PO Box 12211, Research Triangle Park, NC 27709.

Notes

The authors declare no competing financial interest.

ACKNOWLEDGMENTS

Funding for this project came from grants from the National Science Foundation, initially CHE-0809045 and later CHE-1213379. The COMSOL simulation software was purchased under a grant from the U.S. Army Research Laboratory and the U.S. Army Research Office under Contract Number W911NF-04-D-0004. The project also made use of instrumentation purchased by the UNC-EFRC Center for Solar Fuels, an Energy Frontier Research Center funded by the U.S. Department of Energy, Office of Science, Office of Basic Energy Sciences under Award Number DE-SC0001011.

REFERENCES

(1) Ozgur, U.; Alivov, Y. I.; Liu, C.; Teke, A.; Reshchikov, M. A.; Dogan, S.; Avrutin, V.; Cho, S. J.; Morkoc, H. A Comprehensive Review of ZnO Materials and Devices. *J. Appl. Phys.* **2005**, *98*, 041301–041404.

(2) Djurisic, A. B.; Leung, Y. H. Optical properties of ZnO nanostructures. *Small* **2006**, *2*, 944–961.

(3) Wang, Z. L. Zinc Oxide Nanostructures: Growth, Properties and Applications. *J. Phys.: Condens. Matter* **2004**, *16*, R829–R858.

(4) van Vugt, L. K.; Ruhle, S.; Ravindran, P.; Gerritsen, H. C.; Kuipers, L.; Vanmaekelbergh, D. Exciton Polaritons Confined in a ZnO Nanowire Cavity. *Phys. Rev. Lett.* **2006**, *97*, 147401–147405.

(5) Ruhle, S.; van Vugt, L. K.; Li, H. Y.; Keizer, N. A.; Kuipers, L.; Vanmaekelbergh, D. Nature of Sub-band Gap Luminescent Eigenmodes in a ZnO Nanowire. *Nano Lett.* **2008**, *8*, 119–123.

(6) Zimmler, M. A.; Bao, J.; Capasso, F.; Muller, S.; Ronning, C. Laser Action in Nanowires: Observation of the Transition from Amplified Spontaneous Emission to Laser Oscillation. *Appl. Phys. Lett.* **2008**, *93*, 051101–051104.

(7) Yang, Y. H.; Zhang, Y.; Wang, N. W.; Wang, C. X.; Li, B. J.; Yang, G. W. ZnO Nanocone: Application in Fabrication of the Smallest Whispering Gallery Optical Resonator. *Nanoscale* **2011**, *3*, 592–597.

(8) Nobis, T.; Kaidashev, E. M.; Rahm, A.; Lorenz, M.; Grundmann, M. Whispering Gallery Modes in Nanosized Dielectric Resonators with Hexagonal Cross Section. *Phys. Rev. Lett.* **2004**, *93*, 103903–103907.

(9) Nobis, T.; Grundmann, M. Low-Order Optical Whispering-Gallery Modes in Hexagonal Nanocavities. *Phys. Rev. A* **2005**, *72*, 063806–063817.

(10) Sun, L. X.; Chen, Z. H.; Ren, Q. J.; Yu, K.; Bai, L. H.; Zhou, W. H.; Xiong, H.; Zhu, Z. Q.; Shen, X. C. Direct Observation of Whispering Gallery Mode Polaritons and their Dispersion in a ZnO Tapered Microcavity. *Phys. Rev. Lett.* **2008**, *100*, 156403–156407.

(11) Liu, J. Z.; Lee, S.; Ahn, Y. H.; Park, J. Y.; Koh, K. H.; Park, K. H. Identification of Dispersion-dependent Hexagonal Cavity Modes of an Individual ZnO Nanonail. *Appl. Phys. Lett.* **2008**, *92*, 263102–263105.

(12) Czekalla, C.; Nobis, T.; Rahm, A.; Cao, B. Q.; Zuniga-Perez, J.; Sturm, C.; Schmidt-Grund, R.; Lorenz, M.; Grundmann, M. Whispering Gallery Modes in Zinc Oxide Micro- and Nanowires. *Phys. Status Solidi B* **2010**, *247*, 1282−1293.
(13) Zhang, Y.; Zhou, H. J.; Liu, S. W.; Tian, Z. R.; Xiao, M. Second-Harmonic Whispering-Gallery Modes in ZnO Nanotetrapod. *Nano Lett.* **2009**, *9*, 2109−2112.
(14) Czekalla, C.; Sturm, C.; Schmidt-Grund, R.; Cao, B. Q.; Lorenz, M.; Grundmann, M. Whispering Gallery Mode Lasing in Zinc Oxide Microwires. *Appl. Phys. Lett.* **2008**, *92*, 241102.
(15) Dai, J.; Xu, C. X.; Wu, P.; Guo, J. Y.; Li, Z. H.; Shi, Z. L. Exciton and Electron-hole Plasma Lasing in ZnO Dodecagonal Whispering-gallery-mode Microcavities at Room Temperature. *Appl. Phys. Lett.* **2010**, *97*, 011101.
(16) Yang, Y. H.; Dong, J. W.; Wang, N. W.; Yang, G. W. Whispering Gallery Mode Enhanced Luminescence from an Individual ZnO Micro- and Nanoscaled Optical Resonator. *J. Appl. Phys.* **2011**, *109*, 093511−093517.
(17) Gargas, D. J.; Moore, M. C.; Ni, A.; Chang, S. W.; Zhang, Z. Y.; Chuang, S. L.; Yang, P. D. Whispering Gallery Mode Lasing from Zinc Oxide Hexagonal Nanodisks. *ACS Nano* **2010**, *4*, 3270−3276.
(18) Mehl, B. P.; House, R. L.; Uppal, A.; Reams, A. J.; Zhang, C.; Kirschbrown, J. R.; Papanikolas, J. M. Direct Imaging of Optical Cavity Modes in ZnO Rods Using Second Harmonic Generation Microscopy. *J. Phys. Chem. A* **2010**, *114*, 1241−1246.
(19) House, R. L.; Mehl, B. P.; Kirschbrown, J. R.; Barnes, S. C.; Papanikolas, J. M. Characterizing the Ultrafast Charge Carrier Trapping Dynamics in Single ZnO Rods Using Two-Photon Emission Microscopy. *J. Phys. Chem. C* **2011**, *115*, 10806−10816.
(20) House, R. L.; Kirschbrown, J. R.; Mehl, B. P.; Gabriel, M. M.; Puccio, J. A.; Parker, J. K.; Papanikolas, J. M. Characterizing Electron-Hole Plasma Dynamics at Different Points in Individual ZnO Rods. *J. Phys. Chem. C* **2011**, *115*, 21436−21442.
(21) Mehl, B. P.; Kirschbrown, J. R.; House, R. L.; Papanikolas, J. M. The End Is Different than The Middle: Spatially Dependent Dynamics in ZnO Rods Observed by Femtosecond Pump-Probe Microscopy. *J. Phys. Chem. Lett.* **2011**, *2*, 1777−1781.
(22) Mehl, B. P.; Kirschbrown, J. R.; Gabriel, M. M.; House, R. L.; Papanikolas, J. M. Pump-Probe Microscopy: Spatially Resolved Carrier Dynamics in ZnO Rods and the Influence of Optical Cavity Resonator Modes. *J. Phys. Chem. B* **2013**, *117*, 4390−4398.
(23) Cheng, B.; Samulski, E. T. Hydrothermal Synthesis of One-Dimensional ZnO Nanostructures with Different Aspect Ratios. *Chem. Commun.* **2004**, 986−987.
(24) Li, F.; Li, Z.; Jin, F. J. Structural and Luminescent Properties of ZnO Nanorods Prepared from Aqueous Solution. *Mater. Lett.* **2007**, *61*, 1876−1880.
(25) Zipfel, W. R.; Williams, R. M.; Webb, W. W. Nonlinear Magic: Multiphoton Microscopy in the Biosciences. *Nat. Biotechnol.* **2003**, *21*, 1368−1376.
(26) Postava, K.; Sueki, H.; Aoyama, M.; Yamaguchi, T.; Ino, C.; Igasaki, Y.; Horie, M. Spectroscopic Ellipsometry of Epitaxial ZnO Layer on Sapphire Substrate. *J. Appl. Phys.* **2000**, *87*, 7820−7824.

THE JOURNAL OF PHYSICAL CHEMISTRY C

ARTICLE

pubs.acs.org/JPCC

Characterizing the Ultrafast Charge Carrier Trapping Dynamics in Single ZnO Rods Using Two-Photon Emission Microscopy

Ralph L. House, Brian P. Mehl, Justin R. Kirschbrown, Scott C. Barnes, and John M. Papanikolas*

Department of Chemistry, Caudill Laboratories, University of North Carolina at Chapel Hill, Chapel Hill, North Carolina 27599, United States

ABSTRACT: Zinc oxide has emerged as an attractive candidate for a variety of optoelectronic and photonic applications, due in part to a large second-order nonlinear susceptibility, its wide band gap, and large exciton binding energy. We have used time-resolved nonlinear two-photon emission microscopy to characterize the excited-state dynamics of individual ZnO rods. Photoluminescence images reveal a rich structure in the spatial distribution of both the band-edge and trap emission, and spectra recorded following excitation at a specific point in the structure show the characteristic band-edge and defect emission. Time-resolved emission spectra reveal a dynamic red shift of the trap emission band in the as-grown structures. Our results suggest that the trap emission is composed of at least two overlapping emission bands. The higher-energy band is assigned to e−h recombination between a conduction band electron and photogenerated hole bound to an acceptor defect lying within the band gap. The lower-energy band is attributed to a donor−acceptor pair (DAP) transition in which an electron localized on a donor defect recombines with a nearby hole-bound acceptor. The DAP transition energy and recombination rate depend upon the spatial proximity of the two traps, with higher-energy transitions corresponding to closely spaced pairs and occurring more rapidly, resulting in the dynamic red shift. Reduction in the trap density following annealing suppresses the DAP emission and its signature time-dependent red shift. The blue shift of the static photoluminescence spectrum is attributed to the donor defects being preferentially annealed out of the structure, resulting in a larger contribution of the higher-energy band.

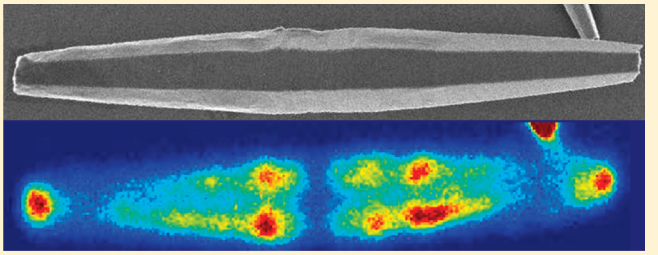

INTRODUCTION

The ability to manipulate the shape of ZnO structures is enormous, and through a variety of facile synthetic methods many different forms, including nanorods with differing end morphologies, tetrapods, and nanohelices have been created.[1−3] The sizes of these structures, which can vary from tens of nanometers to many micrometers, are amenable to ultra-small-scale electronic devices, and the prismatic shapes of the crystalline structures give rise to optical cavities that can be exploited in optoelectronic and photonic applications.[4−13] Since finite-sized structures can introduce new dynamical phenomena not found in bulk materials, understanding the relationship between structure and function is critical to device design. The electronic and photophysical behavior, for example, are strongly influenced by the surfaces and intrinsic defects, which trap mobile carriers and result in band bending and internal electric fields.[14−16] As a consequence, the spectroscopy often depends upon the size and shape of the particle,[2] and significant variation from one object to the next is frequently observed.[17,18] In addition, the physical confinement of carriers in the sharp features of high-aspect structures or spatial variation in defect density across an object can influence carrier relaxation and result in photophysical behavior that differs from one point to another within an individual object.

We have characterized the trap recombination dynamics in needle-like ZnO rods on ultrafast time scales using time-resolved two-photon emission microscopy. Our experiments differ from previous work on ZnO in that they excite a localized region (350 nm diameter) of an individual structure and probe the carrier dynamics between different points in the structure. Photoexcitation in the UV (or simultaneous two-photon excitation in the near-infrared) promotes an electron from the valence band to the conduction band to create free carriers that can either relax into excitonic states that lie just below the conduction band edge or into trap states associated with defects in the crystal lattice or the structure's surface (Figure 1). Exciton recombination gives rise to UV-blue emission that is centered at ∼390 nm, while defect states localized within the band gap offer additional pathways for electron−hole recombination and give rise to a broad visible emission band extending from 500 to 650 nm.

Although the atomic structure of the lattice is (nominally) uniform, we have observed a clear variation in the optical properties of different structural regions. Second-harmonic imaging of these structures shows that the frequency-doubling efficiency is strongly influenced by optical resonator modes.[19] Photoluminescence maps also show significant variation in the band-edge and trap emission across the structure that ultimately

Received: December 13, 2010
Revised: April 19, 2011

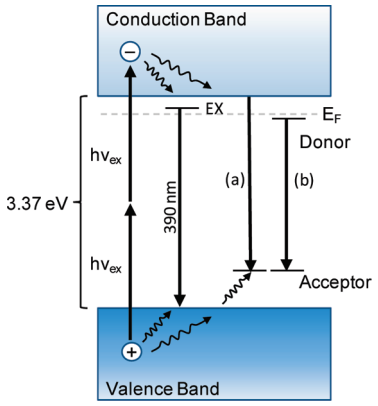

Figure 1. Illustration of the ZnO band diagram. Two-photon excitation produces free carriers that can either relax into excitonic states, which give rise to the band-edge emission centered around 390 nm, or fall into trap states localized within the band gap giving rise to lower-energy emission centered around 550 nm. Trap recombination can occur through variety of mechanisms including (a) recombination between an electron in the conduction band and a hole localized on an acceptor trap state and (b) recombination between an electron localized on a shallow donor trap state and an electron bound to an acceptor trap state.

could be the result of cavity resonances arising from the object's shape. In addition, spatial variation of the photophysics can stem from an inhomogeneous defect distribution. There is a distinct reduction in the emission at the rod midpoint, for example, which is attributed to an increase in the defect density arising from a grain boundary. Luminescence lifetimes measured at different locations within the structure seem to support this assignment.

This paper focuses particularly on the role that native defects (such as vacancies and interstitials) play in facilitating electron−hole recombination. The identity and photophysics of ZnO defects have been the subject of a vast number of research efforts, and a number of notable reviews[2,3,20−22] exist on the subject. Nevertheless, the origin of defect emission has remained a subject of much controversy. Much of the debate has centered on identifying the chemical nature of the defects' sites, each of which can be present in one of several ionization states. Although there is a wide array of potential defects, they can generally be categorized as being able to trap either electrons (i.e., donor states) or holes (i.e., acceptor states). Since ZnO is an intrinsic n-type material,[20] all but the donor sites that lie very close to the conduction band edge are generally filled and natively exist in their most negatively charged state, even in the dark.

Following photoexcitation, there are several different transitions that can give rise to trap emission including donor recombination with a hole in the valence band ($D \rightarrow h^+$), acceptor recombination with an electron in the conduction band ($A \rightarrow e^-$), and recombination between an electron localized on a donor with a hole localized on an acceptor. The latter mechanism is known as donor−acceptor pair (DAP) recombination[23] and occurs between donor and acceptor defects that are in close proximity within the crystal lattice. The experiments discussed here indicate that the broad trap emission spectrum is composed of two different bands with the lower-energy transition (λ_{max} = 550 nm) corresponding to DAP emission and the higher-energy band (λ_{max} = 525 nm) arising from acceptor recombination with free carriers in the conduction band.

By performing measurements on individual structures, we can focus our attention on objects with known morphology. We have developed protocols that enable a series of experiments to be performed on the same object. These methods allow us to correlate the emission images with detailed structural information from scanning electron microscopy (SEM) images, as well as compare spectroscopic observations at the *same* point in the *same* structure before and after postprocessing procedures such as annealing. We show that different regions of the same structure can exhibit different trapping behaviors and, thus, provide a novel perspective on the role that native defects play in the photophysical properties of ZnO nanostructures.

EXPERIMENTAL SECTION

Materials. The ZnO rods were grown using a hydrothermal method adapted from work conducted by Cheng et al.[24] and Li et al.[25] The procedure, which involves heating a 0.05 M reaction solution of $Zn(NO_3)_2$ and hexamethylenetetramine ($(CH_2)_6N_4$) in a closed bomb, typically yields needle-shaped rods ranging from 5 to 30 μm in length and 0.5 to 2 μm in width. The size is controlled by varying reaction temperature, time, and/or concentration. After completion of the reaction, structures are harvested and sonicated in ethanol (200 proof) to break up aggregates and form a suspension. Microscopy samples are prepared by drop-casting ~250 μL of the suspension onto a microscope slide with an etched reference grid. The reference grid facilitated the relocating of the rod for subsequent experiments in the optical microscope or structural characterization via SEM imaging. Once the ethanol evaporates, the slide is placed on the scanning stage with the ZnO rods facing the objective lens. Imaging is performed without a coverslip under ambient conditions.

Two-Photon Microscopy. The microscope consists of a mode-locked Ti:Sapphire laser (Spectra-Physics Tsunami) pumped by a 5 W frequency-doubled continuous-wave diode laser (Spectra-Physics Millenia). The system produces pulses with an 80 fs width at a repetition rate of 76 MHz and a tuning range between 720 and 850 nm with a maximum power output of approximately 1 W. The output is sent through a Faraday isolator and then directed through a prism-pair compressor operated in a double-pass configuration (Figure 2). The pulse energy entering the microscope is reduced to between 0 and 1 nJ/pulse using a variable attenuator constructed from a half-wave plate and polarizing cube.

The microscope employs an inverted design with its objective located below the sample plane. The femtosecond laser beam is expanded by a lens pair, reflected off a dichroic mirror (R, 680−1000 nm; T, 360−650 nm), and then directed into the objective (Olympus MSPlan 50×, NA 0.8), overfilling its input aperture. The sample is raster-scanned across the focal point of the objective using a piezoelectric $x-y$ translation stage (Queensgate NPS3330 controller/stage system) with a step-size and reproducibility that are both less than 20 nm. Two-photon emission emanating from the sample is collected by the objective. Light transmitted through the dichroic beam splitter is focused onto the entrance slit of a monochromator and detected by a photomultiplier tube (PMT) operated in a photon-counting mode. Under typical experimental conditions, the sample emits or generates a signal photon every 500−1000 laser pulses. The PMT output is sent to a discriminator and a counter located on a data acquisition card (model PCI 6602, National Instruments). In addition to the photon counting detection used for imaging, the emitted light can be directed into a time-correlated single-photon counting instrument to obtain time-resolved emission data with an approximately 100 ps instrument response or a

dx.doi.org/10.1021/jp1118426 |*J. Phys. Chem. C* XXXX, XXX, 000–000

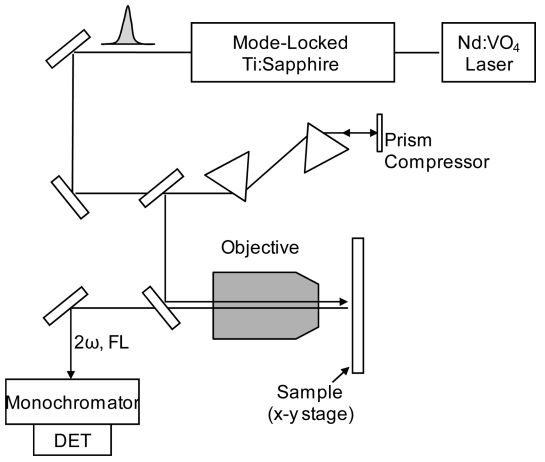

Figure 2. Schematic overview of our nonlinear microscope system. Excitation light is generated by a mode-locked Ti:Sapphire laser that is pumped by a 5 W frequency-doubled, continuous-wave diode laser (532 nm). The system generates pulses with an 80 fs width at a 76 MHz repetition rate and a tuning range between 720 and 850 nm with a maximum power output of ~1 W. A prism compressor, operated in a double-pass configuration, is used to correct for pulse dispersion. For time-resolved experiments the pulse repetition rate is reduced by a factor of 10 using an acousto-optic modulator (not shown). For imaging, the detector is a photomultiplier tube operated in a single-photon counting mode. Detection for time-resolved experiments is either time-correlated single-photon counting instrumentation or a streak camera. The power entering the microscope is controlled with a variable attenuator that consists of a wave plate and polarization beam splitter cube. Light is expanded 2× to overfill the input aperture of the objective. The sample is raster-scanned across the objective focal point, and the resulting fluorescence/SHG is collected back through the objective, focused into the slit of a monochromator, and detected by a photomultiplier tube.

streak camera with approximately 20 ps time resolution. The pulse repetition rate is reduced for time-resolved emission measurements by a factor of 10 using an acousto-optic modulator.

The lateral resolution of the microscope is determined by the size of the laser beam at the focal point of the objective. Since the probability of two-photon excitation and second-harmonic generation scales with the square of the laser intensity, efficient excitation occurs only at the focal point, resulting in confocal-like behavior and a lateral resolution that is smaller than the diffraction limit of the near-infrared laser spot. The diameter of the excitation region is estimated to be approximately 350 nm. Images obtained from 100 nm fluorescent beads yield a point spread function width of ~400 nm. Samples are placed on a glass substrate with an etched grid so that individual objects examined in the optical microscope can also be located in an SEM to obtain high-resolution structural images.

■ RESULTS AND DISCUSSION

This paper investigates the carrier recombination dynamics in photoexcited ZnO rods using steady-state and time-resolved two-photon emission microscopy. The discussion of the experimental results is divided into two sections. The first section describes the two-photon imaging of individual structures and the spatial variation of the photoluminescence. The next section presents time-resolved measurements that probe the trap-mediated recombination dynamics and photoluminescence spectroscopy measurements performed at a specific point in the structure. We have performed experiments on both as-grown and annealed structures, which have enabled us to interpret the spectra in terms of particular defect mechanisms.

Spatially Resolved Photophysics of Individual ZnO Structures. ZnO is a wide band gap semiconductor that can be photoexcited by the absorption of a single UV photon or by simultaneous two-photon absorption in the near-infrared. The resulting free carriers (electron and holes) either relax into excitonic states that lie about 60 meV below the conduction band edge or into trap states associated with defects in the crystal lattice or the structure's surface. The near-UV band originates from a combination of excitonic and electron−hole plasma emission. The excitonic state is most stable at low excitation intensities (i.e., low carrier density) and emits around 390 nm. At higher excitation intensities the photoproduced carriers can exceed the Mott density threshold,[26] at which point the distance between the electron−hole pairs is comparable to the exciton Bohr radius, leading to the formation of an electron−hole plasma, whose emission is shifted to lower energy due to band gap renormalization.[17,26−29] Our observation of band-edge emission centered around 390 nm indicates our experiments are within the low-density regime. Trap recombination in ZnO gives rise to a broad green emission band, whose position and shape depend upon the structure's underlying shape and the synthetic method, signifying the presence of a rich defect chemistry in this material.[2,3] This project focuses particularly on the trapping dynamics in individual needle-shaped ZnO rods.

Here needle-shaped rods are excited with a 730 nm femtosecond laser pulse focused to a diffraction-limited spot by a microscope objective. Because the resulting two-photon excitation region is small (350 nm) compared to the rod's size (5−10 μm in length), only a portion of the rod is excited, allowing us to perform spatially resolved measurements by positioning the excitation spot over a specific part of the structure (e.g., middle or end of the rod) and monitoring the photoluminescence in either a time-integrated or time-resolved fashion. Emission images of individual structures can be obtained raster scanning the sample stage while monitoring either band-edge (390 nm) or trap (550 nm) emission channels.

Care was taken to ensure that experiments were performed at low excitation intensities. Although we find that the images are not sensitive to the pulse energy, other spectroscopic measures (e.g., emission spectra and lifetimes) are intensity-dependent, indicating that the photophysics of these materials depend upon carrier concentration, consistent with observations made by other groups.[30,31] Photoluminescence decays were collected at successively lower pulse energies until a limiting value of the trap emission lifetime was obtained to avoid intensity-dependent effects. This was typically less than 0.3 nJ/pulse.

Two-Photon Imaging. Photoluminescence images obtained via collection of the band-edge (390 nm) and trap emission (550 nm) following two-photon excitation of a single ZnO needle-shaped structure at 730 nm are shown in the right two panels of Figure 3, along with a detailed structural image obtained in an SEM shown at the left. The SEM image of this rod, which is typical of the size and shape of the ZnO rods used in this experiment, shows it to be a crystalline structure ~10 μm in length (~1.5 μm at its widest point), with a hexagonal cross section that tapers to approximately 300 nm at the ends. The two-photon emission images in the exciton and trap emission channels show significant variation in the emission intensity

dx.doi.org/10.1021/jp1118426 |J. Phys. Chem. C XXXX, XXX, 000–000

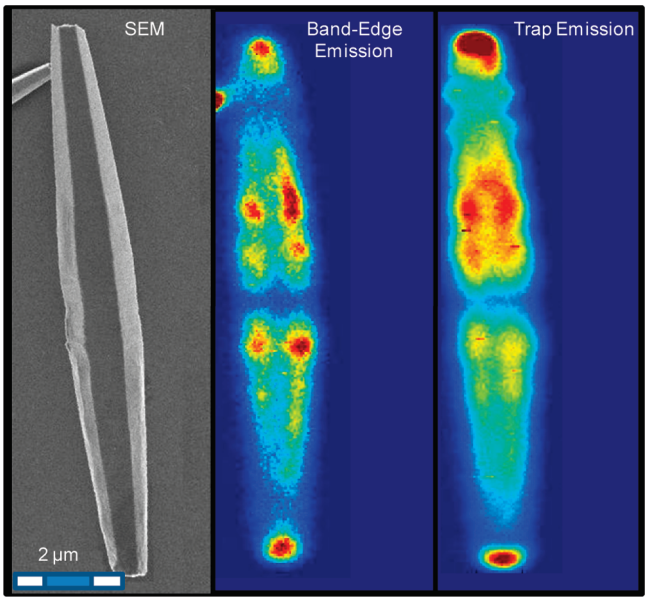

Figure 3. (Left) Scanning electron microscopy image of a typical ZnO rod used in our experiments. The structure is ~10 μm in length and ~1.5 μm in the center, tapering down to ~500 nm at the end. (Middle) Band-edge emission (detected at 390 nm) and (right) trap (detected at 550 nm) emission images observed following two-photon excitation at 730 nm of the rod depicted in the SEM image. Each image shows enhanced intensity at the ends of the structure. The dark area in the center is attributed to the presence of a grain boundary. The enhanced intensity at the vertices may be due to light coupling into whisper gallery modes.

across the structure. Evident in both images are areas of low intensity in the middle of the rod, enhanced emission along the hexagonal corners adjoining each facet, and high intensity at the ends of the structure.

The enhanced intensity at the vertices and periodic modulation along the long axis of the rod suggest that the emission images are influenced by a complex optical mode structure. Similar intensity variation is observed in second-harmonic images,[19] where it is linked to the presence of optical cavity modes oriented transverse to the rod axis. The rod's cross section supports both Fabry−Perot (FP) modes between the parallel facets and ringlike cavity modes arising from total internal reflection off each of the six facets, called whispering gallery modes (WGM). Because the cross-sectional diameter of the needle-like structures changes along the long axis of the rod, optical resonances will appear at distinct locations. It is this periodic variation that suggests the intensity modulation is the result of optical cavity modes and not simple prism effects that redirect light back toward the objective. In principle either resonance type (FP or WGM) could influence the emission images; however, the enhanced intensity at the vertices suggests that it is the WGM that give rise to the intensity modulation observed in these images.

Single-Point Spectroscopy. Spectroscopic information from different points within a single structure can be collected through precise positioning of the focused laser spot and directing the emission into a scanning monochromator/PMT, streak camera, or time-correlated single-photon counting instrumentation, for time-integrated and time-dependent measurements, respectively.

Given the localized nature of the excitation, we anticipate that emission should only emanate from the region excited by the laser pulse. However, because our microscope does not employ an aperture in the detection path, it collects all of the emission in the objective's field of view and cannot distinguish between light emitted from the excitation region versus light emitted from other parts of the structure, perhaps due to carrier transport and/or wave guiding from the excitation spot. To evaluate the spatial locations giving rise to the detected emission, the light collected by the objective was imaged on a charge-coupled device (CCD) detector (Figure 4). The bright spot in the middle of the rod is due to the intense emission created by the focused laser beam, whereas the two dimmer spots on either side represent photoluminescence that is emanating remotely from the rod ends. Given the low carrier mobilities in ZnO,[32] it is unlikely that this emission from these remote locations is the result of carrier transport. It is more likely the result of a wave guiding of light emitted along the rod axis to the ends of the structure. Enhanced emission at the rod ends has been observed in the emission images of ZnO wires and rods obtained by other groups[13,30] and attributed to wave guiding along the longitudinal axis of the structure. However, in those images the emission from the ends was more intense than that from the rod's interior, perhaps due to an experimental arrangement in which the entire rod is excited, thus allowing wave-guided light to stimulate emission as it propagates along the rod. Despite the presence of wave guiding in these images, the majority of the emission collected by the objective emanates from the location of the laser excitation, indicating that coupling into the wave-guiding modes is relatively weak and contributes negligibly to the observed emission at any given region of the structure.

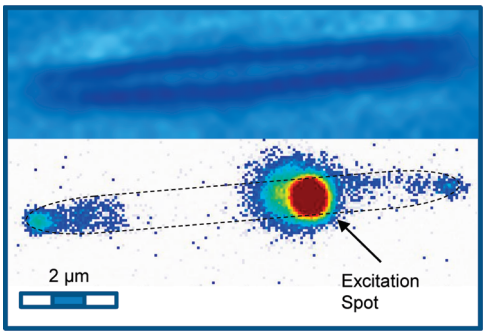

Figure 4. Bright-field and corresponding fluorescence image (390 nm) collected using a CCD camera. The bright spot in the fluorescence image represents emission from the excitation region and represents the dominant source of emission in our experiments. Fluorescence emanating from the ends of the structure is probably due to light coupling into wave-guiding modes.

Through the course of these experiments we monitored the emission in ≈20 different structures. Although there is some variation from structure to structure, the spectra and lifetimes observed across the ensemble show some common features. Figure 5 shows the photoluminescence spectrum obtained following localized 730 nm two-photon excitation in the midpoint of the rod depicted in Figure 3, which is typical of the structures studied. The two most prominent features in the spectrum are the narrow band-edge emission around 390 nm that is characteristic of exciton fluorescence at low excitation intensity and the much broader visible emission (500−650 nm) that arises from the trapping of charge carriers at defect sites. The sharp feature centered at ~365 nm corresponds to the second harmonic that is generated by the ZnO.[19] The relative intensity of the

dx.doi.org/10.1021/jp1118426 |J. Phys. Chem. C XXXX, XXX, 000–000

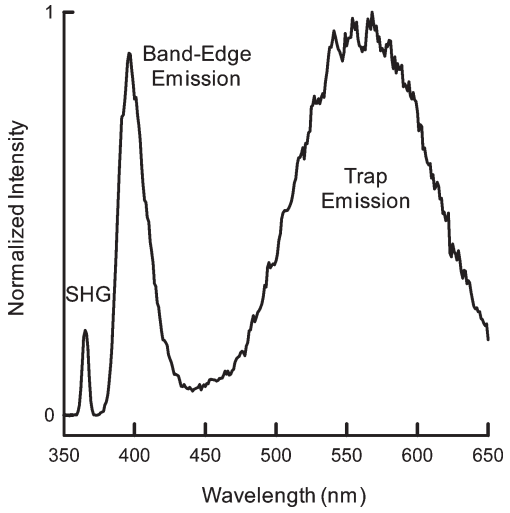

Figure 5. ZnO emission spectrum observed following a two-photon excitation (730 nm) in the center of the rod shown in Figure 3. The sharp feature centered at 365 nm corresponds to second-harmonic generation. The emission band at 390 nm arises from exciton recombination. The broad emission centered at 560 nm corresponds to trap recombination events. The relative intensity of the trap to band-edge emission is suggestive of a high defect density.

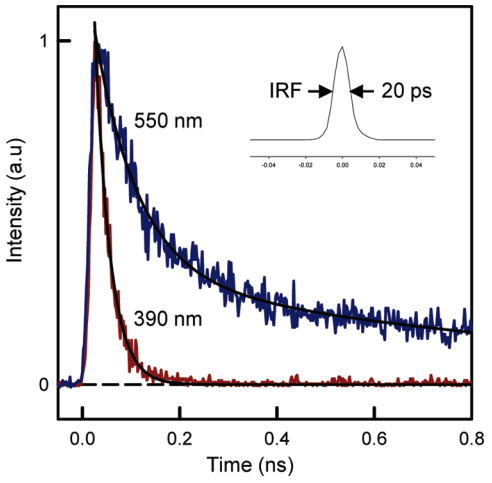

Figure 6. Time-resolved photoluminescence measurements collected following 730 nm two-photon excitation of an individual ZnO rod. The band-edge emission has an ~30 ps lifetime; the streak camera time instrument response (shown in the inset) is ~20 ps. The trap emission bands are multiexponential, displaying a fast subnanosecond component, followed by slower components that decay in tens to hundreds of nanoseconds. The instantaneous rise in the trap emission suggests that the initial trapping events occur within the first 20 ps following photoexcitation.

trap emission compared with the band-edge emission at lower pulse energies is suggestive of a high defect density.

The electron−hole recombination dynamics in individual structures were characterized using ultrafast emission methods. Figure 6 shows the decay of the band-edge (390 nm) and trap emission (550 nm) following the excitation of a localized spot in a single ZnO structure. The band-edge emission decays with an approximately 30 ps lifetime (Figure 6), consistent with experiments conducted on bulk or thin-film ZnO by other groups that show a band-edge emission lifetime of 50−100 ps resulting from free exciton recombination.[33−35] The trap emission rises within the instrument response, and the absence of a delayed rise (Figure 6) suggests that the initial trapping events occur within the first 20 ps following excitation. The decay is multiexponential with time components ranging from subnanosecond (~100−250 ps) to tens to hundreds of nanoseconds (Figure 6), the longer of which are consistent with previous reports.[35,36]

Spatial Variation in Defect Density. One of the most striking features in the two-photon emission images is the dark region that bisects the rod at its midpoint. Shown in the top of Figure 7 are defect emission transients collected at 550 nm from three different locations (middle, interior, and end) in a single ZnO rod, whose trap emission image is shown as the inset. The three different spots exhibit different decay kinetics, indicative of a spatial heterogeneity in the trap recombination dynamics. Interestingly, the trap recombination is faster at the rod midpoint compared to the two other locations, which is consistent with an increase in the nonradiative rate and a greater defect density at that location. One possible cause of an increase in the trap density is a grain or twinning boundary that is not apparent in the SEM image. Although the majority of rods (60−70%) show the decreased intensity in the trap emission image at the rod midpoint, in the rest the dark region is less apparent or absent altogether. The lower panel shows a similar set of transients obtained from one such rod. In these rods the emission decay occurs slowest in the middle of the structure and more rapidly at the end, suggesting a lower defect density at the rod midpoint. Although it is unclear why the remaining 30−40% of the rods do not show this dark region, it could be a consequence of a difference in the nature of the grain boundary that was formed as the crystal was grown in solution. Together, these observations point toward the potential for an inhomogeneous distribution of defect sites and for different regions of the same structure to show different dynamical signatures.

Trap-Mediated Recombination. The precise mechanisms that give rise to the broad defect emission in ZnO remain highly controversial. This is exacerbated by the dependence of visible emission on particle shape, size,[17] and synthetic procedure.[1,20,21] In principle, the trap emission could originate from either surface defects (i.e., dangling bonds) or imperfections in the crystal lattice, which include extrinsic impurities and intrinsic lattice defects.[20−22] Surface emission has been implicated in smaller structures with large surface-to-volume ratios,[17,35,37−39] and larger structures excited with UV light,[13,17,37,40] where the photogenerated carriers are likely produced near the surface of the structure as a consequence of the shallow penetration depth (≈100 nm). However, given the size of our structures and the likelihood that the near-infrared two-photon excitation produces carriers throughout the structure, we anticipate that the majority of the defect emission in our experiments originates from lattice defects within the crystal interior.

Our discussion of the trap recombination involves comparisons between as-grown and annealed structures. A combination of steady-state and time-resolved observations indicates that the trap emission band is composed of two overlapping transitions with different spectral characteristics. The lower-energy band, which has a greater contribution in the spectrum of the as-grown structures, has $\lambda_{max} \approx 560$ nm and is characterized by a time-dependent red shift and a photoluminescence lifetime that increases with decreasing defect density. It is attributed to DAP emission. The higher-energy band ($\lambda_{max} \approx 520$ nm) is

dx.doi.org/10.1021/jp1118426 |J. Phys. Chem. C XXXX, XXX, 000–000

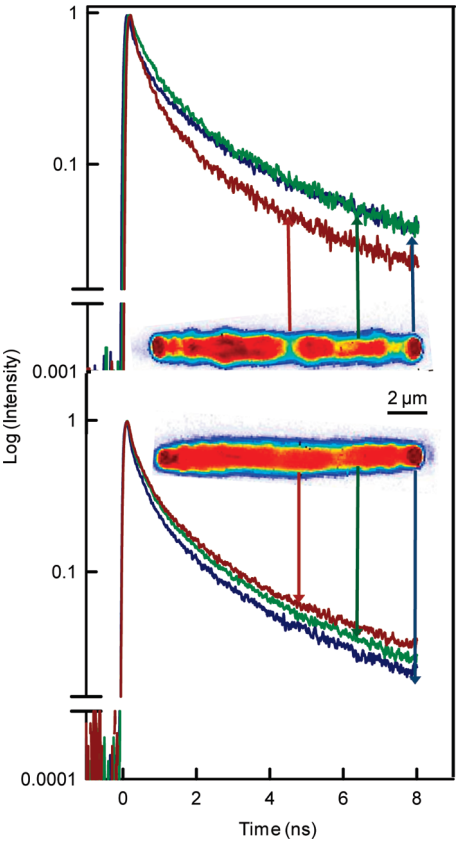

Figure 7. Trap emission decays collected from the middle, interior, and end of structures with the darkened region at the rod midpoint (top) and without (bottom). Structures that show a darkened region have emission decays that are faster in the center of the rod compared to other points, consistent with an increase in the nonradiative rate due to the increased defect density around the grain boundary. The structure without the darkened region shows the emission decay at the end to be faster than the middle.

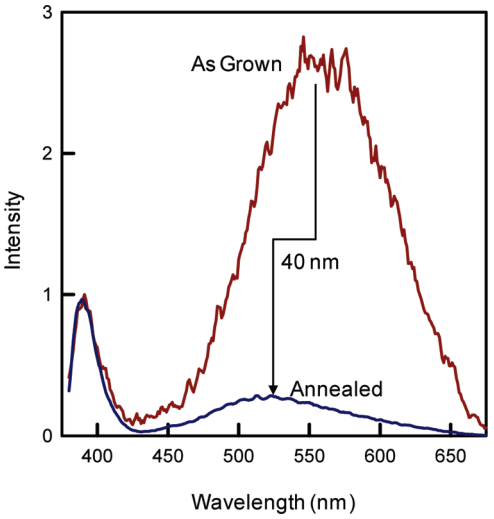

Figure 8. Steady-state spectra observed before and after annealing. The spectra were collected from the center of the rod shown in Figure 3 following two-photon excitation at 730 nm. The first spectrum was collected from the as-grown structure; then, following annealing at 550 °C for 4 h, the emission spectrum was recollected from the same position in the same rod. The spectra, which are normalized to the maximum of the band-edge emission, show a drastic reduction in the overall defect density. In addition, an ∼40 nm blue shift in the spectrum following annealing is observed, which is attributed to the presence of two overlapping emission bands, with the high-energy band less affected by annealing.

unaffected by annealing and is the major contributor to the photoluminescence spectrum in the annealed structures. It is characterized by a shorter lifetime that does not depend upon defect density and is attributed to recombination of electrons in the conduction band with holes trapped at deep acceptor sites. Our discussion below first compares the photoluminescence spectra obtained before and after annealing and then describes the time-dependent spectral evolution.

Photoluminescence Spectra. Shown in Figure 8 are emission spectra acquired from the *same* location in the *same* ZnO rod before and after annealing at 550 °C for 4 h. There is a clear decrease in the trap emission intensity from 130% of the band-edge emission before annealing to 15% afterward, consistent with an overall reduction in the defect density. In addition, the spectrum shifts from about 560 nm in the as-grown structures to 520 nm after annealing. Although the ∼40 nm (∼0.15 eV) shift occurs with little change in the width of the spectrum, there appears to be a slight distortion of the spectrum with a tail extending toward longer wavelengths. The observations shown in Figure 8 were not isolated to this particular structure, and a similar (10−40 nm) blue shift was observed in a majority of the 52 rods we analyzed, with a minority displaying a shift of lesser magnitude (∼5 nm). The shift of the band suggests that the trap emission is actually composed of overlapping emission bands involving different defect types, of which at least one is mobile at the 550 °C annealing temperature.

Time-Resolved Emission. The decay kinetics vary across the trap emission band. Shown in Figure 9A are three transients obtained at different emission wavelengths for the as-grown structures. Each was fit to a triexponential decay function of the form $I(t) = a_1 \exp(-t/\tau_1) + a_2 \exp(-t/\tau_2) + a_3 \exp(-t/\tau_3)$, and the fit parameters for these and two other decays are presented in Table 1. All exhibit ultrafast (0.2 ns), intermediate (0.5−1 ns), and slow decay (3.0−6.5 ns) components, with the ultrafast contribution accounting for about 50% of the amplitude at early times and the two slower components accounting for the other half. A systematic trend is observed in the two slower components (τ_1 and τ_2), which exhibit generally longer decay times and greater amplitudes at the redder emission wavelengths, suggestive of a dynamic shift in the emission band.

The magnitude and temporal evolution of this shift is apparent in the emission spectra reconstructed at different times from decays obtained at a series of detection wavelengths collected between 470 and 600 nm (Figure 9B). The individual points in the figure correspond to the intensity observed at specific times after photoexcitation for each of the detection wavelengths. The solid lines represent fits of each spectrum to a stretched Gaussian function, $f(\lambda) = c_1 \exp[-1/2(\lambda - \lambda_O)^2/(c_2 + c_3(\lambda - \lambda_O))]$, which accounts for the asymmetric line shape. The emission spectra show a time-dependent red shift of ∼10 nm during the first 15 ns after photoexcitation, as depicted by the bold line connecting the maximum of each of the spectra in the figure. We consistently observe the red shift in all the structures, and the magnitude generally ranges from 3 to 12 nm, with the majority shifting between 4 and 8 nm. Figure 9C depicts the kinetics of the spectral shift by showing the magnitude of the shift

dx.doi.org/10.1021/jp1118426 |J. Phys. Chem. C XXXX, XXX, 000–000

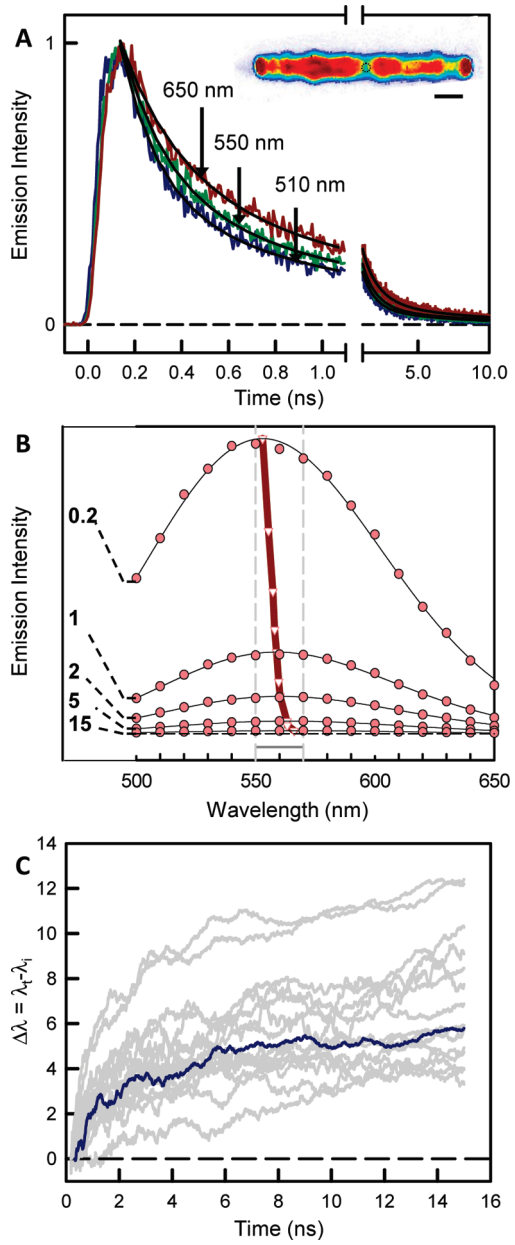

Figure 9. Time-resolved emission data obtained from two-photon photoexcitation at 730 nm of an as-grown structure. The location of the excitation is indicated by the circle on the trap emission image shown in the inset (the scale bar corresponds to 2 μm). The top panel (A) shows the emission decay at three different detection wavelengths, with shorter lifetimes observed at higher emission energies. The emission spectra shown in the middle panel (B) were reconstructed from decays obtained at a series of detection wavelengths and correspond to spectra at 0.2, 1, 2, 5, and 15 ns. They reveal an 8−10 nm time-dependent red shift in the trap emission band. The shift of the maximum from 16 rods is displayed in the bottom panel (C). The red shift varies in magnitude between 4 and 10 nm and occurs within the first 10−15 ns following photoexcitation. An example from an average structure is shown in blue to highlight the trend.

($\Delta\lambda = \lambda_t - \lambda_i$) as a function of time for 16 different rods. The shift exhibits multiple kinetic components, with a rapid shift of the band occurring at early times (∼2−4 ns), followed by a slower shift (∼5−15 ns) to its asymptotic wavelength.

The results from a similar set of experiments performed at the same point in this rod following a 4 h anneal at 550 °C are shown in Figures 10 and 11. Figure 10 compares the trap emission decay at 550 nm before and after annealing. While the as-grown structure decays completely to zero during the 50 ns detection window, after annealing it does not, indicating the emergence of a long-lived decay component. Each transient was fit to a decay function of the form $I(t) = a_1 \exp(-t/\tau_1) + a_2\exp(-t/\tau_2) + a_3 \exp(-t/\tau_3) + a_4$. The addition of the constant (a_4) accounts for the amplitude of this ultraslow decay component, which was measured in other experiments to be in the range of 1−2 μs. While the lifetime of the fastest decay component (∼0.2 ns) is unchanged by annealing (Table 1), the slower components exhibit significant increases in their decay times to 1.5 and 12 ns for τ_2 and τ_3, respectively (Table 1), as well as the appearance of a 1−2 μs component. In addition, the relative contribution of the slow components ($a_2 + a_3 + a_4$) to the overall decay decreases from 50% in the as-grown structures to about 30−40% in the annealed rods. Together, these observations indicate that the physical processes giving rise to the emission at early times (t < 0.2 ns) and later times (t > 0.5 ns) are different.

Shown in Figure 11A are transients obtained at three different detection wavelengths. Whereas the transients obtained from the as-grown structures show slower decays at longer detection wavelengths, after annealing this trend is reversed. The time-resolved spectra reconstructed from the individual transients show an apparent shift to higher energy over time for the annealed structures at early time (0−2 ns) (Figure 11B). However, in contrast to the systematic variation of the lifetimes across the emission band observed in the as-grown structures, the τ_1 and τ_2 lifetimes observed in the annealed structure show no systematic variation across the spectrum (τ_3 shows a slight increase from 12.0 to 12.6 ns at longer detection wavelengths) (Table 1). The consistency in τ_1 and τ_2 across the band suggests that the net blue shift observed in the emission spectrum at early times is due to a variation in the relative amplitudes of the ultrafast and slow components and not a dynamic shift of the spectrum.

The steady-state and time-resolved photoluminescence spectra are consistent with the presence of at least two overlapping bands within the static trap emission spectrum of the as-grown structures. The defect emission in the as-grown structures is composed largely of a low-energy band (λ_{max} = 560 nm) that exhibits a time-dependent red shift in the first 10−15 ns after photoexcitation and has a lifetime that increases with decreasing defect density. Upon heating at high temperature, the defects associated with this band are preferentially annealed out of the lattice, leaving behind a spectrum that is dominated by a higher-energy band (λ_{max} = 520 nm). This band is characterized by an ultrafast lifetime (0.2 ns) that is unaffected by the decrease in defect density. The question thus arises: what is the physical origin of these two emission bands?

Recombination Mechanisms. With the potential for a variety of different defect types, the trap emission band in ZnO is likely composed of multiple components. Generally speaking, defects can be classified as either donors, which trap electrons, or acceptors, which trap holes. The transitions that can give rise to the trap photoluminescence can include donor recombination with a hole in the valence band ($D \rightarrow h^+$), acceptor recombination with an electron in the conduction band ($A \rightarrow e^-$), and recombination between an electron localized on a donor with a hole localized on an acceptor. The latter mechanism is known as DAP recombination[23] and occurs between donor and acceptor

dx.doi.org/10.1021/jp1118426 |J. Phys. Chem. C XXXX, XXX, 000–000

Table 1. Summary of Nonlinear Least-Squares Fits of Emission Decays for the As-Grown and Annealed Structures at Different Detection Wavelengths[a]

	ultrafast		intermediate		slow		ultraslow
detection wavelength (nm)	τ_1 (ns)	(a_1)	τ_2 (ns)	(a_2)	τ_3 (ns)	(a_3)	(a_4)
			As-Grown Rods				
480	0.10	(0.50)	0.56	(0.41)	3.77	(0.09)	
510	0.15	(0.51)	0.77	(0.41)	4.88	(0.08)	
550	0.16	(0.47)	0.82	(0.44)	5.37	(0.09)	
600	0.19	(0.45)	0.92	(0.45)	5.99	(0.10)	
650	0.22	(0.45)	1.01	(0.45)	6.54	(0.10)	
			Annealed Rods				
480	0.17	(0.68)	1.53	(0.18)	12.01	(0.11)	(0.03)
510	0.22	(0.59)	1.66	(0.24)	12.27	(0.14)	(0.03)
550	0.22	(0.58)	1.66	(0.25)	12.25	(0.14)	(0.03)
600	0.21	(0.67)	1.52	(0.21)	12.48	(0.10)	(0.02)
650	0.24	(0.73)	1.59	(0.18)	12.56	(0.07)	(0.02)

[a] Decays for the as-grown rods were fit to a six-parameter triexponential decay function, whereas a seven-parameter form was used for the annealed rods. Uncertainties in the amplitudes are ≈3%. For each component the lifetime and relative amplitude (in parentheses) are displayed. Uncertainties in the intermediate and slow lifetimes are also ≈3%. Since the lifetime of the ultrafast component is close to the instrument response of the time-correlated single-photon counting apparatus (100 ps) its uncertainty is probably closer to 10%.

defects that are in close proximity within the crystal lattice. Because the ionized acceptors are negatively charged, they tend to attract and capture the photogenerated holes, making the probability for donor recombination with the valence band unlikely.[3,41] At the same time, this suggests the dominant transitions are between electrons in the conduction band, or localized in shallow defects, with holes trapped at acceptor sites (Figure 1).

The time-dependent red shift associated with the lower-energy feature suggests that it corresponds to DAP emission resulting from a high defect density in the as-grown structures. When the donor and acceptor defects are well-separated from each other, the primary transitions correspond to recombination of the trapped electron (or hole) with its free carrier counterpart in the valence (or conduction) band. If the donors and acceptors are in close spatial proximity, the electron bound to the donor can recombine with the acceptor-bound hole, resulting in DAP emission. The emission energy from such a transition is given by[23]

$$\Delta E = E_g - E_I = E_g - \left(E_D + E_A - \frac{e^2}{\varepsilon d}\right) \quad (1)$$

where E_g is the band gap energy and E_I is the energy needed to ionize both the electron and hole into their respective bands, E_D and E_A are the ionization energies of the isolated donors and acceptors, respectively, ε is the dielectric constant, and d is the distance between them in the lattice. Pairing of the defects perturbs the donor and acceptor levels toward their respective band edges,[23] and as a consequence, the pairs that are closer together will emit at higher energy. Pairs that are in close spatial proximity will also experience a greater wave function overlap and recombine faster than those that are further apart, and it is this distribution of recombination rates that gives rise to the multiexponential form of the photoluminescence decay. The result is an initially blue photoemission that shifts to the red as time progresses.

Donor−acceptor pair emission has been implicated in a number of experiments investigating the origin of the ZnO photoluminescence, and transitions between a variety of defect types have been observed.[2,20,21] These include recombination involving shallow donors and shallow acceptors that give rise to a blue emission at ≈400 nm,[21,42] as well as pairs involving deep trap levels, which contribute to the yellow-green emission.[3,17,20,21] Because carriers undergo trapping and detrapping due to thermal

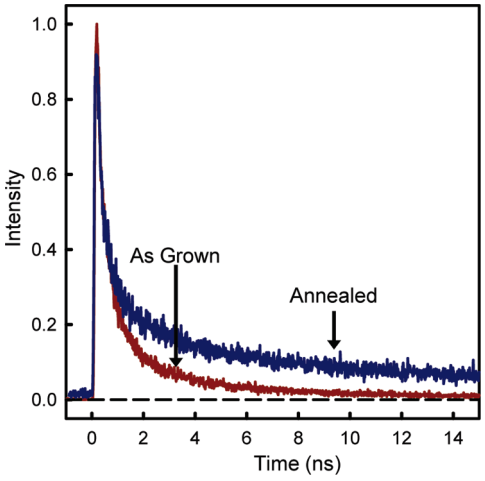

Figure 10. Emission decays collected at 550 nm from the same position in the same structure, before and after annealing. The decay lifetime from the as-grown structure is characterized by an ultrafast (0.2 ns), intermediate (1 ns), and slow (7 ns) component. The slower components, which decay almost completely by 50 ns in the as-grown structure, are much longer following annealing, where emission is still observed at 50 ns. Data collected on other annealed structures suggest the photoluminescence decays completely after 2 μs. The fastest decay observed at early times is attributed to recombination between the conduction band and the hole-bound acceptor with kinetics that are independent of annealing (∼0.2 ns lifetime before and after annealing). The longer decay components are attributed to donor−acceptor pair (DAP) emission and are highly dependent on temperature. The increased lifetime following annealing is consistent with reduced donor defect density.

dx.doi.org/10.1021/jp1118426 |J. Phys. Chem. C XXXX, XXX, 000–000

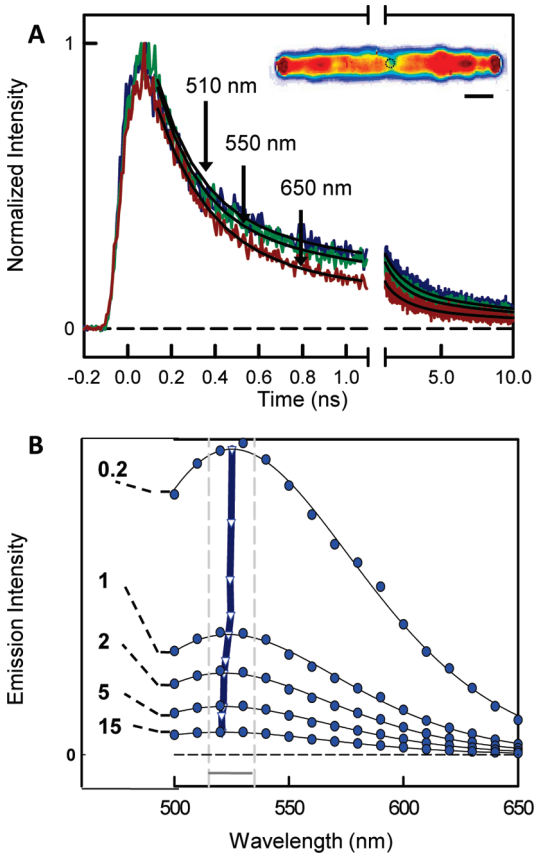

Figure 11. Time-resolved emission data taken after annealing the rod shown in Figure 9 (the scale bar corresponds to 2 μm). The location of the excitation is indicated by the circle on the trap emission image shown in the inset. The top panel (A) shows the emission kinetics have a faster decay at lower energies in contrast to our observations before annealing. The lower panel (B) shows emission spectra reconstructed from transients obtained at a series of detection wavelengths and correspond to spectra at 0.2, 1, 2, 5, and 15 ns. They show an apparent blue shift of the emission band with increasing time. The consistency of τ_1 and τ_2 (Table 1) across the band suggests the apparent blue shift is due to variation in the relative amplitudes of the ultrafast and slow components and not a dynamic shift of the spectrum.

activation, DAP emission is sensitive to temperature. This is particularly true for the higher-energy DAP emission involving shallow defects, which is observed at low temperatures (5 K); however, deeper traps are much less susceptible to thermal detrapping and DAP recombination has been implicated in the visible emission at much higher temperatures.[31]

It is this sensitivity to thermal detrapping that makes the temperature dependence a particularly useful method of assigning DAP recombination. With respect to the time-dependent spectral shifts observed here, we would expect that carrier trapping and detrapping processes at higher temperatures would allow carrier migration through the bands and mute the red shift; that is, measurements at lower temperatures should show greater spectral shifts. Such observations have already been made in polycrystalline ZnO films. In those experiments, Egelhaaf and Oelkrug observed a red shift of ~2000 cm^{-1} within 600 ns after excitation of ZnO at 77 K; however, at room temperature almost no shift was observed.[43] Since our experiments are conducted at room temperature, the red shift we observe is comparatively small (~300 cm^{-1}) compared to Egelhaaf and Oelkrug's observations at 77 K, and we would expect a much larger shift at lower temperature. Although such observations would provide strong evidence to support DAP recombination, low-temperature measurements are currently not feasible in our two-photon emission microscope.

However, in addition to a distinctive dependence on temperature, DAP recombination will also show a characteristic dependence on the defect density. Annealing crystalline materials at high temperatures is a well-established method of reducing the defect density in semiconductor systems, and comparisons between the as-grown and annealed structures provides support for the DAP assignment.

As the defect density decreases, the average spacing between donors and acceptors increases, which alters both the emission lifetime and the magnitude of the spectral shift. Because the reduced wave function overlap at larger separations will lead to an increase in the DAP recombination time, the increase in the photoluminescence lifetime from tens of nanoseconds in the as-grown structures to several microseconds in the annealed rods (Figure 10) supports the DAP assignment. The magnitude of the spectral shift is given by

$$\Delta(\Delta E) \approx \frac{e^2}{\varepsilon}\left(\frac{1}{\langle d\rangle_{t=\infty}} - \frac{1}{\langle d\rangle_{t=0}}\right) \approx -\frac{e^2}{\varepsilon\langle d\rangle_{t=0}} \qquad (2)$$

where $\langle d\rangle_{t=0}$ is the average separation between a donor and the nearest acceptor at $t = 0$. As the average separation increases, the interaction between the donor and acceptor states diminishes, and the magnitude of the spectral shift decreases. The time-dependent shift in the low-energy band is masked at early times in the annealed structures by the apparent net blue shift of the spectrum. That being said, there is a slight increase in τ_3 at longer wavelengths, which is consistent with a significantly reduced red shift and the DAP assignment.

Defect Types. Because of the differing reports in the literature, precise assignment of the donor and acceptors to particular trap types is difficult. The trap emission originates from imperfections in the crystal lattice that include extrinsic impurities and intrinsic lattice defects.[20−22] There have been numerous experimental reports in the literature that systematically probe the defect chemistry in ZnO and relate it to specific spectroscopic signatures.[17,21,41,44−46] Perhaps just as numerous are the theoretical models that attempt to make similar assignments.[20,47−49] While this research has been conducted for decades the exact assignments still remain inconclusive and controversial. This is exacerbated by the dependence of visible emission on particle shape, size,[17] and synthetic procedure.[1,20,21] For example, a survey of particles grown by different synthetic methods shows significant variation in their trap emission spectra,[2] underscoring the difficulties in making such assignments.

Among the different types of intrinsic defects (vacancies, interstitials, and substitutions), perhaps the two most heavily cited for giving rise to the defect emission are oxygen (V_O) and zinc vacancies (V_{Zn}), each of which can exist in either neutral, single-, or doubly ionized states.[20,21] In n-type ZnO these defects exist in their most negatively charged state, making the oxygen vacancy a neutrally charged donor (V_O) and the Zn vacancy a doubly charged acceptor (i.e., V_{Zn}^{2-}). There have been numerous reports that attribute the defect emission to single-ionized oxygen vacancies (V_O^+),[50−55] which, in principle, could also act as an acceptor; however, it is uncertain that V_O would exist in a

dx.doi.org/10.1021/jp1118426 |J. Phys. Chem. C XXXX, XXX, 000–000

singly ionized state under n-type conditions and several recent reports have suggested that it is thermodynamically unstable.[20,21]

If the trap emission observed in our structures originates entirely from native defects, then one potential assignment would involve Zn vacancies in their doubly ionized state, V_{Zn}^{2-}, serving as acceptor defects.[20−22] Upon photoexcitation, a hole in the valence band $(h^+)_{VB}$ can localize on one of these sites and subsequently recombine with an electron in the conduction band, or a shallow donor, to result in the emission of a photon (i.e., $V_{Zn}^{-} + (e^-)_{CB} \rightarrow V_{Zn}^{2-} + h\nu$). The emission energy of such a transition would be approximately $E_g - E_A$, where E_g is the band gap and E_A is the hole ionization energy. There are discrepancies in the literature for the hole ionization energy from V_{Zn}^{-} (i.e., $V_{Zn}^{-} \rightarrow V_{Zn}^{2-} + (h^+)_{VB}$), with reports placing it between 0.9[20,43] and 2.8 eV.[2,22] A value closer to the lower limit would correspond to the emission of an ∼500 nm photon, consistent with the higher-energy emission band. There are several candidates for the shallow defects involved in the DAP emission. If both the DAP emission and the higher-energy emission observed in annealed structures involve the same acceptor defect, namely, V_{Zn}^{-}, then the shallow defects involved in the DAP emission must lie within 150−200 meV of the conduction band edge. Although neutral oxygen vacancies, V_O, are one possibility, it is unclear whether they would be annealed out of the lattice at the temperature used here. Zinc and hydrogen interstitials are more likely candidates. They lie within 150 meV of the conduction band edge, and since they have low migration barriers, they are likely to be annealed from the structure, disrupting the DAP transition. The invoking of native defects in the DAP emission is consistent with assignments made by other groups.[31,43]

Although our structures are not intentionally doped, we cannot completely rule out extrinsic defects arising from a variety of impurities, which have also been implicated in ZnO DAP emission.[3,20,21,42,56] In particular, defects created by Li and Cu inclusion have been implicated, with Li-doped materials giving rise to yellow luminescence centered around 570 nm and Cu giving rise to the green emission centered around 500 nm.[3,21,45,56,57]

CONCLUSION

We utilize nonlinear microscopy methods to study the trap emission dynamics in single needle-shaped ZnO rods. Analysis of trap emission decays obtained using two-photon emission microscopy for both as-grown and annealed structures suggest that the trap emission band is composed of two overlapping emission bands. The lower-energy band, which is more prominent in the as-grown rods, contributes to the emission on longer time scales ($t >$ 0.5 ns), exhibits a time-dependent spectral red shift during the first 10−15 ns after photoexcitation, and has a lifetime that depends on defect density. We attribute these observations to DAP emission. The higher-energy band is characterized by an ultrafast (0.2 ns) lifetime and is attributed to recombination between electrons in the conduction band and holes trapped at deep defect sites.

AUTHOR INFORMATION

Corresponding Author

*E-mail: john_papanikolas@unc.edu.

ACKNOWLEDGMENT

This project was supported by a Grant from the National Science Foundation (CHE-0809045).

REFERENCES

(1) Wang, Z. L. *J. Phys.: Condens. Matter* **2004**, *16*, R829.
(2) Djurisic, A. B.; Leung, Y. H. *Small* **2006**, *2*, 944.
(3) Ozgur, U.; Alivov, Y. I.; Liu, C.; Teke, A.; Reshchikov, M. A.; Dogan, S.; Avrutin, V.; Cho, S. J.; Morkoc, H. *J. Appl. Phys.* **2005**, *98*, 041301.
(4) Ju, S. H.; Lee, K.; Janes, D. B. *Nano Lett.* **2005**, *5*, 2281.
(5) Ng, H. T.; Han, J.; Yamada, T.; Nguyen, P.; Chen, Y. P.; Meyyappan, M. *Nano Lett.* **2004**, *4*, 1247.
(6) Park, W. I.; Kim, J. S.; Yi, G. C.; Bae, M. H.; Lee, H. J. *Appl. Phys. Lett.* **2004**, *85*, 5052.
(7) Ryu, Y. R.; Lee, T. S.; Lubguban, J. A.; White, H. W.; Kim, B. J.; Park, Y. S.; Youn, C. J. *Appl. Phys. Lett.* **2006**, *88*, 241108.
(8) Wang, X. D.; Zhou, J.; Song, J. H.; Liu, J.; Xu, N. S.; Wang, Z. L. *Nano Lett.* **2006**, *6*, 2768.
(9) Chen, Y. F.; Bagnall, D.; Yao, T. F. *Mater. Sci. Eng., B* **2000**, *75*, 190.
(10) Law, M.; Sirbuly, D. J.; Johnson, J. C.; Goldberger, J.; Saykally, R. J.; Yang, P. D. *Science* **2004**, *305*, 1269.
(11) Ryu, Y. R.; Lee, T. S.; Lubguban, J. A.; White, H. W.; Park, Y. S.; Youn, C. J. *Appl. Phys. Lett.* **2005**, *87*, 153504.
(12) Zeng, H. C. *J. Mater. Chem.* **2006**, *16*, 649.
(13) Johnson, J. C.; Yan, H. Q.; Yang, P. D.; Saykally, R. J. *J. Phys. Chem. B* **2003**, *107*, 8816.
(14) Irene, E. *Electronic Materials Science*; John Wiley & Sons: Hoboken, NJ, 2005.
(15) Allen, M. W.; Swartz, C. H.; Myers, T. H.; Veal, T. D.; McConville, C. F.; Durbin, S. M. *Phys. Rev. B* **2010**, *81*, 075211.
(16) Tay, Y. Y.; Tan, T. T.; Liang, M. H.; Boey, F.; Li, S. *Phys. Chem. Chem. Phys.* **2010**, *12*, 6008.
(17) Djurisic, A. B.; Leung, Y. H.; Tam, K. H.; Hsu, Y. F.; Ding, L.; Ge, W. K.; Zhong, Y. C.; Wong, K. S.; Chan, W. K.; Tam, H. L.; Cheah, K. W.; Kwok, W. M.; Phillips, D. L. *Nanotechnology* **2007**, *18*, 095702.
(18) Ozgur, U.; Teke, A.; Liu, C.; Cho, S. J.; Morkoc, H.; Everitt, H. O. *Appl. Phys. Lett.* **2004**, *84*, 3223.
(19) Mehl, B. P.; House, R. L.; Uppal, A.; Reams, A. J.; Zhang, C.; Kirschbrown, J. R.; Papanikolas, J. M. *J. Phys. Chem. A* **2010**, *114*, 1241.
(20) Janotti, A.; Van de Walle, C. G. *Phys. Rev. B* **2007**, *76*, 165202.
(21) McCluskey, M. D.; Jokela, S. J. *J. Appl. Phys.* **2009**, *106*, 071101.
(22) Schmidt-Mende, L.; MacManus-Driscoll, J. L. *Mater. Today* **2007**, *10*, 40.
(23) Williams, F. *Phys. Status Solidi* **1968**, *25*, 493.
(24) Cheng, B.; Shi, W. S.; Russell-Tanner, J. M.; Zhang, L.; Samulski, E. T. *Inorg. Chem.* **2006**, *45*, 1208.
(25) Li, F.; Li, Z.; Jin, F. J. *Mater. Lett.* **2007**, *61*, 1876.
(26) Klingshirn, C. *Semiconductor Optics*, 3rd ed.; Springer-Verlag: Berlin, Germany, 2007.
(27) Cheng, B. C.; Yu, X. M.; Liu, H. J.; Fang, M.; Zhang, L. D. *J. Appl. Phys.* **2009**, *105*, 014311.
(28) Ando, H.; Oohashi, H.; Kanbe, H. *J. Appl. Phys.* **1991**, *70*, 7024.
(29) Takeda, J.; Kurita, S.; Chen, Y. F.; Yao, T. F. *Int. J. Mod. Phys. B* **2001**, *15*, 3669.
(30) Song, J. K.; Willer, U.; Szarko, J. M.; Leone, S. R.; Li, S.; Zhao, Y. *J. Phys. Chem. C* **2008**, *112*, 1679.
(31) Guo, B.; Qiu, Z. R.; Wong, K. S. *Appl. Phys. Lett.* **2003**, *82*, 2290.
(32) Cavaleri, J. J.; Skinner, D. E.; Colombo, D. P.; Bowman, R. M. *J. Chem. Phys.* **1995**, *103*, 5378.
(33) Guo, B.; Ye, Z. Z.; Wong, K. S. *J. Cryst. Growth* **2003**, *253*, 252.
(34) Hong, S. S.; Joo, T.; Park, W. I.; Jun, Y. H.; Yi, G. C. *Appl. Phys. Lett.* **2003**, *83*, 4157.
(35) Johnson, J. C.; Knutsen, K. P.; Yan, H. Q.; Law, M.; Zhang, Y. F.; Yang, P. D.; Saykally, R. J. *Nano Lett.* **2004**, *4*, 197.
(36) Studenikin, S. A.; Cocivera, M. *J. Appl. Phys.* **2002**, *91*, 5060.
(37) Hsu, N. E.; Hung, W. K.; Chen, Y. F. *J. Appl. Phys.* **2004**, *96*, 4671.
(38) Foreman, J. V.; Li, J. Y.; Peng, H. Y.; Choi, S. J.; Everitt, H. O.; Liu, J. *Nano Lett.* **2006**, *6*, 1126.

(39) Li, D.; Leung, Y. H.; Djurisic, A. B.; Liu, Z. T.; Xie, M. H.; Shi, S. L.; Xu, S. J.; Chan, W. K. *Appl. Phys. Lett.* **2004**, *85*, 1601.
(40) Guo, R.; Matsumoto, M.; Matsumoto, T.; Higashihata, M.; Nakamura, D.; Okada, T. *Appl. Surf. Sci.* **2009**, *255*, 9671.
(41) Reshchikov, M. A.; Korotkov, R. Y. *Phys. Rev. B* **2001**, *64*, 115205.
(42) Meyer, B. K.; Alves, H.; Hofmann, D. M.; Kriegseis, W.; Forster, D.; Bertram, F.; Christen, J.; Hoffmann, A.; Strassburg, M.; Dworzak, M.; Haboeck, U.; Rodina, A. V. *Phys. Status Solidi B* **2004**, *241*, 231.
(43) Egelhaaf, H. J.; Oelkrug, D. *J. Cryst. Growth* **1996**, *161*, 190.
(44) Han, J. P.; Mantas, P. Q.; Senos, A. M. R. *J. Eur. Ceram. Soc.* **2002**, *22*, 49.
(45) Schirmer, O. F.; Zwingel, D. *Solid State Commun.* **1970**, *8*, 1559.
(46) Look, D. C.; Hemsky, J. W.; Sizelove, J. R. *Phys. Rev. Lett.* **1999**, *82*, 2552.
(47) Sokol, A. A.; French, S. A.; Bromley, S. T.; Catlow, C. R. A.; van Dam, H. J. J.; Sherwood, P. *Faraday Discuss.* **2007**, *134*, 267.
(48) Kohan, A. F.; Ceder, G.; Morgan, D.; Van de Walle, C. G. *Phys. Rev. B* **2000**, *61*, 15019.
(49) Oba, F.; Nishitani, S. R.; Isotani, S.; Adachi, H.; Tanaka, I. *J. Appl. Phys.* **2001**, *90*, 824.
(50) Vanheusden, K.; Warren, W. L.; Seager, C. H.; Tallant, D. R.; Voigt, J. A.; Gnade, B. E. *J. Appl. Phys.* **1996**, *79*, 7983.
(51) Li, Y.; Meng, G. W.; Zhang, L. D.; Phillipp, F. *Appl. Phys. Lett.* **2000**, *76*, 2011.
(52) Lin, B. X.; Fu, Z. X.; Jia, Y. B. *Appl. Phys. Lett.* **2001**, *79*, 943.
(53) Wu, X. L.; Siu, G. G.; Fu, C. L.; Ong, H. C. *Appl. Phys. Lett.* **2001**, *78*, 2285.
(54) Liu, M.; Kitai, A. H.; Mascher, P. *J. Lumin.* **1992**, *54*, 35.
(55) Lyu, S. C.; Zhang, Y.; Ruh, H.; Lee, H. J.; Shim, H. W.; Suh, E. K.; Lee, C. J. *Chem. Phys. Lett.* **2002**, *363*, 134.
(56) Garces, N. Y.; Wang, L.; Bai, L.; Giles, N. C.; Halliburton, L. E.; Cantwell, G. *Appl. Phys. Lett.* **2002**, *81*, 622.
(57) Cox, R. T.; Block, D.; Herve, A.; Picard, R.; Santier, C.; Helbig, R. *Solid State Commun.* **1978**, *25*, 77.

THE JOURNAL OF PHYSICAL CHEMISTRY C

ARTICLE

pubs.acs.org/JPCC

Characterizing Electron−Hole Plasma Dynamics at Different Points in Individual ZnO Rods

Ralph L. House,[†] Justin R. Kirschbrown,[†] Brian P. Mehl,[†] Michelle M. Gabriel,[†] Joseph A. Puccio,[†] James K. Parker,[†,‡] and John M. Papanikolas*[,†]

[†]Department of Chemistry, Caudill Laboratories, University of North Carolina at Chapel Hill, Chapel Hill, North Carolina 27599, United States

[‡]Chemical Sciences Division, U.S. Army Research Office, P.O. Box 12211, Research Triangle Park, North Carolina 27709, United States

ABSTRACT: We have used two-photon emission microscopy to characterize the charge carrier dynamics at different locations within a single ZnO rod. Photoexcitation by a focused laser produces carriers (electrons and holes) in a localized region. Emission is detected using both time-integrated and time-resolved methods. Results show that the electron−hole plasma (EHP) state plays a larger role at the end of the rod compared to other points within the structure, where electron−hole recombination proceeds through an excitonic state. The origin of this spatial dependence is attributed to the physical confinement at the end of the structure that prevents an expansion of the photoexcited electron−hole cloud through processes such as carrier diffusion. Whispering gallery modes are identified as contributing to a periodic emission pattern along the length of the structure.

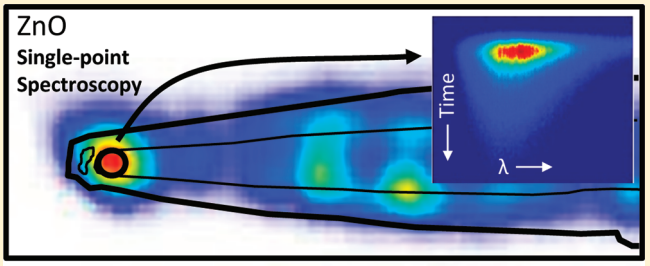

1. INTRODUCTION

At low excitation intensities the optical properties of semiconductors are determined by single electron−hole pairs that exist either in excitonic states or as free carriers in the continuum. As the excitation intensity and corresponding carrier density increase, the separation between excitons becomes comparable to, or smaller than, the Bohr radius. The charge carrier interactions that emerge in this high-density regime give rise to a host of nonlinear optical effects, including a weakening of the exciton binding due to Coulombic screening, and ultimately the formation of a collective electron−hole plasma (EHP) phase. The many-body exchange and correlation interactions that are present in the EHP stabilize the photoexcited state, resulting in a narrowing of the band gap that is often referred to as band gap renormalization.[1] Furthermore, the oscillator strength is enhanced in the EHP, and electron−hole recombination in this high density limit is characterized by an intense, red-shifted emission compared to its excitonic counterpart.[2]

Finite-sized structures offer an additional layer of complexity and opportunity. When an object's dimensions are comparable to the wavelength, its size and shape play a central role in determining its optical properties. The shape of the object can give rise to complex cavity resonances that concentrate the optical field in specific locations, becoming an intrinsic part of the optical response. While most examples of cavity resonances have come from engineered systems, similar effects are possible in nanoscale and mesoscale structures.[3−10]

Electron−hole plasma formation has been observed in bulk materials and single nanostructured objects. However, the potential for EHP variation across different regions within a single structure, and the relation between EHP formation and local optical cavity modes, has not been explored. Here we describe the use of two-photon emission microscopy to examine the spatial variation in EHP formation in individual needle-shaped ZnO rods and relate EHP formation with local optical cavity modes. The combination of facile EHP formation in ZnO[6−9,11,12] and the diverse set of synthetically available crystalline structures with complex geometrical architectures[13−15] make this an ideal material for investigating shape dependent EHP formation. Previous work in our lab investigated the excited state dynamics of needle-shaped ZnO rods with spatial specificity.[16−19] This report builds upon that work by examining the EHP dynamics in different regions of individual rods (e.g., end vs middle) using both time-integrated and time-resolved methods. Experiments using a focused laser beam to excite a spatially localized region of the rod show a greater propensity for EHP formation in the narrow tips compared to the interior regions where the rod's cross section is larger. We attribute this spatial variation to a physical confinement of carriers that inhibits expansion of the charge cloud at the end the structure, maintaining the density of electron−hole pairs and the EHP state. In addition to the spatial variation in EHP formation, the optical properties are strongly influenced by whispering gallery (WG) modes supported within the rod's hexagonal cross section. It is the combination of spatially varying EHP and optical cavity modes that give rise

Received: August 15, 2011
Revised: September 21, 2011
Published: September 22, 2011

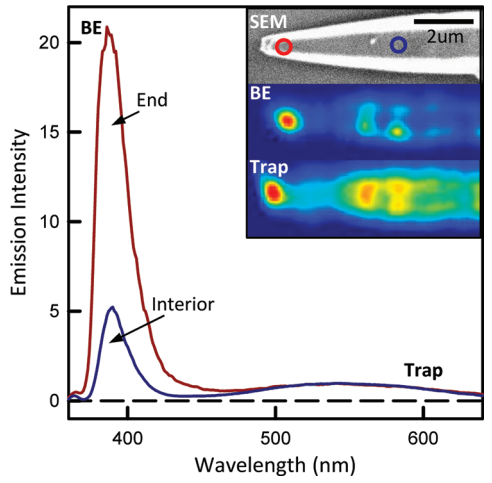

Figure 1. Band-edge (BE) and trap (T) emission images of the rod shown in the SEM image. The rods are needle-shaped and symmetric, although in this image only the left-hand side of the structure is shown. The fluorescence images were obtained at a laser power of 10 mW and show increased intensity at the end of the rod and modulated intensity throughout the interior. Emission spectra collected by positioning the excitation spot at the end (red) and interior (blue) of the structure show two bands arising from band-edge emission (BE) at 400 nm and trap recombination at 550 nm. The locations of the spectra are indicated by the colored circles in the SEM image.

to the complex emission images and spatially heterogeneous behavior.

2. EXPERIMENTAL SECTION

Studying the carrier dynamics at different points within a single structure necessitates a technique with high temporal resolution and spatially localized excitation. The microscope used here combines an ultrafast laser source with a home-built inverted microscope.[18] Two photon excitation is achieved using the 730 nm output of a mode-locked (80 MHz) Ti:sapphire laser. Light from the laser is directed through a prism-pair compressor and reflected off a dichroic beam splitter (R, 680−1000 nm; T, 360−650 nm) onto the back aperture of the objective (Olympus MSPlan 50×, 0.8 NA), which focuses the beam to a diffraction limited spot. Because two-photon excitation scales with the square of the laser intensity, the lateral dimension of the excitation is approximately 350 nm. Photoluminescence collected by the objective passes through the beam splitter and is directed into a monochromator and detected by a photomultiplier tube for time integrated measurements or a streak camera for time-resolved detection (∼10 ps time resolution). Imaging is achieved by raster-scanning the sample across the focal point of the objective using a piezoelectric stage (Queensgate NPS3330 Controller/Stage System).

The structures were synthesized using hydrothermal techniques, drop-cast onto a glass microscope slide, and annealed at 550 °C prior to study. Through the course of this study we examined approximately 10 needle-shaped rods. The scanning electron microscopy (SEM) image of a typical structure is shown in the top right of Figure 1. While there is some variation in size, the structures are all crystalline, with faceted, hexagonal cross sections. They generally vary between 10 and 20 μm in length and are 1−2 μm in diameter at the middle, tapering down to ∼300−500 nm at the ends.

3. RESULTS AND DISCUSSION

Zinc oxide is a wide band gap semiconductor (3.37 eV) with a strong exciton binding energy (60 meV).[13,15] Photoexcitation in the ultraviolet, or two-photon excitation in the near-infrared, promotes electrons from the valence band to the conduction band. The free carriers that are produced can relax into excitons (at low excitation intensities), resulting in a near-UV emission at 390 nm, or become trapped at defect sites, giving rise to a broad visible emission centered at 550 nm.

Imaging. Two-photon microscopy images obtained by monitoring the band edge (390 nm) and trap (550 nm) emission channels following two-photon excitation at 730 nm of a typical rod (denoted **R1**) are shown along with the SEM image in Figure 1. The increased areas of intensity at the ends of the structure are a particularly prominent feature in both the band-edge and trap emission images. A closer comparison of the two images, however, shows that the bright spots are slightly offset, with the trap image showing its most intense emission slightly to the left of the band edge. This shift is likely a consequence of the roughness observed at the tip of this rod, which would result in a greater defect density and brighter trap emission.

Optical Cavity Modes. In addition to the bright ends, the emission from the interior of the rod is periodically modulated and appears to coincide with the facets in both the trap and band-edge emission images, with greater contrast in the band edge. Not every rod exhibits a pattern of this nature, but most do, and the contrast in the band-edge image is generally always greater. This spatial variation most likely results from the influence of optical cavity modes (supported by the rod's hexagonal cross section) on the emission intensity. Generally, there are two types of modes—standing wave (Fabry−Perot, FP) resonances, which are supported between two parallel facets, and whispering gallery (WG) modes, which correspond to propagation of light around the periphery of the hexagonal cross section through total internal reflection off each facet. We previously identified the influence of FP and WG modes on second-harmonic generation in ZnO rods,[17] and WG modes have been implicated in a number of other spectroscopic measurements of ZnO structures.[20−25] The coincidence of the bright spots in the emission images with the vertices of the hexagonal facets suggests that it is the WG modes that influence photoluminescence in these structures.

For a given wavelength, λ, the resonance condition dictates that modes will be supported for specific cross-sectional diameters of the rod, i.e.

$$d_m = \frac{\lambda}{3n}\left[m + \frac{6}{\pi}\tan^{-1}(\beta\sqrt{3n^2-4})\right] \quad (1)$$

where d_m is the separation between two parallel facets and m is an integer that specifies the mode number.[22,26] In this expression n is the refractive index and β depends upon the polarization of the light. The spacing between adjacent modes, $\Delta d = d_{m+1} - d_m$ is then $\lambda/3n$.

The periodic nature of the emission pattern in the tapered structure arises because the facet spacing changes along the length of the rod.[17] Analysis of the SEM images for this rod shows that the facet separation varies nearly linearly with distance along the rod, resulting in a series of resonances observed along the structure that are spaced by

$$\Delta L = \frac{\Delta d}{\alpha} = \frac{\lambda}{3n\alpha} \quad (2)$$

where α is the change in the facet spacing per unit length along the rod. For the rod shown in Figure 1, α = 120 nm/μm in the vicinity of the resonances.

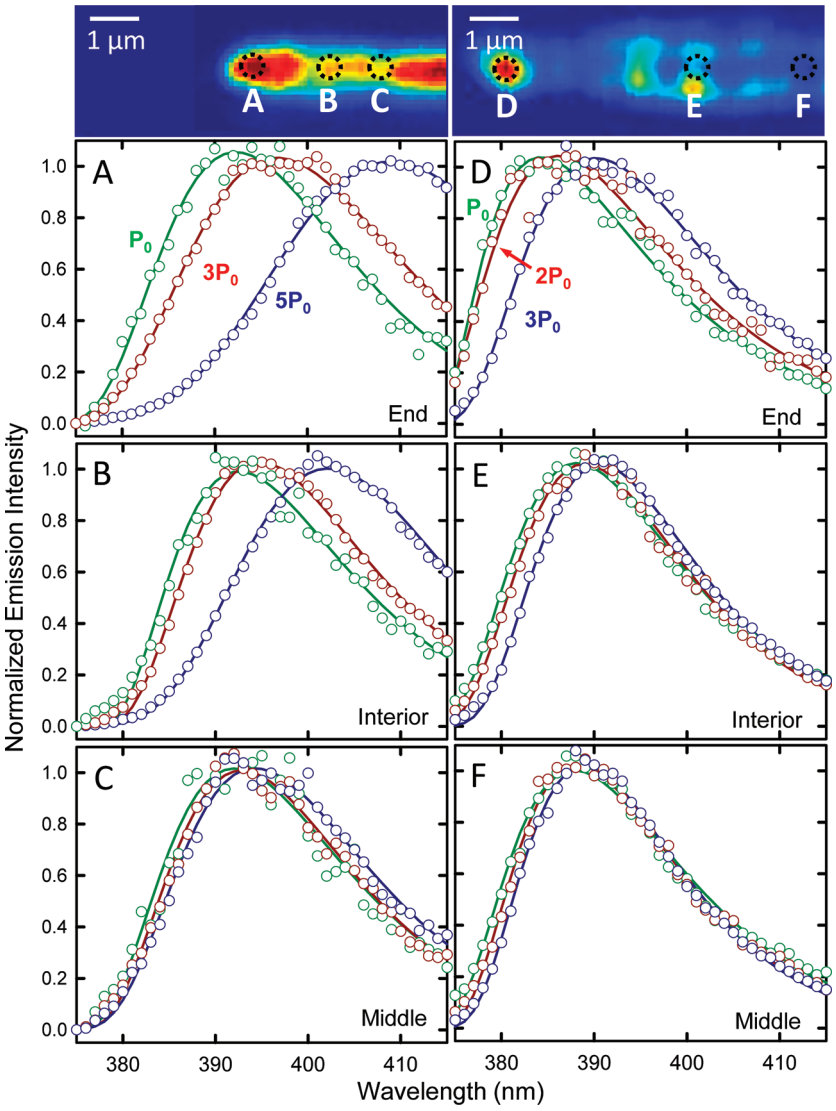

Figure 2. Band-edge emission spectra collected at a series of laser powers at three different points within two different structures, **R1** and **R2**. Emission images for the two structures are shown at the top. Panels A−C and the left-hand image correspond to **R2**; panels D−F and right-hand image correspond to **R1**. The scale bar in both images is 1 μm. The locations marked A−F indicate the points at which the spectra shown in panels A−F were collected. Each panel shows three spectra collected using low (green), intermediate (red), and high (blue) laser power. The green spectra in panels A−C were collected at the same power (P_0), as were the red ($3P_0$) and blue ($5P_0$). The same is true for panels D−F, but green, red, and blue correspond to P_0, $2P_0$, and $3P_0$. In both cases, P_0 = 5 mW.

The WG modes can influence the emission either through spatial modulation of the excitation or enhancement of the photoluminescence through constructive interference. Using λ = 730 nm and n = 2 in the above expression yields a predicted spacing, ΔL, between optical resonances of approximately 0.9−1.0 μm, which is close to the observed spacing of 1.0−1.1 μm. This suggests that the periodic variation observed in the emission images arises (at least in part) from excitation light coupling into the WG modes, resulting in a concentration of the optical field at specific locations within the rod and regions of localized excitation. In addition to the excitation light, a coupling of the 390 nm emission into the WG resonator may also play a role. While the predicted spacing for adjacent resonances (m, m + 1) in the band-edge emission (390 nm) is only 0.5 μm, too small to account for the observed pattern, the spacing between alternating resonances (m, m + 2) would also be around 1.0 μm. Thus, the periodic pattern observed in the band-edge emission image may stem from a situation in which *both* the excitation and emission light are quasi-resonant. This double resonance condition is not expected to be present in the trap image, where the resonance condition cannot be simultaneously satisfied by the 730 nm excitation light and the 550 nm defect emission, accounting for the lesser degree of contrast observed in the defect emission image.

Spatially Dependent EHP Formation. Spectroscopic measurements are performed by positioning the excitation spot at specific points in the structure. The photoluminescence spectra shown in Figure 1B were collected from the end of the rod and at a point located between the end and middle, denoted interior. (Note, throughout this manuscript the "end of the rod" refers to the location of the bright point in the band-edge emission image.) Emission spectra observed at different locations have

the same spectral features, namely a narrow transition centered at ~390 nm that corresponds to electron−hole recombination from the band-edge (BE) and a broad trap emission band at ~550 nm (T). While the spectra have the same basic form, the intensity of the band-edge emission relative to the trap depends on the position in the structure, with the spectrum obtained from the end exhibiting a greater BE/T intensity ratio than the interior (~20:1 vs ~5:1). The spatial variation in the BE/T ratio is one indicator that the photophysics at the end of the structure differ markedly from those in the interior.

The band-edge emission spectrum at the end of the rod also shows a significant dependence on excitation intensity relative to other points. Band-edge emission spectra collected at different excitation intensities are shown in Figure 2 for three different locations in two different rods, **R1** and **R2**. Dashed circles on two-photon emission images that accompany each set of spectra indicate the locations where the spectra were collected. At the middle of the rod, the spectra are independent of excitation intensity, with $\lambda_{max} \approx 390$ nm. On the other hand, at the end of the rod, the spectra systematically shift to lower energy with increasing excitation energy. In the case of **R2**, a broadening of the spectrum is also observed; however, the degree to which this happens varies from rod to rod. Similar, but less dramatic changes, are observed in the interior. We have observed this phenomenon to differing degrees in multiple structures. A systematic examination of nine rods shows that on average there is an 8 nm shift at the end, a 4 nm shift in the interior, and a 2 nm shift in the middle of the structure.

The red shift in the emission band is consistent with the formation of an EHP at higher excitation intensities.[8−10,27] At low excitation intensity the band-edge (BE) emission arises predominantly from exciton recombination. As the carrier density increases, Coulombic screening weakens the exciton binding energy, resulting in dissociation of the electron−hole pairs and the transition to the EHP state. Experimental gain spectra suggest the transition to the EHP in ZnO occurs at carrier densities between 10^{17} and 10^{19} cm^{-3}.[1] On the basis of the two-photon cross section for ZnO and excitation intensities used here, we estimate that each laser pulse produces a charge carrier density of $\approx 10^{21}$ cm^{-3}.[28]

The many-body correlation and exchange interactions between carriers that are present in the high density EHP regime alter the electronic structure of the semiconductor. Because the Pauli principle forbids electrons with parallel spin to occupy the same unit cell, the distance between electrons increases, reducing the Coulombic repulsion. There is also a greater probability of finding an electron near a hole (and vice versa) than finding two like charges in the same vicinity, and the two effects combined lower the total energy of the system.[1] The net result of this stabilization of the plasma is a monotonic decrease of the band gap with increasing electron−hole pair density. As a consequence, the emission spectrum resembles the exciton emission at low laser power but shifts to the red as the excitation intensity increases and the system transitions to an EHP state.

Closer inspection of the spectra shows that at the lowest excitation intensity the spectra at the end of the structure exhibit some differences relative to their counterparts in the interior. The **R1** spectrum is slightly blue-shifted and the **R2** spectrum is broadened. While the broadening is suggestive of the beginnings of plasma formation, the blue shift is consistent with the weakening of the exciton that occurs as their Bohr orbits begin to overlap.[1] These differences indicate that the photophysics at the end of the structure are influenced by carrier−carrier interactions, even at the lowest excitation intensities.

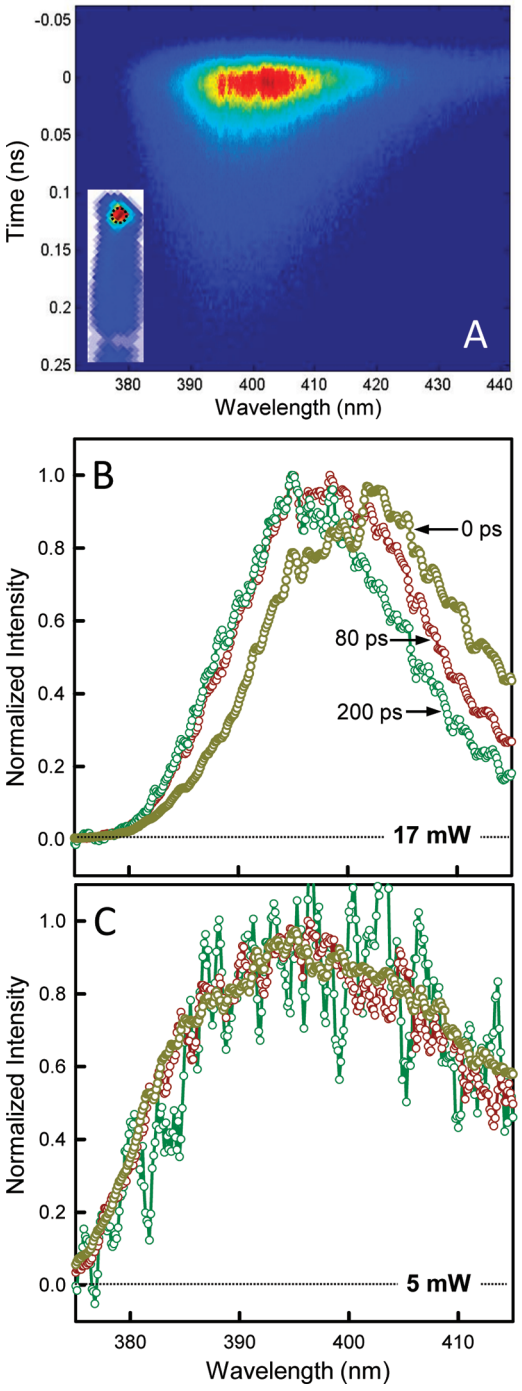

Figure 3. Time-resolved emission data collected from the end of structure **R3**. (A) Intensity map depicting emission as a function of time and wavelength (blue corresponds to low intensity, red high intensity) obtained under high laser power conditions (17 mW). The inset shows the emission image. (B) Emission spectra obtained by taking horizontal slices through this emission map at 0 ps (gold), 80 ps (red), and 200 ps (green) after excitation show a time-dependent blue shift of the band. (C) Emission spectra collected from the same point, but at a lower laser power (5 mW), show no shift.

The dependence of the spectrum on carrier density implies that the EHP emission should have a distinct temporal signature,

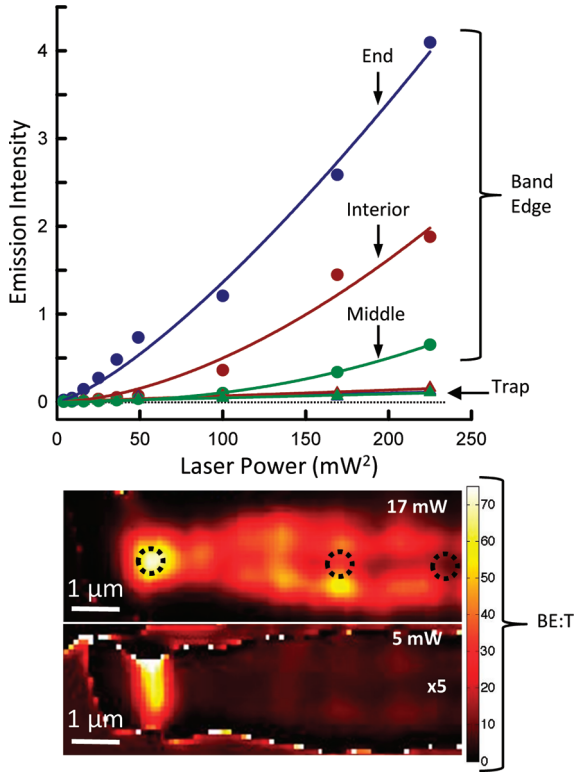

Figure 4. Intensities of the band-edge and trap emission bands in **R1** as a function of laser power at the end (blue), interior (red), and middle (green). The three locations are indicated by the points labeled D, E, and F, respectively, in the right-hand image of Figure 2. Images represent the BE/T ratios obtained by dividing the band-edge image by the trap image at two different laser powers. The 5 mW image was multiplied by a factor of 5.

showing an emission spectrum that appears initially to the red of the exciton band and shifts to the blue with time as electrons and holes recombine and the carrier density drops. The spectral–temporal intensity map in Figure 3A depicts the evolution of the BE emission following 17 mW excitation at the end of the rod labeled **R3**. The fluorescence image of this rod is shown in the inset of Figure 3A. Spectra at specific times can be obtained by taking horizontal slices across the intensity map. A comparison of spectra extracted at 0, 80, and 200 ps shows that the spectra shift to higher energy over the first 200 ps following photoexcitation (Figure 3B), consistent with the instantaneous appearance of an EHP and a subsequent transition to an excitonic state. When the experiment is conducted in the same region of the rod with a lower power (5 mW), the shift in the spectrum disappears (Figure 3C), in line with the formation of an excitonic state.

In the smaller regions at the ends of the structure, we observe an increase in the magnitude of the spectral red shift (Figure 2), consistent with the formation of an EHP. The implication is that the photogenerated carriers in these locations must have a density that is high enough to support transition of the nascent charge distribution to the EHP. This is greatly facilitated at the end of the structure, where physical confinement of the charge carriers will help to maintain the close interaction. In the middle of the structure, carriers can migrate away from the excitation region, either through simple diffusion or perhaps driven by internal fields that separate the electrons and holes. On the basis of the carrier diffusion constant in ZnO ($\sim$10 cm^2 s^{-1}),[29,30] we estimate a field-free diffusion length of $\approx$300 nm during the first 100 ps after excitation. Band-bending in ZnO is anticipated to result in electric fields and a depletion zone that extends a hundred nanometers or more into the bulk, which could increase this even further. The net result is a decrease in the charge density that makes it more difficult to form and sustain the EHP. As a result, the emission observed at the interior locations arises predominantly from excitonic recombination.

The transition from the excitonic state to the EHP is also accompanied by characteristic changes in the emission intensity. A decrease in the oscillator strength of the exciton emission is expected as the carrier density increases. In this intermediate regime, the exciton–exciton interactions result in a weakening of the exciton binding energy that is accompanied by an increase in the excitonic radius and a corresponding decrease in the overlap of the electron and hole wave functions. This trend reverses as the system transitions from this intermediate regime to the EHP, where an increased correlation between the electrons and holes results in a greater oscillator strength (i.e., excitonic enhancement) and a brighter emission than those of its exciton counterpart.[2] This increase in oscillator strength could explain the more intense band-edge emission observed both in the images and in the spectra collected at the ends of the structure.

Shown in Figure 4 is the intensity of the band-edge and trap emission as a function of the square of the laser power at three different points located along the central axis of **R1**. The trap emission exhibits a linear increase in this representation, indicating that it is simply proportional to the carrier density produced by two-photon excitation. The band-edge emission, on the other hand, shows upward curvature, signifying that its intensity increases superlinearly with the carrier density. This upward curvature is more pronounced at the end of the rod, where the red shift in the emission spectrum shows the contribution from the EHP is the greatest. The intensity dependence of the BE emission (both its intensity and spectral position) indicates a spatially dependent propensity for EHP formation, with the degree of correlation and exchange interactions increasing (i.e., greater degree of EHP) as the excitation is moved from the middle to the end of the rod.

Whispering Gallery Mode Stimulated Emission. One signature of stimulated emission in ZnO is an increase in the ratio of the band-edge to trap emission intensities with increasing laser power. Shown below the plot in Figure 4 are images of the BE/T ratio at two different laser powers. At low laser powers there is a generally uniform BE/T ratio of $\approx$2 observed throughout the interior of this rod and a localized region of $\approx$12–13 at the end. Given the small excitation volume at this location, we anticipate that spontaneous EHP emission is the main contributor to the total emission and that the increase in the BE/T ratio is due primarily to the EHP oscillator strength. However, because of its large oscillator strength, EHP emission in ZnO is often associated with stimulated emission and lasing in finite sized structures,[7–9,11,12,25,31–35] and as a result it is difficult based on our data alone to rule out contributions from stimulated emission at the end of the rod. It is interesting to note that the BE/T ratio is $\approx$0.5–0.7 at the very tip of the rod, where the most intense spot in the trap emission image occurs, highlighting the greater influence of the trap emission where the structure terminates. Our focus, however, is not on the end of the structure but on the changes that occur in the interior.

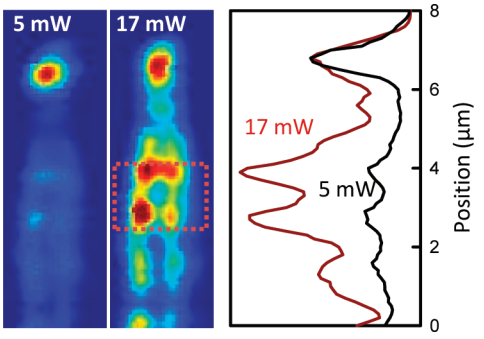

Figure 5. Band-edge emission images of **R1** obtained under low power (5 mW) and high power (17 mW) conditions. The images are scaled to have the same intensity at the end of the rod. The images are 8 μm in the vertical dimension. The right-hand panel shows the emission intensity (obtained by summing the intensity across a row of pixels) along the longitudinal axis of the rod for the two different powers. The WG mode pattern becomes more pronounced at higher powers.

In the rod's interior, the BE/T ratio grows by a factor of 30−40 as the laser power is increased from 5 to 17 mW; however, the growth is not uniform across the structure. The WG mode pattern is more pronounced in the BE/T ratio image at the higher power, indicating that resonance locations exhibit a disproportionate increase in the band-edge emission intensity. This is evident in the band-edge images themselves, which are shown at low and high excitation intensities in Figure 5. The emission intensity along the length of the rod is displayed in the right-hand panel, which shows the integrated signal across a row of pixels as a function of longitudinal position. As the laser power is increased, the brightness of the interior WG modes exceeds even that observed at the end of the rod.

These observations must arise from a situation in which the rod's cross-sectional diameter also supports a WG resonance at 390 nm. Under these circumstances, emission (exciton or EHP) from the excitation region would travel around the periphery of the rod undergoing total-internal reflection at each facet, resulting in stimulated emission. Because we do not see a narrowing of the emission spectrum (Figure 2D−F), which would be an indicator of WG mode lasing, the enhancement of the mode pattern observed here is probably better described by amplified spontaneous emission.

Closer inspection of the images shows that, for a given WG mode, the emission intensity depends upon the lateral position of the excitation. Figure 6 shows this variation for one of the WG resonances in **R1**, where the expanded view in the figure corresponds to the area indicated by the red rectangle in Figure 5. The intensity profile across the rod (right-hand side of panel) shows two peaks that coincide with the outer facets of the structure. Comparison of lateral profiles taken at different powers shows that the contrast depends upon laser intensity, with the peaks increasing more than the interior. Intensity dependence measurements performed at the "bright" and "dim" spots marked on the image are displayed in Figure 6B. The brighter spot shows a steeper increase in the emission intensity with increasing pulse energy.

The lateral variation in the intensity dependence is indicative of a nonlinear optical effect, either in the degree of excitation or in the enhancement of the stimulated emission. One possibility is that the WG mode results in an enhancement in the optical field, which in turn leads to a greater carrier density and a more intense

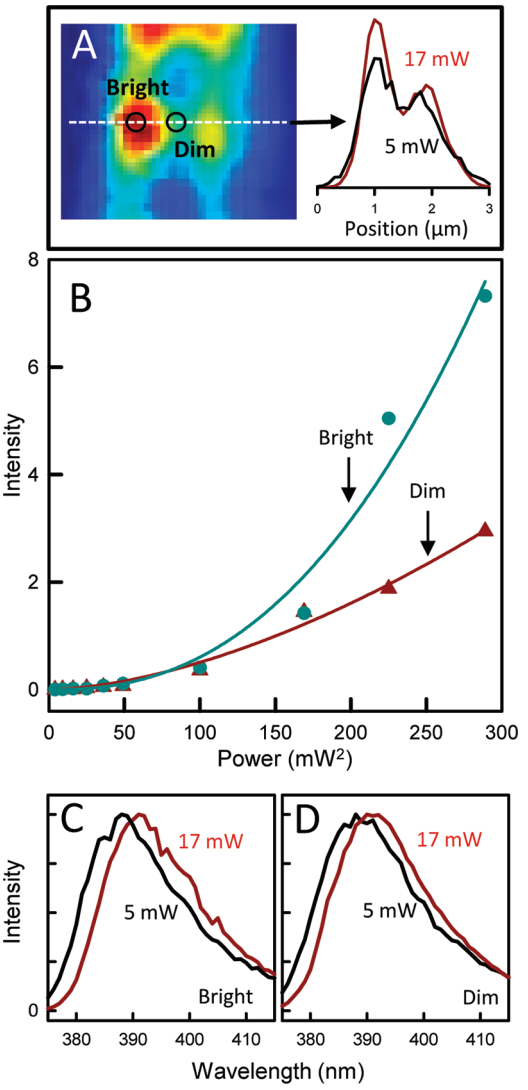

Figure 6. (A) Expanded image of the WG mode in **R1** indicated by the red rectangle in Figure 5. The horizontal dimension of the image is 3 μm. The profile at the right corresponds to a horizontal cut along the dotted line in the image for both the low (5 mW) and high (17 mW) power cases. (B) The intensities of the band-edge emission at the two points along this line that are labeled "bright" and "dim" in the image. Parts C and D are the band-edge emission spectra collected from these two points at low (5 mW) and high (17 mW) power.

EHP. This does not appear to be the case, however, as the two locations (Figure 6C and D) show similar power-dependent spectral shifts, implying similar EHP characteristics. A more likely possibility for its origin lies in the positional differences of the excitation. When the rod is excited near its edge, light emitted by the electron−hole recombination event will be better positioned to undergo total internal reflection and travel around the periphery of the rod, stimulating emission on each successive round trip. The splitting of the WG resonance into two spots may be a consequence of a better coupling of the emission into the WG mode at those locations.

4. CONCLUSIONS

We have implemented two-photon emission microscopy to locally excite different regions of individual ZnO rods at steadily

dx.doi.org/10.1021/jp207830h |J. Phys. Chem. C 2011, 115, 21436–21442

increasing excitation intensities. Results from steady-state spectral analyses show that the BE emission band shifts to lower energy with increasing excitation power at the end of the rod. The magnitude of the shift is greatly diminished in the rod interior (by a factor of 2 on average) and disappears almost completely in the middle. These observations are consistent with the preferential formation of an EHP at the end of the rod. Time-resolved emission data confirms this notion, showing a time-dependent spectral blue shift in the band edge emission when the end of the rod is excited with high power. This corresponds to disappearance of the EHP and subsequent recovery of the band gap. No shift is observed at low excitation intensities. Images obtained under high power conditions show a pronounced whispering gallery (WG) mode pattern that enhances the stimulated emission. Collectively, our results show that different regions of a single structure can exhibit distinctly different photophysical behaviors.

AUTHOR INFORMATION

Corresponding Author
*E-mail: john_papanikolas@unc.edu.

ACKNOWLEDGMENT

Support for R.L.H., J.R.K., and B.P.M. was provided by a grant from the National Science Foundation (CHE-0809045). Support for M.M.G. during the latter stages of the project was provided by a grant from the U.S. Army Research Laboratory and the U.S. Army Research Office under Contract Number W911NF-04-D-0004. The project also made use of instrumentation purchased by the UNC-EFRC on Solar Fuels and Next Generation Photovoltaics, an Energy Frontier Research Center funded by the U.S. Department of Energy, Office of Science, Office of Basic Energy Sciences under Award Number DE-SC0001011.

REFERENCES

(1) Klingshirn, C. F. *Semiconductor optics*, 3rd ed.; Springer: Berlin, New York, 2007.
(2) Pavesi, L.; Staehli, J. L.; Capozzi, V. *Solid State Commun.* **1987**, *61*, 321.
(3) Voss, T.; Svacha, G. T.; Mazur, E.; Muller, S.; Ronning, C.; Konjhodzic, D.; Marlow, F. *Nano Lett.* **2007**, *7*, 3675.
(4) Sun, L. X.; Chen, Z. H.; Ren, Q. J.; Yu, K.; Bai, L. H.; Zhou, W. H.; Xiong, H.; Zhu, Z. Q.; Shen, X. C. *Phys. Rev. Lett.* **2008**, *100*, 156403.
(5) van Vugt, L. K.; Ruhle, S.; Ravindran, P.; Gerritsen, H. C.; Kuipers, L.; Vanmaekelbergh, D. *Phys. Rev. Lett.* **2006**, *97*, 147401.
(6) Johnson, J. C.; Yan, H. Q.; Schaller, R. D.; Petersen, P. B.; Yang, P. D.; Saykally, R. J. *Nano Lett.* **2002**, *2*, 279.
(7) Song, J. K.; Willer, U.; Szarko, J. M.; Leone, S. R.; Li, S.; Zhao, Y. *J. Phys. Chem. C* **2008**, *112*, 1679.
(8) Leung, Y. H.; Kwok, W. M.; Djurisic, A. B.; Phillips, D. L.; Chan, W. K. *Nanotechnology* **2005**, *16*, 579.
(9) Takeda, J.; Kurita, S.; Chen, Y. F.; Yao, T. F. *Int. J. Mod. Phys. B* **2001**, *15*, 3669.
(10) Zu, P.; Tang, Z. K.; Wong, G. K. L.; Kawasaki, M.; Ohtomo, A.; Koinuma, H.; Segawa, Y. *Solid State Commun.* **1997**, *103*, 459.
(11) Song, J. K.; Szarko, J. M.; Leone, S. R.; Li, S. H.; Zhao, Y. P. *J. Phys. Chem. B* **2005**, *109*, 15749.
(12) Szarko, J. M.; Song, J. K.; Blackledge, C. W.; Swart, I.; Leone, S. R.; Li, S. H.; Zhao, Y. P. *Chem. Phys. Lett.* **2005**, *404*, 171.
(13) Djurisic, A. B.; Leung, Y. H. *Small* **2006**, *2*, 944.
(14) Wang, Z. L. *J. Phys.: Condens. Matter* **2004**, *16*, R829.
(15) Ozgur, U.; Alivov, Y. I.; Liu, C.; Teke, A.; Reshchikov, M. A.; Dogan, S.; Avrutin, V.; Cho, S. J.; Morkoc, H. *J. Appl. Phys.* **2005**, *98*, 041301.
(16) Mehl, B. P.; Kirschbrown, J. R.; House, R. L.; Papanikolas, J. M. *J. Phys. Chem. Lett.* **2011**, *2*, 1777.
(17) Mehl, B. P.; House, R. L.; Uppal, A.; Reams, A. J.; Zhang, C.; Kirschbrown, J. R.; Papanikolas, J. M. *J. Phys. Chem. A* **2010**, *114*, 1241.
(18) House, R. L.; Mehl, B. P.; Kirschbrown, J. R.; Barnes, S. C.; Papanikolas, J. M. *J. Phys. Chem. C* **2011**, *115*, 10806.
(19) House, R. L.; Mehl, B. P.; Zhang, C.; Kirschbrown, J. R.; Barnes, S. C.; Papanikolas, J. M. *Proc. SPIE* **2009**, *7396*, 73960G.
(20) Liu, J. Z.; Lee, S.; Ahn, Y. H.; Park, J. Y.; Koh, K. H.; Park, K. H. *Appl. Phys. Lett.* **2008**, *92*, 263102.
(21) Nobis, T.; Grundmann, M. *Phys. Rev. A* **2005**, *72*, 063806.
(22) Nobis, T.; Kaidashev, E. M.; Rahm, A.; Lorenz, M.; Grundmann, M. *Phys. Rev. Lett.* **2004**, *93*, 103903.
(23) Czekalla, C.; Sturm, C.; Schmidt-Grund, R.; Cao, B. Q.; Lorenz, M.; Grundmann, M. *Appl. Phys. Lett.* **2008**, *92*, 241102.
(24) Zhang, Y.; Zhou, H. J.; Liu, S. W.; Tian, Z. R.; Xiao, M. *Nano Lett.* **2009**, *9*, 2109.
(25) Dai, J.; Xu, C. X.; Wu, P.; Guo, J. Y.; Li, Z. H.; Shi, Z. L. *Appl. Phys. Lett.* 2010, *97*, 011101.
(26) Grundmann, M.; Czekalla, C.; Nobis, T.; Rahm, A.; Cao, B. Q.; Zuniga-Perez, J.; Sturm, C.; Schmidt-Grund, R.; Lorenz, M. *Phys. Status Solidi B* **2010**, *247*, 1282.
(27) Cheng, B. C.; Yu, X. M.; Liu, H. J.; Fang, M.; Zhang, L. D. *J. Appl. Phys.* 2009, *105*, 014311.
(28) Lin, J. H.; Chen, Y. J.; Lin, H. Y.; Hsieh, W. F. *J. Appl. Phys.* **2005**, *97*, 033526.
(29) Mitsubori, S.; Katayama, I.; Lee, S. H.; Yao, T.; Takeda, J. *J. Phys.: Condens. Matter* 2009, *21*, 064211.
(30) Takeda, J.; Takagi, K.; Okabe, T.; Ko, H. J.; Yao, T. *Phys. Status Solidi* **2004**, *1*, 678.
(31) Johnson, J. C.; Yan, H. Q.; Yang, P. D.; Saykally, R. J. *J. Phys. Chem. B* **2003**, *107*, 8816.
(32) Yang, P. D.; Gargas, D. J.; Moore, M. C.; Ni, A.; Chang, S. W.; Zhang, Z. Y.; Chuang, S. L. *ACS Nano* **2010**, *4*, 3270.
(33) Kalt, H.; Fallert, J.; Dietz, R. J. B.; Sartor, J.; Schneider, D.; Klingshirn, C. *Phys. Status Solidi B* **2010**, *247*, 1448.
(34) Anastasiadis, S. H.; Stassinopoulos, A.; Das, R. N.; Giannelis, E. P.; Anglos, D. *J. Opt. (Bristol, U. K.)* 2010, *12*, 024006.
(35) Shih, T.; Mazur, E.; Richters, J. P.; Gutowski, J.; Voss, T. *J. Appl. Phys.* 2011, *109*, 043504.

Direct Imaging of Optical Cavity Modes in ZnO Rods Using Second Harmonic Generation Microscopy†

Brian P. Mehl, Ralph L. House, Abhineet Uppal, Amanda J. Reams, Chuan Zhang, Justin R. Kirschbrown, and John M. Papanikolas*

Department of Chemistry, Caudill Laboratories, University of North Carolina at Chapel Hill, Chapel Hill, North Carolina 27599

Received: February 2, 2009; Revised Manuscript Received: June 11, 2009

Images of second harmonic generation (SHG) in needle-shaped ZnO rods obtained from individual structures show areas of enhanced second harmonic intensity along the longitudinal axis of the rod that are periodically distributed and symmetrically situated relative to the rod midpoint. The spatial modulation is a direct consequence of the fundamental optical field coupling into standing wave resonator modes of the ZnO structure, leading to an enhanced backscattered second harmonic condition that cannot be achieved in bulk ZnO. A more complicated second harmonic image is observed when excitation is below the band gap, which is attributed to whispering gallery modes. This physical phenomenon, which extends beyond just ZnO to many other optical materials, could pave the way to new applications that exploit the nonlinear optical properties of individual structures.

I. Introduction

The increasing demand for miniature optoelectronic and photonic devices that access new spectral regions has fueled intense interest in a variety of wide band gap semiconductors that assume complex geometrical architectures.[1,2] Exciton emission is ideal for many applications but restricts operating wavelengths, limiting device applications. Second harmonic generation (SHG) and other nonlinear mixing processes have the potential to circumvent this limitation. Efficient SHG requires a large second-order susceptibility ($\chi^{(2)}$) and a mechanism to maintain phase coherence between the fundamental and second harmonic optical waves, i.e., phase matching. In many common bulk SHG materials, with large $\chi^{(2)}$ values, phase-matching is achieved by exploiting an intrinsic birefringence. However, the formation of these materials into nanostructures is limited.[3] On the other hand, there are many semiconductors that have large $\chi^{(2)}$ values and can also adopt intricate forms, but they often lack the capacity to achieve phase matching through conventional means.[4,5]

Cavity modes in microstructured materials can play an important role in the nonlinear mixing processes, resulting in new phenomena not present in macroscopic systems. For example, microresonators formed from second-order materials can circumvent phase matching and exhibit efficient SHG when the fundamental and/or second harmonic optical fields are resonant with cavity eigenmodes.[4−12] Experimental observations of this phenomenon date back to the 1960s when Ashkin et al.[6] explored the enhancement of SHG in KDP though optical cavity resonance. More recent efforts used electrochemical, photolithographic, and molecular beam epitaxy techniques to develop complex high-finesse cavities in order to achieve a quasi-phase-matching condition with increased conversion efficiency. In addition to efficiency enhancement, microcavity resonances can result in phase matching conditions that yield second harmonic intensity propagating in new directions. The second harmonic produced in conventional frequency doubling emerges collinear with the fundamental, in the forward scattered direction; however, microcavities can produce a counterpropagating beam as well. This backscattered radiation, which could be thought of as arising from a standing polarization wave, cannot be achieved in bulk materials and is one signature of the optical cavity's influence on the SHG process. While most examples of cavity effects in nonlinear mixing have come from engineered systems, similar effects should be visible in nanoscale structures that have well-defined cavity eigenmodes. Here the shape of the object (e.g., rods, ribbons, tetrapods, etc.) can lead to more complex cavity modes and is expected to play an even greater role in the nonlinear mixing process.

Zinc oxide has emerged as an ideal material for exploring structurally dependent optical phenomena.[13] The diverse set of synthetically available crystalline structures that include wires, rods, and tetrapods provide an array of complex geometrical architectures to investigate.[14] Its wide band gap (3.37 eV, 368 nm) and strong exciton binding energy (60 meV)[15] lead to an intense violet-blue emission under UV excitation that is targeted for many next generation optical device applications. When an object's dimensions are comparable to the wavelength, its size and shape play a central role in determining its optical properties. The hexagonal cross section of the ZnO structure can support both Fabry−Pérot (i.e., standing wave) and whispering gallery modes, and several groups have studied the affects of these optical resonator modes on the ZnO photoluminescence.[16−21] Optical waveguiding and photon confinement are observed in a variety of structures, resulting in modulated spectral properties. These processes, which are integral to the function of many devices including nanowire lasers,[22] are present even when the transverse dimension is smaller than the emission wavelength. While cavity effects on the emission properties of nanostructured materials have been studied, their influence on second-order nonlinear optical processes has remained largely unexplored.

This paper examines the effect of cavity modes on the SHG process in individual needle-like ZnO rods using second harmonic microscopy. The images show areas of cavity-

† Part of the "W. Carl Lineberger Festschrift".

* Corresponding author, john_papanikolas@unc.edu.

10.1021/jp9009614
Published on Web 07/09/2009

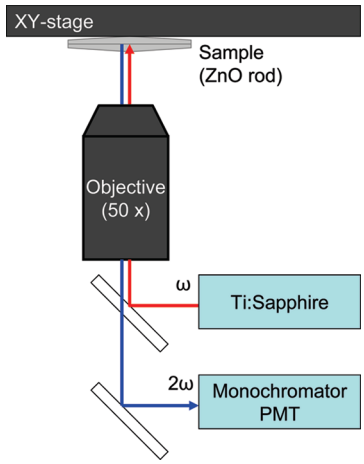

Figure 1. Schematic representation of the nonlinear microscope. Individual rods are excited by a femtosecond laser pulse from a mode-locked Ti:sapphire laser that is focused to a diffraction limited spot by a microscope objective placed below the sample plane. Two-photon photoluminescence and second harmonic light emanating from the rod is collected by the objective, transmitted through a dichroic beamsplitter, focused onto the entrance slit of a monochromator and detected by a photomultiplier tube. Imaging is achieved by raster scanning the sample across the focal point of the objective.

enhanced second harmonic intensity along the longitudinal axis (*c*-axis) of the rod that are periodically distributed, symmetrically situated relative to the rod midpoint, and have positions that vary with the fundamental frequency. The spatial modulation is a direct consequence of the fundamental (ω) coupling into cavity modes of the ZnO resonator that are oriented transverse to the rod axis, resulting in enhanced backscattered second harmonic light. Second harmonic generation in bulk materials propagates in a forward direction due to phase matching, whereas the presence of backward propagating SHG is a direct consequence of nonlinear mixing in a microcavity. Our results point to the potential for exploiting the resonator properties of individual objects, possibly paving the way for the development of novel nonlinear optical devices.

II. Experimental Section

The nonlinear microscope consists of an ultrafast laser source coupled to a far-field microscope (Figure 1). A mode-locked Ti:sapphire laser (Spectra Physics Tsunami) pumped by a 5 W frequency-doubled continuous-wave diode laser (Spectra Physics Millenia) is used as the excitation source. The system produces 80 fs pulses at a 76 MHz repetition rate and can be tuned between 720 and 850 nm with a maximum power output of approximately 1 W. The laser output is sent through a Faraday isolator and prism-pair compressor operated in a double pass configuration. A half-wave plate and polarizing cube serve as a variable attenuator, reducing the average power entering the microscope to about 10 mW. The beam diameter is expanded by a factor of 4 and directed, by reflection off a dichroic mirror (R, 680−1000 nm; T, 360−650 nm), into the objective (Olympus MSPlan 50×, NA 0.8) of an inverted microscope, overfilling its back aperture. Light focused by the objective onto the sample results in two-photon emission and/or second harmonic generation. Light collected by the objective is transmitted through the beamsplitter, focused onto the entrance slit of a monochromator, and detected by a photomultiplier tube operated in a photon-counting mode. Under typical experimental conditions, a signal photon is detected for every 500−1000 laser pulses. Images are compiled by raster-scanning the excitation spot over the sample using a piezoelectric x−y translation stage with a step-size and reproducibility that are both less than 20 nm. The spatial resolution of the microscope is determined by the size of the laser beam at the focus of the objective. Since the probability of two-photon excitation and second harmonic generation scales with the square of the laser intensity, efficient excitation occurs only at the focal point, resulting in confocal-like behavior and a lateral dimension that is smaller than the diffraction limit. The diameter (δ) of the excitation region is estimated[23] from $\delta = 2(\ln 2)^{1/2}(0.325\lambda)/2^{1/2}\,\mathrm{NA}^{0.91}$ to be approximately 350 nm. Images obtained from 100 nm fluorescent beads yielded a point spread function with a width of ∼400 nm.

Synthesis. ZnO structures were grown using hydrothermal and solution phase techniques adapted from Cheng et al.[24] and Li et al.[25] Rods analyzed in this work are synthesized by incubating a 0.05 M solution of $Zn(NO_3)_2$ and methenamine ($(CH_2)_6N_4$) under hydrothermal conditions for 3 h at 150 °C. The needle-like rods, which range in length from 1 to 30 μm, are collected on glass slides placed at the bottom of the reaction container. After completion of the reaction, the slide is removed from the container and sonicated in ethanol (200 proof) to harvest the rods. Microscopy samples are prepared by drop-casting ∼250 μL of the ZnO/ethanol suspension onto a microscope slide. Once the ethanol evaporates, the slide is placed on the scanning stage with the ZnO rods directly facing the objective lens. Imaging is performed without a coverslip under ambient conditions.

III. Results and Discussion

A scanning electron microscopy (SEM) image of a typical ZnO rod is displayed in Figure 2a. The SEM image shows a faceted ZnO rod that is ∼9 μm in length with a hexagonal cross section whose *c*-axis is directed along the primary growth direction. The diameter varies along the length of the rod from about 500 nm at the ends to approximately 1.5 μm at its widest point. Figure 2e shows the emission spectrum following two-photon excitation at 730 nm (1.70 eV) of the ZnO rod shown in Figure 2a. Since the spatial extent of the excitation (400 nm) is smaller than the rod (9 μm), the emission collected by the objective originates from a localized region of the structure, which in this case is the midpoint of the rod. The spectrum contains a sharp SHG peak at 365 nm (3.40 eV), a band edge emission peak at 390 nm (3.18 eV), and a broad peak centered at 550 nm (2.25 eV) that is commonly assigned to trap states arising from defects in the crystal structure.[1] Panels b−d of Figure 2 show the images obtained at the second harmonic, band edge, and trap state emission wavelengths, respectively. The band edge and trap state emission images show increased intensity at the ends of the rod, and a reduction in emission intensity at the midpoint that could be evidence of a grain boundary not observed in the SEM.

The SHG image differs considerably from the two emission images, displaying a periodic pattern of enhanced intensity along the rod axis. Although not apparent in this particular rod, periodic variations are occasionally observed in band edge and trap state emission images; however, the contrast is much lower and exists in only a very small portion of analyzed rods. While the periodic SHG pattern is a general phenomenon that is reproduced in a large number of needle-like rods, it is not observed in all rod shapes. SHG images of ZnO nanowires obtained by other groups using near-field and far-field methods do not show periodic variation of the type observed here.[21,26] The pattern is also not observed in rods with parallel sides, i.e.,

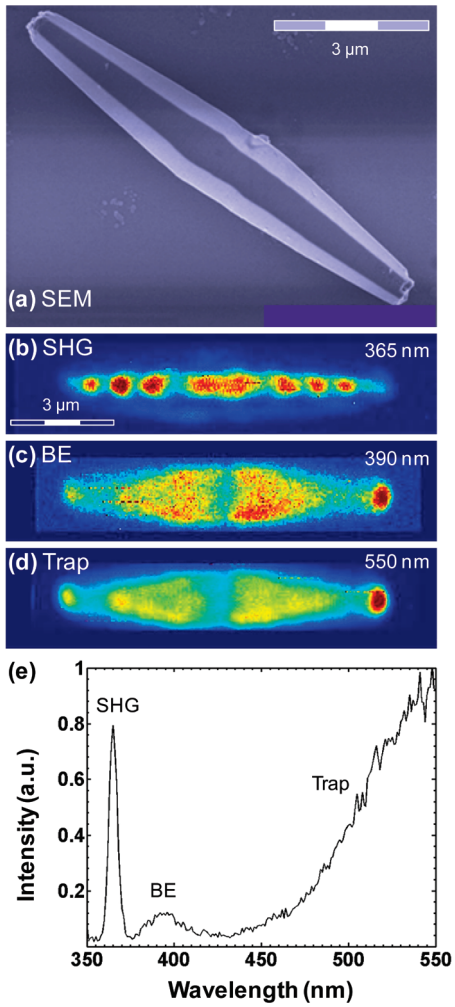

Figure 2. Nonlinear second harmonic and two-photon emission microscopy of an individual ZnO rod. (a) Scanning electron microscopy image of a needle-like ZnO rod that is approximately 9 μm in length with its *c*-axis as the primary growth direction. (b) Second harmonic microscopy image (365 nm) and two-photon photoluminescence images corresponding to (c) band-edge (BE) emission (390 nm) and (d) trap state emission (550 nm) observed following excitation at 730 nm (1.7 eV). Periodic variation is clear in the second harmonic image, whereas the photoluminescence images show no such variation. (e) The steady-state emission spectrum observed following excitation at the midpoint of the rod.

rectangular profiles (data not shown), suggesting that the phenomenon is associated with the variation in diameter that occurs along the length of the rod in the needle-shaped structure.

These observations invoke the question: What is the physical explanation for the periodic pattern? The periodic nature suggests that the phenomenon is linked to optical cavity modes supported by the ZnO resonator. Such an assertion is not without precedence. A variety of ZnO structures are observed to support optical cavity modes, and because of the short cavity lengths, the spacing between adjacent resonances is oftentimes large enough that they can be resolved in the emission spectrum.[16−22,27,28] The image in Figure 2b is a direct manifestation of the cavity and its affect on the SHG process. In principle the active modes could either lie longitudinal or transverse to the rod axis; however, the geometry of our experiment (Figure 1) suggests that it is modes supported by the cross section of the rod that are giving rise to the periodic pattern.

The simplest cavity that can be supported by the hexagonal cross section of a ZnO rod is a Fabry−Pérot resonator formed from two plane-parallel facets (Figure 3f). For the needle-like structures, excitation at different points along the rod axis corresponds to interaction with resonators of varying cavity lengths. The intensity of the fundamental stored within a Fabry−Pérot resonator of cavity length d is given by[29]

$$I_\omega(d) = I_0 \frac{1}{1 + F \sin^2\left(2\pi \frac{n_2 d}{\lambda_\omega}\right)} \quad (1)$$

where the finesse $F = 4R/(1 - R)^2$ can be determined from the indices of refraction inside (n_2) and outside (n_1) the resonator with the reflection at the boundaries given by $R = (n_1 - n_2)^2/(n_1 + n_2)^2$ at normal incidence. $I_\omega(d)$ is a periodic function with maximum coupling into the cavity occurring for values of d equal to an integer number of half-wavelengths, i.e., $d = m(\lambda_\omega/2n_2)$ with $m = 1, 2, 3$, etc. Depicted in Figure 3b is $I_\omega(d)$ obtained with $n_1 = 1.0$ (air), $n_2 = 2.3$ (ZnO), and $\lambda_\omega = 746$ nm. The intensity stored in the cavity exhibits a series of broad resonances spaced at multiples of 162 nm. The widths of the resonances are a result of the low reflectivity at the interfaces (~15%). It is the periodic nature of $I_\omega(d)$ combined with a varying facet separation along the rod axis that is the qualitative origin of the second harmonic generated images.

We have taken this qualitative idea one step further and used the resonance function, $I_\omega(d)$ shown in Figure 3b to simulate the second harmonic patterns observed in our images. Displayed in panels d and e of Figure 3 are the SHG and SEM images of a 9 μm long ZnO rod. The procedure involves first using the SEM image to measure the diameter of the rod, d_r (Figure 4f) as a function of distance along the rod axis. The facet separation is then estimated from the diameter assuming that the cross section is a perfect hexagon ($d_{FP} = 3^{1/2}d_r/2$); the result is displayed in Figure 3a. The SHG intensity along the rod axis is obtained by mapping the square of the intensity values ($I_{2\omega} = I_\omega^2$) in Figure 3b onto the facet separation in Figure 3a. Since the plane-parallel plates of the hexagon do not extend toward infinity but only span the length of a facet (*s* Figure 3f), the spatial intensity variation perpendicular to the rod axis is approximated as a Gaussian with a full width at half-maximum of *s*. The result is a matrix of intensity values displayed in Figure 3c. Despite the simplicity of the model the simulated image is in remarkable agreement with the experimental image. The relatively minor differences between the experimental and simulated images may be due to an uncertainty in the refractive index for ZnO since a range of values between 2.2 and 2.4 have been reported for the wavelengths of interest,[1] or they reflect an imperfect hexagonal cross section (i.e., not all facets are of equal length implying that $d_{FP} = 3^{1/2}d_r/2$ is only approximate). Furthermore, the simulation models the needle-like structure of the rod as a series of hexagonal slabs calculating the energy stored in the cavity assuming the facets are parallel and using that to determine the intensity of the second harmonic. The facets are not quite parallel, and in this respect our model is only approximate. The tapered shape introduces walk-off that would decrease the finesse of the cavity relative to the parallel geometry assumed in the model. Since ZnO has low reflectivity at the interfaces (~15%), it already has a low finesse and walk-off would just reduce this further. Despite this limitation, the similarity between the simulated and experimental images suggests that the additional reduction in the cavity finesse introduced by nonparallel facets is a relatively minor effect.

The resonance condition ($d = m(\lambda_\omega/2n_2)$) predicts that for a given mode number (m), the resonant cavity length will increase

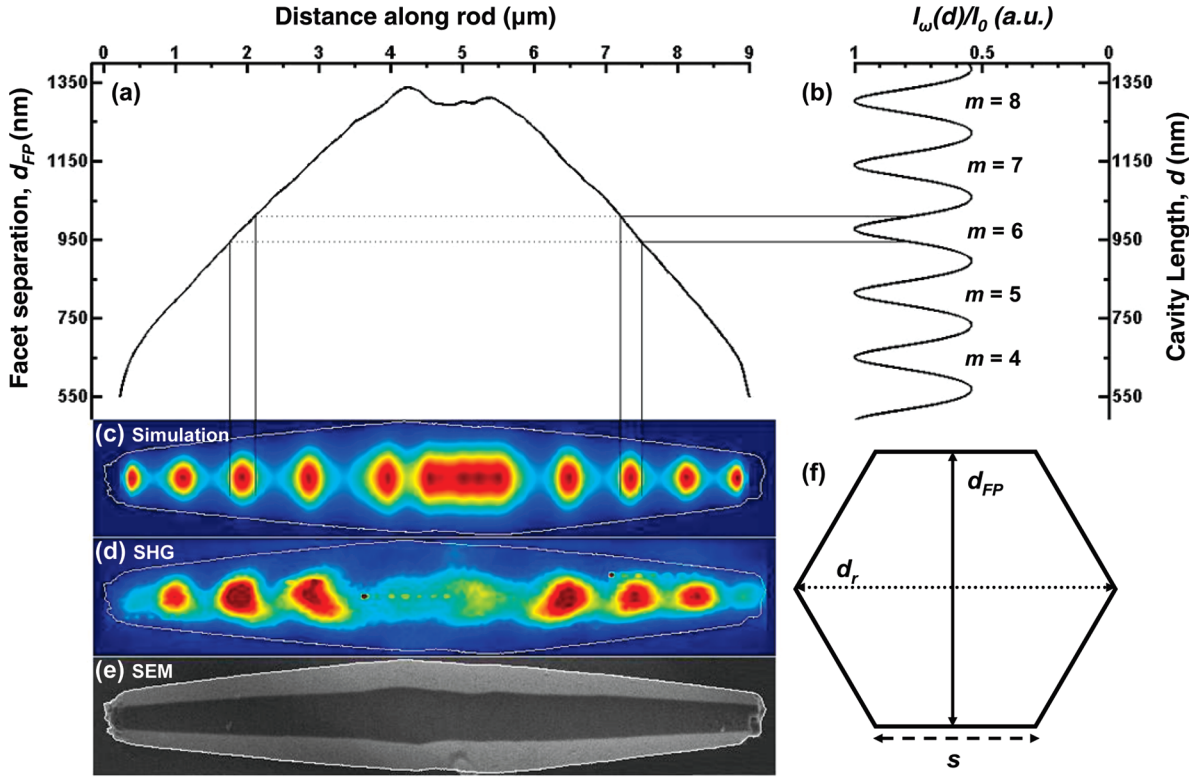

Figure 3. Cavity mode analysis of the second harmonic images. (a) A plot of facet separation (d_{FP}) as a function of distance along the rod axis measured from the SEM image of the needle-like ZnO rod shown in panel (e). (b) Intensity of the fundamental (I_ω) stored inside a Fabry−Pérot resonator as a function of cavity length. Obtained using eq 1 with $n_1 = 1.0$ (air), $n_2 = 2.3$ (ZnO) and $\lambda_\omega = 746$ nm. The intensity stored in the cavity exhibits a series of broad resonances spaced at multiples of 162 nm. The widths of the resonances are a result of the low reflectivity at the interfaces (∼15%). The solid lines represent the fwhm (I_ω) of integer $m = 6$ half-wavelengths which fit inside the resonator. (c) Simulated second harmonic generated microscopy image using (a) and (b). (d) Experimentally collected second harmonic generated microscopy image. (e) Scanning electron microscopy image of a needle-like ZnO rod used to generate (a). (f) Illustration of the hexagonal cross section of a ZnO rod with facet separation (d_{FP}), diameter (d_r), and facet length (s).

linearly with the fundamental wavelength. Figure 4 displays a series of SHG images collected over a range of excitation wavelengths. The images obtained from 726 to 750 nm ($\lambda_{2\omega} =$ 363−375 nm) are relatively similar, each displaying the clear periodic pattern that was also present in Figure 2b. Inspection of multiple rods confirms that in general each resonance spot moves toward the midpoint of the rod (in the direction of larger d_{FP}) as λ_ω is tuned to the red. This general trend is apparent in Figure 5, which represents data obtained from four different rods. The figure shows the facet separation (d_{FP}) at three SHG resonances, which correspond to $m = 5$, 6, and 7 standing wave modes, as a function of excitation wavelength. The shaded areas depict the resonant cavity lengths predicted by $d = m(\lambda_\omega/2n_2)$ for n_2 between 2.2 and 2.4.

The absence of the same modulation in the two-photon emission images (Figure 2c,d) indicates that the physical origin of the pattern is not simply a consequence of the spatial variation in light intensity along the rod due to the coupling of fundamental optical field into the Fabry−Pérot modes of the ZnO resonator. The pattern instead stems from the standing wave that is created between the two parallel facets. This standing wave, which can be thought of as a superposition of two propagating waves traveling in opposite directions, in turn produces a second-order polarization wave with zero phase velocity that extends throughout the rod. The standing-wave nature of this polarization leads to the generation of second harmonic photons that propagate in both forward and back directions. The backscattered second harmonic is not produced in bulk ZnO and is a direct consequence of second harmonic generation in an optical resonator. When the near-infrared photon energy is larger than half the ZnO band gap, the second harmonic will likely travel only 100 nm before it is reabsorbed by the ZnO. Under these conditions it is unlikely that the second harmonic couples into a resonator mode. It is the nonlinear polarization standing wave that is responsible for the observed enhanced backscattered SHG; when the facet separation is such that the fundamental is off resonance, the standing wave is not formed and the backscattered second harmonic generation is suppressed.

Excitation above the ZnO band gap (726−750 nm) results in SHG images that are dominated by the standing wave pattern with the most intense second harmonic along the center of the rod. When the fundamental wavelength is tuned below the band gap, from 750 to 810 nm, a qualitatively different SHG behavior is observed (Figure 4). At the lowest energies ($\lambda_\omega = 775$−810 nm) the second harmonic intensity shifts to the outside of the rod to coincide with the rod vertices and angled facets giving rise to a complicated intensity pattern. The images obtained at intermediate excitation wavelengths (755 and 762 nm) appear to be a combination of these two extremes. The origin of this shift is not entirely clear but may reflect a competition between different types of cavity modes supported by the rod cross section.

While a Fabry−Pérot cavity is the simplest cavity that could be formed inside a hexagon cross section, it is not the only one available. Whispering gallery modes (WGM) correspond to the circulation of light around the perimeter of the rod due to total internal reflection off each of the six facets, resulting in larger Q-factors when compared to standing wave Fabry−Pérot modes, where the reflectivity is only ∼15%. The main cavity loss for

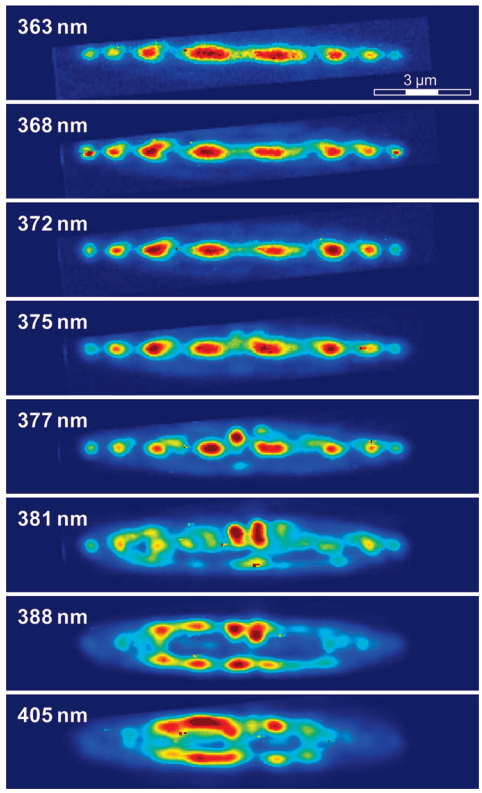

Figure 4. Second harmonic images as function of excitation wavelength. An array of second harmonic generation microscopy images of a needle-like ZnO rod after photoexcitation over a range of fundamental wavelengths (726−810 nm). The images show periodic areas of enhanced SHG intensity. The SHG intensity pattern qualitatively changes around 377 nm, correlating with excitations falling below the band gap. Each SHG image is scaled individually, masking the variation in the absolute intensity that is observed across this range. In particular, as the second harmonic photon energy is tuned toward the exciton resonance (380 nm), we observe an increase in the SHG efficiency due to resonance enhancement.

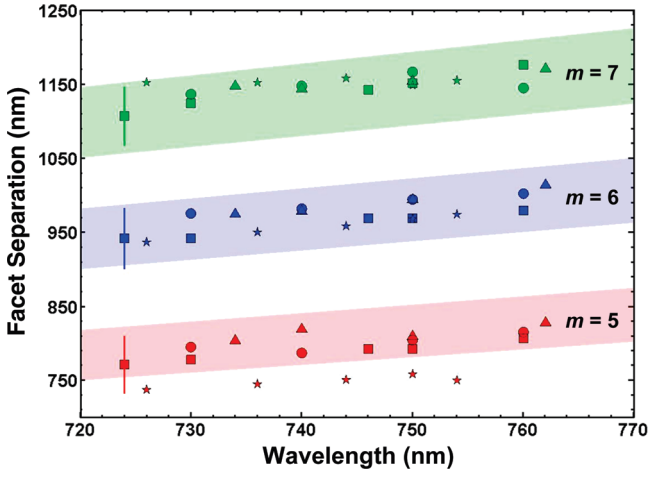

Figure 5. Facet separations measured from the SEM image at the positions of the $m = 5$, 6, 7 SHG resonances for a series of different laser excitation wavelengths. The figure is a compilation of data from four different needle-like ZnO rods (□, ●, ▲, ★). The error bars represent the average uncertainty associated with measuring the facet separation. The shaded regions highlight the resonance conditions, $d = m(\lambda_\omega/2n_2)$ for $m = 5$, 6, 7, with n_2 between 2.2 and 2.4.

WGM occurs at the vertices,[30] which is in qualitative agreement with the increased SHG intensity observed at the edges of the facets. The primary evidence for the presence of these modes in ZnO structures has come from modulation in their emission spectra,[16,18−20,27,28] with far fewer observations resulting from direct imaging. One recent exception to this is the report of periodic modulation in SHG images of ZnO tetrapods,[31] consistent with our results; however, the resolution of those images precluded the direct observation of preferential emission from the vertices and the assignment was made on the basis of geometrical arguments. The competition between the WGM and Fabry−Pérot modes may stem from the reabsorption of the second harmonic at the blue end of the excitation range, giving rise to a path-length-dependent loss that would favor the shorter Fabry−Pérot cavity. We are currently employing the finite-difference time-domain (FDTD) method,[32] using a freely available software package,[33] to further explore this competition.

IV. Conclusion

Spatial imaging of single needle-shaped ZnO structures using second harmonic generation microscopy exhibit cavity-enhanced second-order mixing. Images obtained from individual structures show areas of enhanced second harmonic intensity along the longitudinal axis of the rod that are periodically distributed and symmetrically situated relative to the rod midpoint while both band-edge and trap state emissions do not. It is the periodic nature of the intensity of the fundamental contained inside the cavity $I_\omega(d)$ combined with a varying facet separation along the rod axis that is the qualitative origin of the second harmonic generated images. The spatial modulation is a direct consequence of the fundamental optical field coupling into standing wave resonator modes of the ZnO structure, leading to an enhanced backscattered second harmonic condition that cannot be achieved in bulk ZnO. As the fundamental wavelength is tuned below the band gap, a qualitative change in the SHG image is observed. The complicated image is most likely due to the competition between Fabry−Pérot and whispering gallery modes.

Acknowledgment. This project was supported by a grant from the National Science Foundation (CHE-0809045). A.J.R. is a student Chapel Hill High School in Chapel Hill, North Carolina, and a participant in the ACS Project SEED program.

References and Notes

(1) Ozgur, U.; Alivov, Y. I.; Liu, C.; Teke, A.; Reshchikov, M. A.; Dogan, S.; Avrutin, V.; Cho, S. J.; Morkoc, H. *J. Appl. Phys.* **2005**, *98*, 041301.
(2) Morkoc, H.; Strite, S.; Gao, G. B.; Lin, M. E.; Sverdlov, B.; Burns, M. *J. Appl. Phys.* **1994**, *76*, 1363.
(3) Nakayama, Y.; Pauzauskie, P. J.; Radenovic, A.; Onorato, R. M.; Saykally, R. J.; Liphardt, J.; Yang, P. D. *Nature* **2007**, *447*, 1098.
(4) Berger, V. *J. Opt. Soc. Am. B* **1997**, *14*, 1351.
(5) Rosencher, E.; Vinter, B.; Berger, V. *J. Appl. Phys.* **1995**, *78*, 6042.
(6) Ashkin, A.; Boyd, G. D.; Dziedzic, J. M. *IEEE J. Quantum Electron.* **1966**, *Qe 2*, 109.
(7) Simonneau, C.; Debray, J. P.; Harmand, J. C.; Vidakovic, P.; Lovering, D. J.; Levenson, J. A. *Opt. Lett.* **1997**, *22*, 1775.
(8) Fiore, A.; Berger, V.; Rosencher, E.; Bravetti, P.; Nagle, J. *Nature* **1998**, *391*, 463.
(9) Pellegrini, V.; Colombelli, R.; Carusotto, I.; Beltram, F.; Rubini, S.; Lantier, R.; Franciosi, A.; Vinegoni, C.; Pavesi, L. *Appl. Phys. Lett.* **1999**, *74*, 1945.
(10) Cao, H.; Hall, D. B.; Torkelson, J. M.; Cao, C. Q. *Appl. Phys. Lett.* **2000**, *76*, 538.
(11) Dolgova, T. V.; Maidykovski, A. I.; Martemyanov, M. G.; Fedyanin, A. A.; Aktsipetrov, O. A.; Marowsky, G.; Yakovlev, V. A.; Mattei, G. *Appl. Phys. Lett.* **2002**, *81*, 2725.
(12) Mondia, J. P.; van Driel, H. M.; Jiang, W.; Cowan, A. R.; Young, J. F. *Opt. Lett.* **2003**, *28*, 2500.
(13) Djurisic, A. B.; Leung, Y. H. *Small* **2006**, *2*, 944.
(14) Wang, Z. L. *J. Phys.: Condens. Matter* **2004**, *16*, R829.
(15) Thomas, D. G. *J. Phys. Chem. Solids* **1960**, *15*, 86.

(16) Liu, J. Z.; Lee, S.; Ahn, Y. H.; Park, J. Y.; Koh, K. H.; Park, K. H. *Appl. Phys. Lett.* **2008**, *92*, 263102.
(17) Ruhle, S.; van Vugt, L. K.; Li, H. Y.; Keizer, N. A.; Kuipers, L.; Vanmaekelbergh, D. *Nano Lett.* **2008**, *8*, 119.
(18) Nobis, T.; Grundmann, M. *Phys. Rev. A: At., Mol., Opt. Phys.* **2005**, *72*, 063806.
(19) Nobis, T.; Kaidashev, E. M.; Rahm, A.; Lorenz, M.; Grundmann, M. *Phys. Rev. Lett.* **2004**, *93*, 103903.
(20) Sun, L. X.; Chen, Z. H.; Ren, Q. J.; Yu, K.; Bai, L. H.; Zhou, W. H.; Xiong, H.; Zhu, Z. Q.; Shen, X. C. *Phys. Rev. Lett.* **2008**, *100*, 156403.
(21) van Vugt, L. K.; Ruhle, S.; Ravindran, P.; Gerritsen, H. C.; Kuipers, L.; Vanmaekelbergh, D. *Phys. Rev. Lett.* **2006**, *97*, 147401.
(22) Johnson, J. C.; Yan, H. Q.; Yang, P. D.; Saykally, R. J. *J. Phys. Chem. B* **2003**, *107*, 8816.
(23) Zipfel, W. R.; Williams, R. M.; Webb, W. W. *Nat. Biotechnol.* **2003**, *21*, 1369.
(24) Cheng, B.; Shi, W. S.; Russell-Tanner, J. M.; Zhang, L.; Samulski, E. T. *Inorg. Chem.* **2006**, *45*, 1208.
(25) Li, F.; Li, Z.; Jin, F. J. *Mater. Lett.* **2007**, *61*, 1876.
(26) Johnson, J. C.; Yan, H. Q.; Schaller, R. D.; Petersen, P. B.; Yang, P. D.; Saykally, R. J. *Nano Lett.* **2002**, *2*, 279.
(27) Czekalla, C.; Sturm, C.; Schmidt-Grund, R.; Cao, B. Q.; Lorenz, M.; Grundmann, M. *Appl. Phys. Lett.* **2008**, *92*, 241102.
(28) Wang, D.; Seo, H. W.; Tin, C. C.; Bozack, M. J.; Williams, J. R.; Park, M.; Tzeng, Y. *J. Appl. Phys.* **2006**, *99*, 093112.
(29) Demtröder, W. *Laser spectroscopy: basic concepts and instrumentation*, 3rd ed.; Springer: Berlin, 2003.
(30) Wiersig, J. *Phys. Rev. A: At., Mol., Opt. Phys.* **2003**, *67*, 023807.
(31) Zhang, Y.; Zhou, H.; Liu, S. W.; Tian, Z. R.; Xiao, M. *Nano Lett.* **2009**, *9*, 2109.
(32) Taflove, A.; Hagness, S. C. *Computational electrodynamics: the finite-difference time-domain method*, 3rd ed.; Artech House: Boston, 2005.
(33) Farjadpour, A.; Roundy, D.; Rodriguez, A.; Ibanescu, M.; Bermel, P.; Joannopoulos, J. D.; Johnson, S. G.; Burr, G. W. *Opt. Lett.* **2006**, *31*, 2972.

JP9009614